Universitá degli studi di Roma
"Tor Vergata"

FACOLTA' DI SCIENZE MATEMATICHE, FISICHE
E NATURALI

DOTTORATO DI RICERCA IN ASTRONOMIA

XX CICLO

The connection between solar magnetic fields and photospheric dynamics

Silvia Giordano

Thesis Advisor:
Prof. Francesco Berrilli

Thesis Coordinator:
Prof. Roberto Buonanno

Contents

List of Figures

List of Tables

Foreword

Convection is the chief mode of heat transport in the outer envelopes of cool stars such as the Sun. Convective effects are recognizable in large-scale features, such as the global differential rotation and meridional circulation flows, as well as smaller scale phenomena such as granulation, mesogranulation, and supergranulation. Moreover, convective flows widely determine the evolution and organization of tiny magnetic elements observed in the solar surface responsible for small scale irradiance solar variations.

Our understanding of the solar convection derives from numerical simulations of compressible convection (MHD approach) and from spectral observations of the solar surface (velocity and center line maps, helioseismological data, etc.).

In this work we face the problem of connection between solar magnetic fields and photospheric dynamics through an experimental approach. In particular we worked on acquisitions systems for solar imaging spectroscopy, on a pipeline for the spectroscopic data reduction and on the data analysis.

One of the basic tools of observational solar physics is spectroscopy, which allows us to derive information on several physical parameters of solar atmosphere such as velocity, temperature, magnetic field strength etc. Spectroscopic analysis allows us to determine the vertical velocity of solar surface structures. Moreover, as wavelength can be somehow associated to depth in the solar atmosphere, it is possible to transform a bidimensional image in a 3-D field.

In order to study solar atmosphere dynamics, observations of adequate spectral purity, together with high spatial resolution to resolve small-scale structures are necessary. Moreover, the rapid evolution of observed solar features requires monochromators with high transparency to acquire multiple-line spectra in a comparatively short time. In order to meet all these requirements, suitable instruments and techniques have to be used. An instrument which satisfies all these constraints is IBIS, an Interferometric Bidimensional Spectrometer, installed at the Dunn Solar Telescope/NSO (Sac Peak, USA). IBIS produces data with high spectral ($\lambda/\Delta\lambda \simeq 200000$), spatial (0.2" at DST telescope) and temporal resolution (exposure time 10 ms; acquisition rate 5 frames s^{-1}). Images acquired with IBIS are currently recorded by a CCD camera.

Chapter 1 introduces the reader to the solar spectroscopy and to the use of spectroscopic imaging to retrieve information on solar photospheric layers dynamics. The basic concept and the layout of the IBIS spectrograph, used in this thesis to acquire spectroscopic images, is described.

Chapter 2 reports laboratory measurements and calibrations, derived through the application of the Photon Transfer Technique, of two sensors: the SI-1920 HD CMOS sensor and the Andor DV885 EMCCD sensor. Our interest in these

sensors is related to the necessity to replace the CCD camera, now installed on the IBIS spectral channel. Improvements in the IBIS camera system concern an increased sensitivity/quantum efficiency, a decreased detector readout time, a larger array size and an increased full well/programmable detector gain.

Chapter 3 describes the various steps of the pipeline developed for the IBIS data reduction. The pipeline includes both the standard image processing and a high performance IDL software package written specifically for high resolution solar images.

In Chapter 4 we report some results related to the study of the emergence and the organization of the magnetic field on the solar surface both as isolated structures and as clusters. More in detail, typical isolated magnetic features are pores or sunspots.

We investigated the small scale dynamics of a strong magnetic field region (pore) with a light bridge inside it, observed with the IBIS spectrometer. An analysis of the intensity and velocity maps revealed the presence, inside the light bridge, of elongated structures showing a kind of reversal in intensity and velocity. More in detail, in the intensity images we observed a narrow central dark lane running along the axis of the light bridge, that we explain proposing an analytical model. Regarding the velocity structure, its topology resembles a convective roll and may indicate a modification of the photospheric convective flows.

By adopting the IBIS dataset, we studied the oscillatory properties of the solar atmosphere, in the photosphere and the chromosphere, with particular regard to the influence of the magnetic topology. In particular, we analyzed the propagation of waves in the atmosphere in correspondence of a pore, of a magnetic network area and of a quiet Sun region. Studying the generation and propagation of waves in the solar atmosphere provides information about the atmospheric structure and dynamics and it helps to identify the key mechanism of chromospheric and coronal heating.

Finally, by using large FoV MDI magnetograms we analyzed the spatial distribution of reticular clusters of magnetic features, such as the magnetic network. For this purpose, we developed a numerical algorithm able to detect voids between magnetic fragments. We computed Void Probability Functions which describe, in a uniform and objective way, the assessment of the void structure of different magnetic elements distributions.

Acknowledgements

At the end of this work I feel in debt with a lot of people who, in one way or another, gave me the strength to continue along this way. Without their help and their constant encouragement, now I wouldn't be writing this thesis. I will try to remember all ones and I apologize if I am forgetting someone.

First of all, a special thought is for my advisor Prof. Francesco Berrilli. Without his continued support, encouragement, assistance and patience the research presented in this thesis would not have been completed. He has taught me a lot of solar physics and has increased my interest in the Sun. During these years he took care not only of my instruction as a solar physicist, but of my well-being. He always had time to listen to me in the most difficult moments. I will never forget the long conversations had together.

I am grateful to Prof. Alberto Egidi, for useful discussion and suggestions, and to Prof. Sergio Cantarano who introduced me to the study of solid-state imaging sensors.

I would like to thank Prof. Roberto Buonanno, chairman of this Ph.D. course, for having stimulated my attendance to graduate courses and seminars that have widely extended my background in astronomy and astrophysics.

This Thesis research was carried on at the Dept. of Physics, Univ. of Rome "Tor Vergata" and has benefitted from the Regione Lazio CVS (Centro per lo studio della variabilitá del Sole) PhD grant.

Many thanks to Dario, Valentina, Bartolomeo and Roberto for their support, patience (I acknowledge that it is not so simple to bear me, especially in this last period) and above all for the time spent together, in the solar physics laboratory and not only. How could I forget all the awful coffees taken together at the "red", or better the "yellow", university bar! For me they are not colleagues but friends.

A special thought is for Dr. Arnaldo Florio for creative and interesting discussions on just everything and for sharing with me the brown sugar and the black chocolate passion!

I thank Dr. Katja Janssen for support and useful suggestions in the IBIS data reduction pipeline.

A sincere thank is for Dr. Giuseppe Consolini, who introduced me to the "complex" world of complexity and for Dr. Ermanno Pietropaolo who reduced part of the data used in this thesis and introduced me to the use of Labview.

I also would like to express my gratitude to Prof. Guido Ceppatelli who gave me the possibility to spend a short period at the IAC. Thanks also for the time spent with him as a friend.

I am also grateful to Dr. Jorge Sánchez Almeida for useful discussions had together during the short period spent at the IAC.

Special thank also to the NSO-Sacramento Peak observatory crew, in particular to M. Bradford, D. Gilliam and J. Helrod for their efficient support in the observations and above all for their kindness and user-friendliness!

Thanks to PhD colleagues for sharing this experience, and especially thanks to Francesco for breaks taken together during these three years and to Fiore, with whom I shared many and many good talks.

Very special thanks to Federica, who shared with me the PhD experience and to whom I opened my hearth in the most difficult moments. Thanks Federica for being the best friend one could hope to have and for being witness of the most important day of my life. Special thanks to Mariella for her long and amusing mails. Even if she was far away, she was always present.

Thanks to all friends who don't belong to the physics world and with whom I spent a great part of my spare time. I am grateful to them for the non-astrophysical conversations that helped me to retain my sanity. I want to finish this dissertation so I can only name a few: Anna and Gianmaria, Ester and Paolo, Simone & Co., Maria and Valeria, Anna and Lucio. Many of them shared with me the experience of "studenti fuori sede" becoming my Roman family.

Finally, I am truly grateful for having such a wonderful family. A great thanks is for my brother, Giacomo, and his wife, Loredana, who were always present in difficult moments of my stay in Rome and not only. A kiss if for Veronica, my little nephew, who has been providing me with all the joy needed. I am truly indebted to my parents, Ada and Carmine, who allowed me to follow a dream. They always believed in me and their never-ending support and love was especially important to reach this goal.

And finally and most important my infinite gratitude is for Federico, who was always at my side, from my first exam of "Analisi Matematica 1" to the last line of this thesis. His support was especially important during these last months to conclude this Thesis. Thanks Federico for your patience, your love and especially for your positive life "philosophy". You have always shown me the positive side of life.

For all those I forgot, you are included here: Thank you.

Chapter 1

Solar imaging spectroscopy

Magnetic fields play a key role in many astrophysical processes. The investigation of magnetism is strongly hampered by the inability to resolve the spatial scales at which many of the processes occur. The Sun provides a unique laboratory to study astrophysical magneto-hydrodynamics. It is the only stellar object close enough to resolve many of the features associated with magnetic activity, and therefore the Sun provides the only access to processes that are not directly observable on other astrophysical objects.

The magnetic field created in the convective zone emerges through the photosphere, forming a hierarchy of discrete strong-field structures with highly dynamic patterning. These time dependent patterns confirm that all magnetic activity occurring on the Sun, including the generation of magnetic flux by a self-excited dynamo process and the various phenomena like sunspots, coronal loops, flares and mass ejections, is largely determined by non-linear interactions between the convective flux of matter in the surface layers of the solar structure and the magnetic field emerging from internal regions.

In fact, the spatial and temporal behaviour of photospheric convective flows strongly influences the arrangement and evolution of magnetic elements emerging on the solar surface, contributing to the assembly of magnetic features which modulate the solar energy output. On the other side, local magnetic field clustering strongly dampens the efficiency of convection. Therefore, a complete insight of the dynamics of the plasma flows and their interaction with magnetic fields is essential to fully understand the solar convective layer.

In order to retrieve information on solar atmospheric layers dynamics observation at high spatial, spectral and temporal resolution are needed. To meet all these requirements, suitable instruments and techniques have to be used. In this chapter we will introduce the reader to solar spectroscopy and to the instrument, namely IBIS (Interferometric BIdimensional Spectrometer), used in this thesis to acquire solar spectroscopic images.

1.1 Introduction

ving plasma and the solar magnetic field determines the spatial configuration of the enhanced magnetic field in the outer layers of the Sun. The turbulent convection present in the external layers of the Sun drags the magnetic flux tubes

causing their emergence, cancellation, fragmentation and coalescence (Close et al. 2003). These processes determine the formation and the evolution of active regions and originate structures of all dimensions. The magnetic field is concentrated in relatively small magnetic regions with high field strength, between which the magnetic field is very much weaker. The strong field concentrations are localized at the edges of the convective cells: convective flow and magnetic field tend to exclude each other. Convective motions in the photosphere are responsible for the compression of magnetic "flux tubes" and play an important role in their evolution.

The buffeting of flux tubes by nearby granules generates transverse magnetohydrodynamic waves (Steiner et al., 1994), which dissipate their energy in the chromosphere and represent a possible source of heating in this region (Ofman et al., 1998). Convective flows also drive the motion of the footpoints of coronal magnetic loops, twisting field lines and resulting in magnetic reconnection. This process heats the corona through resistive dissipation (van Ballegooijen, 1998; Furusawa & Sakai, 2000). Moreover, magnetic features may account for variations in the Sun's luminosity during the solar active cycle. These changes in solar energy output could be responsible for climatic changes on Earth (Cubasch & Voss, 2000).

The observed general behaviour of magnetic flux in the solar atmosphere is well reproduced in numerical simulations. They allow us to study the full three-dimensional structure of magnetic field configurations, as well as the spatial scales which are not resolved by current observations, thus helping to develop consistent models of the physical processes underlying the observed phenomena. Numerical models of convection and magnetoconvection have provided us with much of our understanding of photospheric magnetic features.

When developing comprehensive simulations of magneto-convection, in order to well approximate solar conditions, we have to take into account elaborate physics: radiative transfer, which is the main driver of convection and has an important influence on the temperature structure and brightness of magnetic field concentrations, and partial ionization, which strongly affects the efficiency of convective energy transport.

Based on the seminal studies of linear stability of thermal magneto-convection by Chandrasekhar (1961), two different but complementary branches of numerical research, in the field of solar magnetoconvection, have been developed.

One uses simplified physics with the only aim to isolate and understand the basic physical processes that are involved. With the advent of ever more powerful computers in the 1980s, a second line of research emerged, which attempts to model the physical processes on the Sun as realistically as possible. In these simulations effects such as compressibility, ionization and radiative transfer have to be included. Despite the progress made in the field of realistic simulations, idealized studies have, until the present day, not lost their relevance. While they cannot be compared directly to observations, they allow us to isolate certain physical processes and are amenable to analytical tools like linear stability analysis and bifurcation theory, thus providing valuable insight into the underlying physical mechanisms.

Recently, following the lines of more idealized models, Cattaneo et al. (2001) presented large-scale, three dimensional, numerical experiments on highly nonlinear magnetoconvection in the Boussinesq approximation. These simulations show how an increase of the imposed magnetic field causes a gradual transition

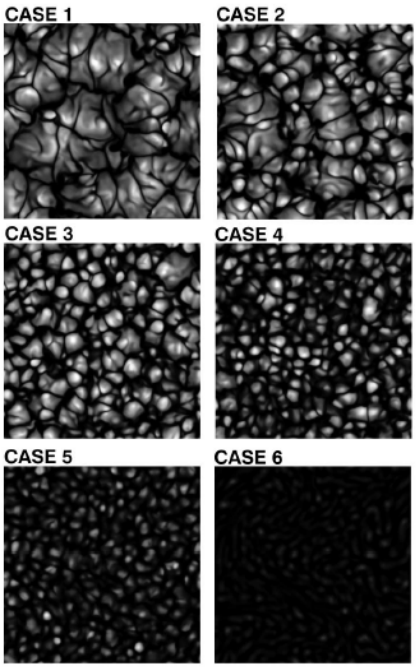

Figure 1.1: Snapshot of surface temperature fluctuations for increasing values of initial magnetic field B_0 (cases 1-6) (from Cattaneo et al., 2001).

from a dynamo regime through a convective regime to an oscillatory regime.

In Fig. 1.1 and Fig. 1.2 gray-scale plots of surface temperature and magnetic fluctuations are reported, respectively, for different values of the initial magnetic field B_0. Initially (*cases 1 and 2*), when B_0 is weak, the system is dominated by the turbulent convective flow and we observe a typical granular pattern. As a consequence, the magnetic field is localized at the borders of the convective cells, with the strongest magnetic signals identifying a large-scale pattern (*mesogranular scale*). For higher values of B_0 the convective pattern is affected by the magnetic field, as the Lorentz force becomes increasingly effective in preventing overturning motions. As a result, the horizontal scale of convection decreases: the cells grow narrower and become feebler. Another change in the surface features is the rapid disappearance of the mesocellular structures as B_0 is increased. When the magnetic field becomes very strong (*case 6*) the cellular pattern, displayed in previous cases, disappears: the system is dominated by the magnetic field so that the flow is no longer able to concentrate the magnetic flux at the edges of convective cells.

In contrast to these idealized simulations, "realistic" simulations of solar magneto-convection aim at approximating the real Sun, by including elaborate physics like radiative transfer, partial ionization, open and transmitting boundary conditions, spectral line and polarization diagnostics. For a realistic simulation the system of magnetohydrodynamic equations including the continuum, momentum, induction, and energy equations has to be solved, preferably in three spatial dimensions. Since flux concentrations are predominantly gov-

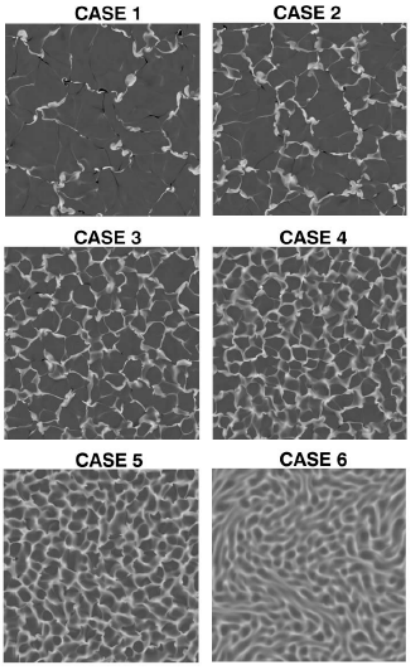

Figure 1.2: Snapshot of surface magnetic field. Light and dark regions indicate upward and downward orientation, respectively (from Cattaneo et al., 2001).

erned by convective motions, at very least the surface layers of the convection zone must be taken into account in order to obtain reliable results for the magnetic field in the photosphere. Hence, the computational domain must span the distinct radial section of the sun, where energy transport changes from convective to radiative, so that radiative transfer must be taken into account in the energy equation. An equation of state and opacities, appropriate for the solar plasma in the region of interest, are essential for a realistic simulation. The spatial extent of the computational domain is limited by the computational resources and the minimum spatial resolution required. Because of the obvious computational limitations, all realistic simulations are effectively large-eddy simulations in which the effects of small-scale motions, not explicitly included in the simulations, are parametrized by way of sub-grid models, hopefully providing a realistic description of their influence on the resolved scales. In the case of "non-magnetic convection", the simulations reproduce the observations remarkably well (Nordlund, 1984a; Nordlund & Stein, 1990b; Stein et al., 1992; Bercik et al., 1998). For simulations of solar magneto-convection, observational validation requires a comparison with observed profiles of the Stokes parameters (describing polarized light) for various spectral lines.

Recently, a 3D MHD simulation code (MURAM code), satisfying the requirements of realistic simulations, has been developed for applications in the solar photosphere and convective zone. It includes non-local and non-grey radiative transfer and takes into account partial ionization effects. Results obtained by applying this code to the study of the formation, dynamics and structure

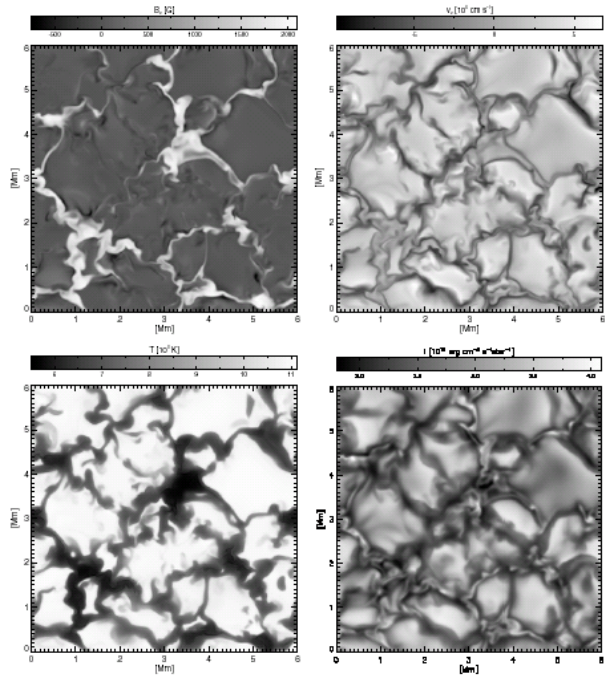

Figure 1.3: Map of (frequency-integrated) brightness (*lower right*) and horizontal cuts, at the the average geometrical height corresponding to unity optical depth, of temperature (*lower left*), vertical magnetic field (*upper left*) and vertical velocity (*upper right*). The velocity plot shows granular upflows (bright structures) surrounded by intergranular downflow lanes (dark regions). In the magnetic field plot, the bright regions correspond to strong concentrations of magnetic field. They individuate a network which is organized on a scale (mesoscale) larger than the spatial scale of the granulation.

of small-scale magnetic flux concentrations have recently been published in a series of papers by Schüssler and collaborators. Vögler et al. (2005) simulate magnetoconvection in a box encompassing an area on the solar surface of 6×6 Mm^2 with a height extension of 1400 km, reaching from the temperature minimum to 800 km below the surface of unity optical depth. Although this is only 0.4% of the convection zone depth, the box still includes the entire transition from almost completely convective to mainly radiative energy transfer and the transition from the regime where the flux concentration is dominated by the convective plasma flow to layers where the magnetic energy density of the flux concentrations by far surpasses the thermal energy density. The bottom boundary in this and similar simulations is open, in the sense that plasma can freely flow in and out of the computational domain, subject to the condition of mass conservation. Inflowing material has a given specific entropy that determines the effective temperature of the radiation leaving the domain at the top, while the outflowing material carries the entropy it instantly has.

Fig. 1.3 shows some results from three-dimensional simulations runs with the MURAM code. The simulation, initially purely hydrodynamic, starts from

a plane-parallel model of the solar atmosphere. A vertical magnetic field (B$\sim$ 200 G) is uniformly introduced after convection (granulation) has fully developed. Such a simulation shows that most of the magnetic flux is transported to the downflow lanes of the granular pattern, where the field is concentrated to kilogauss values by the convective intensification process. In Fig. 1.3 we report a map of the frequency-integrated emergent intensity (brightness) together with horizontal slices of temperature, vertical magnetic field, and vertical velocity at z = 0 for a snapshot taken about two hours of simulated solar time after the introduction of the magnetic field. The result is that the magnetic field forms elongated, sheet-like structures that extend along inter-granular lanes as well as larger structures with a size of up to 1000 km ("micropores"), which are located at vertices of several downflow lanes. Typical field strengths in these field concentrations at a height corresponding to unity optical depth are between 1500 and 2000 G. In intensity maps the micropores appear dark owing to the reduced efficiency, while smaller structures are usually brighter than the non-magnetic downflow lanes. The magnetic network, organized on a "mesoscale", is embedded in the network of granular downflows. This "mesoscale" is a typical and robust feature of convection simulations (e.g., Cattaneo et al., 2001).

From an observative point of view, over the past decade, the progress in observational techniques (e.g. imaging spectroscopy, speckle polarimetry, adaptive optics) has made it possible to resolve, on the solar surface, features that are only 0.1" wide (70 km on the Sun), making the fine structures created by magnetoconvection interactions recognizable and greatly improving our knowledge of photospheric magnetic fields. Moreover, observations provide a means of obtaining information on the variation of physical quantities along the line of sight in a structured atmosphere, albeit only in a highly convoluted form, which usually does not allow an unambiguous interpretation, while subphotospheric layers are entirely inaccessible to direct observations. The combination of observations with theoretical models is finally making it possible to understand the detailed mechanism that are responsible for the visible fine structures observed on the solar surface.

1.2 2-D solar spectroscopy

Spectroscopy is one of the most important tools of observational solar physics. The analysis of the spectrum of emitted radiation provides information about several physical parameters like velocity, temperature, pressure, magnetic field strength etc. The combination of all these physical quantities allows a proper description of the state of the solar atmosphere.

The instrument to record the spectrum of the incoming radiation is the spectrograph, consisting in prisms, gratings or other devices. Classical grating spectrographs record whole spectra at a time and at a fixed spatial coordinate, perpendicular to the slit, providing a high spectral resolution, better than 1 pm. In order to cover a larger field of view, so as to obtain a 2D spectrum of the source, it is necessary to scan the solar image across the slit. This method is slow in image acquisition, implying an effective resolution deterioration due to changing solar surface and atmospheric seeing. Moreover, the field of view ends up being limited by the length and width of the slit.

In order to circumvent the problem of spatial scanning, two-dimensional

spectroscopic techniques have been developed. 2-D spectrographs consist in tunable filter instruments employing either tunable Lyot filters, Michelson interferometers (MFI), Fabry-Perot interferometers (FPI) or a combination of them. These instruments perform a scan across the selected spectral line, thus providing a two-dimensional filtergram at each step. The individual narrow-band filtergrams, obtained at different wavelengths along a spectral line, are then combined to a full 2-D spectrogram. In this way, for each point across the field of view a spectral line profile can be constructed, by plotting the intensity at a certain position for each filtergram.

The main limitation of this technique is the time needed to complete a scan. If the time in which the spectral scan has been performed is much smaller than the typical temporal evolution of the solar surface, spectral images can be considered simultaneous.

Unlike grating spectrographs, by using a 2D spectrometer it is possible to obtain spatial and spectral information almost instantaneously over a 2D field of view.

The more relevant requirements of an ideal spectrometer are:

- High spectral resolution to analyze narrow photospheric lines;
- High spatial resolution to observe small structures, with sizes of $\simeq$ 50-100 km on the solar surface;
- High temporal resolution to observe rapidly evolving active phenomena;
- High wavelength stability to ensure the reproducibility of the selected spectral points;
- An extended field of view to easily study active regions;
- A large useful spectral range to allow a large choice among spectral lines with different diagnostic power.

It is difficult to satisfy simultaneously all these requirements, each one strictly depending on the others. In fact, a high spectral resolution can be obtained at the expense of photon flux. Long exposure times are required to not compromise the photometric accuracy. In such conditions the seeing cannot be considered frozen, thus reducing the effective spatial resolution. In conclusion, an imaging spectrometer, with simultaneously high spectral, spatial, and temporal resolution is a photon-starved instrument. The only way not to compromise the photometric accuracy is to increase throughput and transmittance. An instrument which satisfies both these characteristics is the Fabry-Perot interferometer (FPI), thanks to its large area and to the modern dielectric multi-layer coatings. Moreover, by using a FPI, it is possible to achieve a high spectral resolution, comparable to that of a grating spectrograph, and a rapid wavelength tuning, if piezo-scanned.

Only a few spectrometers based on two or more Fabry-Perot etalons have been built and succesfully used in astrophysical applications. The first systems were built in the sixties, e.g. the PEPSIOS-type spectrometers and the triple-FPIs of the Culgoora Observatory (Ramsay et al., 1970; Loughhead et al., 1978), which was never operative. Recently, two systems consisting in a FPI in series with a tunable birefringent filter were built in Goettingen (Bendlin et al., 1992;

Figure 1.4: The Dunn Solar Telescope telescope at Sacramento Peak, New Mexico (USA).

Bendlin & Volkmer, 1995) and in Florence (IPM: Italian Panoramic Monochromator) (Cavallini, 1998). Both instruments are characterized by a slow wavelength tuning and a low transmittance. The Goettingen instrument, operating at the Vacuum Tower Telescope (VTT) on Tenerife, has been very recently upgraded to a double FPI system (Koschinsky et al., 2001). Other two multi-etalons have been built: TESOS (Telecentric Etalon SOlar Spectrometer), born as a double-FPI spectrometer, is now a three-etalon system (Tritschler et al., 2002) operating, since 1997, at the VTT on Tenerife; IBIS (Interferometric BIdimensional Spectrometer), on which we will focus our attention, is a double-FPI instrument, operating at the Dunn Solar Telescope (DST) of the National Solar Observatory (USA-NM) since June 2003.

1.3 Richard B. Dunn Solar Telescope

The Dunn Solar Telescope (DST) is placed at the National Solar Observatory in Sunspot, NM, USA, at an altitude of 2804 m. Its basic design consists of a large 41 m tower with a 0.76 m window at the top. Sunlight is reflected by a pair of movable 1.1 m mirrors down a 1.2 m diameter, 100 m long evacuated tube. Light reflects off a concave 1.6 m main mirror at the bottom of the telescope, 57 m below ground, and then back up to the observing room. The two mirrors at the top act as a heliostat, therefore compensating for proper motion. The entire set-up hangs from a low-friction tank that contains about 10 tons of mercury and makes it is easy to rotate the 200 tons of tube and instruments to compensate for apparent image rotation.

Regarding the post-focus instrumentation, the DST is equipped with: a Uni-

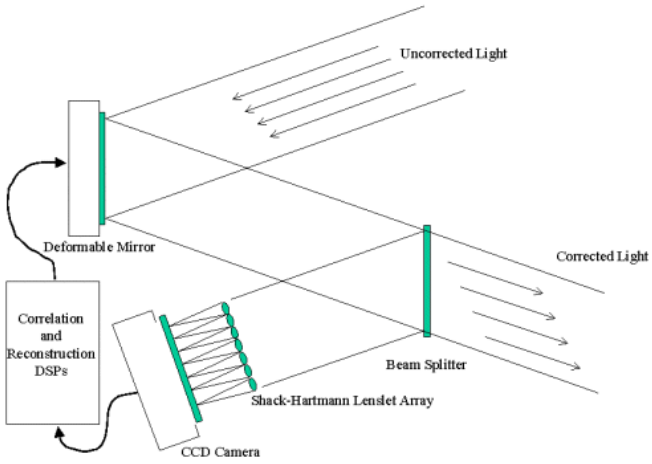

Figure 1.5: Block diagram of an adaptive optic system.

versal Birifrangent Filter (UBF), which allows the acquisition of monochromatic images in a large wavelength range, an Advanced Stokes Polarimeter (ASP), to analyze the polarized light and therefore the magnetic fields, an Echelle Spectrograph, which allows simultaneous measurements in two or more wavelengths and an Interferometric BIdimensional Spectrometer (IBIS), which we will lenghtly describe in the following section.

A high order adaptive optics (HOAO) system (Rimmele, 2004) is now operating at the DST. Fig. 1.5 shows the block diagram of an adaptive optics system. Essentially it includes a 97 actuator deformable mirror, built by Xinetics Inc, placed at a pupil of the telescope, a reconstructor based on commercial off-the-shelf DSPs and a correlating Shack-Hartmann wavefront sensor which measures the distortions introduced by the atmosphere. It consists of an array of lenslets which subdivide the circular telescope aperture (76 cm) into 76 sub-apertures and image it on a camera. The central subaperture is completely obstructed by the pick-off mirror for the DST guiding telescope beam. In this way the shape of the incoming wavefronts is measured as a function of position in the telescope aperture plane. The number of pixels per subaperture image is software selectable between 16×16 and 20×20 pixels. A high frame rate camera (2500 fps), based on a 1280×1024 Photobit CMOS image sensor, was custom developed for the wavefront sensor.

The mean wavefront perturbation in each pixel is calculated. A parallel processing approach, employing 40 DSP processors, is used to perform all computations for sensing and reconstructing the wavefront. The pixellated map of the wavefronts is fed into the deformable mirror and used to correct the wavefront errors introduced by the atmosphere. The DSPs also drive a tip/tilt mirror, mounted in front of the AO system, that removes gross image motion caused by the atmosphere.

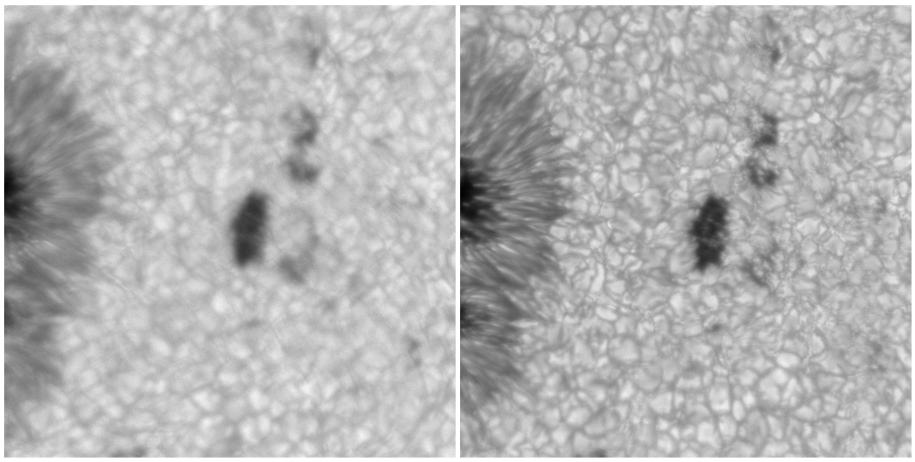

Figure 1.6: Sample images acquired at the Dunn Solar Telescope (λ=550 nm$\pm$10) with AO system off (*left*) and on (*right*). Each frame covers an area of 45"$\times$45".

1.4 IBIS

The Interferometric BIdimensional Spectrometer (IBIS) is a next generation bidimensional spectrometer based on a dual Fabry-Perot interferometric system. It was built at the INAF-Arcetri Astrophysical Observatory, with the contribution of the Department of Astronomy and Space Science of the University of Florence and the Department of Physics of the University of Rome "Tor Vergata". Since June 2003 it has been operating at the Dunn Solar Telescope (DST) at the National Solar Observatory in Sunspot, NM, USA. It was installed on an optical bench, fed by the previously described high-order AO system.

IBIS represents a powerful instrument addressing a variety of important observational programs in solar physics thanks to its high spectral resolution (0.3-0.5 nm) combined with short exposure times and a large field of view ($\sim$ 80").

1.4.1 Interferometer specification

The most important issues to be considered when a multi-FPI spectrometer is designed are the spacing ratios of the FPIs and the optical configuration. In this section we describe the respective considerations and the adopted solution.

A Fabry-Perot Interferometer is an optically resonant cavity, consisting in a pair of parallel transparent optical plates. The normalized transmission passband for a single FPI is described by an Airy function set

$$T(\lambda) = \frac{1}{1 + 4R(1 \quad R) \ ^2 sin^2(\frac{\psi}{2})} \tag{1.1}$$

where R is the surface reflectivity and ψ the phase delay between the plates, given by

$$\psi = 4\pi d\mu cos(\theta)/\lambda \tag{1.2}$$

d is the plate separation, μ the refractive index of the medium inside the cavity, θ the angle of incidence and λ the wavelength. This leads to the typical transmission pattern with maxima of order n, n=1,2,... for ψ=2πn and a Free Spectral Range, i.e. the spacing of two adjacent maxima, of FSR=$\lambda^2/2\mu d$. Such a transmission pattern prevents using a single FPI as a spectroscopic device.

It is possible to isolate a single interference order by employing a narrowband interference filter in tandem with a series of FP interferometers with suitable spacings. The resulting instrumental profile for such a combined system is obtained by multiplying the individual functions:

$$T(\lambda) = T_{IF}(\lambda) \prod_{i=1}^{N} T_i(\lambda) \tag{1.3}$$

where T_{IF} and T_i are the transmission profiles of the interference filter and of the i-th FP, respectively. A combination of two or more FPIs enlarges the FRS, so that the side unwanted interference orders are better suppressed and the spectral resolving power increases. On the other hand, the greater complexity of the system causes a decrease of the overall transparency and of the optical quality. On the basis of these considerations, a double FPI system was preferred for IBIS, which represents a good compromise between spectral resolution, transparency and optical quality. The adopted interferometers are two Queensgate ET-50, piezo-scanned and capacity servo-controlled etalons, with a diameter of 50 mm and a very short wavelength setting time (few ms). The surface quality of each plate is $\lambda/150$ after coating.

In designing a multi-FP system, once the number of FPIs has been defined, the next important step is the search of the ratio between the spacings of the two FPIs (the so-called *optimum ratio*). For IBIS a ratio of 0.277 has been chosen. It corresponds to the ratio value which best reduces the amount of parasitic light (for more details see Cavallini, 2006). Apart from the *optimum ratio*, other important instrumental parameters are the spacings of the two FPIs and the coating reflectivity. The best spacing has to be a compromise between a low parasitic light (P) and a high spectral resolving power (R), because with increasing spacing both P and R increase. To choose the coating reflectivity we have to consider that with increasing reflectivity the overall maximum transmittance of the two interferometers and the image quality decrease, while the ghost relative intensity increases. Therefore, a pair of interferometers with spacings t = 2.300 mm (FPI 1) and 0.637 mm (FPI 2) and a coating reflectivity R =0.93 have been chosen, as the best compromise between transparency, ghosts, parasitic light, image quality and spectral resolution.

Concerning the optical mounting, there are essentially two possibilities which can be adopted for the design of a FPI spectrometer: *collimated* (*classic*) (CM) or *telecentric* (TM) mounting (Fig. 1.7). In CM the FPIs are mounted near the image of the entrance pupil of the telescope. Every image point corresponds to collimated beams, incident with a specific angle with respect to the optical axis propagating through the FPIs. The effective plate separation is a function of this angle, which results in a wavelength gradient across the Field of View (FoV). With respect to the center of the FoV, the wavelength of the transmission maximum near the edges will be blue-shifted. Moreover, all rays distributed across the pupil image with equal inclination will form one image point. Therefore, non uniformity of the plate surfaces or parallelism errors will

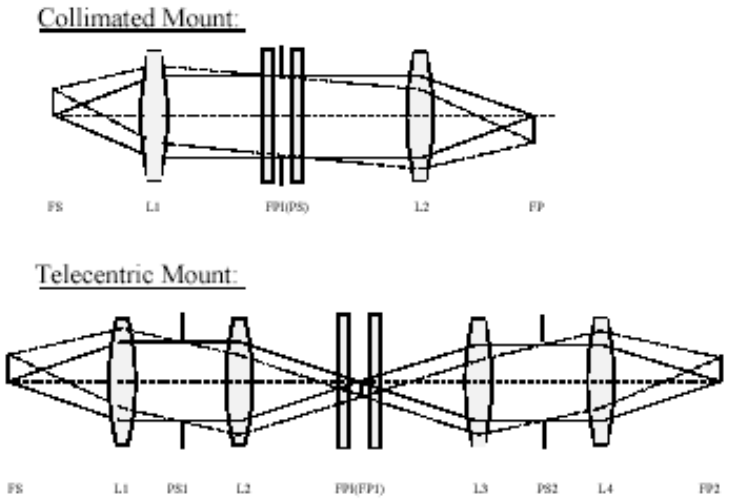

Figure 1.7: Schematic drawing of a double Fabry Perot Interferometers in collimated (or classic) and telecentric mount. In the first case the telescope aperture (PS) is imaged into the interferometers, L2 is the reimaging lens. At the FPI location the beam is collimated. In the second case, lenses L1 and L2 project the solar image (FS) into the interferometer. Lenses L3 and L4 image the solar image onto the detector

.

result in a broadening of the transmitted spectral profile. Thus the spectral profile depends not only on the reflection of the interferometer coatings but also on the flatness and parallelism of the plates.

In TM the pupil image is collimated and the FPIs are located near the image plane. In this case the points of the final image are formed by beams with the same cone angle at each point across the field of view. Since every position on the interferometer belongs to exactly one point within the solar image, there are no systematic wavelength shifts over the FoV due to angle variations.

A multi-FPI in CM suffers from the FoV spectral inhomogeneity, but the spectral resolution has the maximum obtainable value and the image quality is entirely preserved. For an ideal multi-FPI in TM the FoV is spectrally homogeneous, while the spectral resolution is lower than in CM. Concerning the image quality, it is reduced by a systematic effect, due to a wavelength dependent pupil apodization (Beckers, 1998; von der Lühe & Kentischer, 2000). On the basis of these considerations, for IBIS the CM has been preferred, obtaining the best spectral resolution and image quality, with the only disadvantage being the spectral inhomogeneity.

1.4.2 Optical design

The optical scheme of IBIS is shown in Fig. 1.8, where the solid line indicates the principal path. At the exit of the high-order AO, the telescope primary image is at infinity and a pupil image is formed near the first folding mirror m1, at the focus of the transfer lens L0. This lens and two further mirrors

(m2, m3) form the solar image on the field stop (FS) of the instrument, 21.3 mm in diameter, corresponding to 80" on the Sun. Three lenses (L1, L2, L3) and a folding mirror (M1) successively collimate the field stop and the pupil, producing an image of the latter compatible with the clear diameter of the interferometers. In more detail, L1 is used to obtain a pupil image on the shutter (ES) which controls the exposure time, while the other two lenses (L2 and L3) focus the image of the pupil on the filter wheel, positioned between the two Fabry-Perot interferometers. A fourth lens (L4) and two further folding mirrors (M2, M3), placed beyond the FPIs, form a solar image, 6.85 mm in diameter, on a CCD camera (CCD 1). A small amount of the incoming light ($\simeq$ 0.5%) is reflected by one of the two beamsplitters (BS 1), placed between L1 and L2, and passes through a second set of broad-band interference filters (FWHM=50 Å), centered at the same peak wavelength of the previous ones. A suitable set of optics finally forms, on a second CCD camera (CCD 2) identical to the first one, broad-band images of the same FoV and on the same scale of the monochromatic ones. Thanks to only one electronic shutter, placed near a pupil image, the two cameras simultaneously acquire a monochromatic and a white light image of the same solar area. Such white light images can be used as a transparency reference and/or for post facto procedures, to correct the seeing effects.

L2 and L3 lenses are used to obtain the classic mounting configuration of the two Fabry-Perot interferometers. Between the FPIs a filter wheel carries a set of narrow-band interference filters, with a passband of 0.3 nm or 0.5 nm depending on the wavelength (IBIS operates between 580.0 nm and 860.0 nm). Their role is to isolate the instrumental profile and to minimize the ghost images produced by inter-reflections between the two interferometers. They have a peak transparency of $\simeq$30% while the intensity of ghost images is $\simeq$10% of the principal one. Due to the filter, therefore, the resulting intensity of ghost images is reduced to $\simeq$1%. This allows us to use the interferometers in axial mode, avoiding the unwanted effects produced by their tilt, essentially consisting in a different shape of the instrumental profile in different points of the final image plane.

Some secondary optical paths allow us to perform the initial tuning between the two interferometers and the interference filters, and to verify and adjust the parallelism of the interferometer plates and their orthogonality to the optical axis. Referring again to Fig. 1.8, these secondary optical paths are indicated by dashed lines. In particular, the initial tuning between the two interferometers and the selected interference filters is obtained by injecting the radiation emitted by a halogen lamp (HL) into the principal optical path. The radiation emitted by a frequency-stabilized He-Ne laser sent to the principal optical path is used to verify and to adjust the parallelism of the interferometer plates. In order to determine the orthogonality between each interferometer and the optical axis a pellicle beamsplitter (BS2) can be inserted on the plane of the image formed by the second lens (L2).

Many instrumental components are provided with actuators for remote positioning, while four TV cameras allow the verification of the correctness of all operations. TV5, continuously showing the selected solar region, is used to monitor the solar and atmospheric conditions. The adopted CCD cameras are two high speed (5 MHz) Pentamax by Princeton Instruments with a Kodak KAF-1400 detector with 1317×1035 pixels.

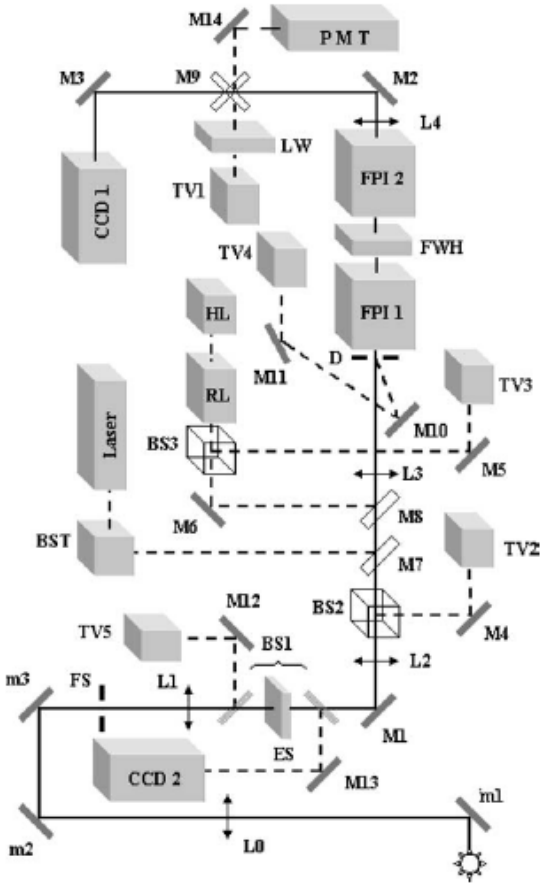

Figure 1.8: Schematic drawing of IBIS layout. The solid line represents the principal optical path, while the secondary ones are shown by dashed lines.

1.4.3 Instrumental characteristics

The IBIS instrumental characteristics, shown in Tab. 1.1, meet the initial requirements well. The spectral and temporal resolutions are satisfactory, as well as the useful wavelength range, the FoV and the wavelength stability. Concerning the spatial resolution, the image scale allows a suitable sampling and the exposure time is sufficiently short to apply post facto image restoring techniques. The more relevant instrumental characteristics of IBIS can be summarized as follows:

1. High spectral resolving power:
   $\mathcal{R} = \lambda/\Delta\lambda =$ 205000 (at 8600 Å) - 320000 (at 7000 Å);

2. High wavelength stability:
   the maximum drift of the instrumental profile is < 10 m$\cdot s^{-1}$ on 10 h;

3. Large useful spectral range:
   the useful spectral range covers 2800 Å (5800 Å-8600 Å);

Wavelength range	580.0 - 860.0 nm
Available spectral lines	589.6 nm Na D1
	630.2 nm Fe I
	709.0 nm Fe I
	722.4 nm Fe II
	854.2 nm Ca II
Range width	$\pm$ 200 pm (580.0 - 750.0 nm) $\pm$ 350 pm (750.0 - 860.0 nm)
Spectral resolving power	212000 - 274000
Passband FWHM	2.1 pm - 4.2 pm
Wavelength drift of the instrumental profile	$\leq 10m \cdot s^{-1}$ on 10 h
Field of view	80" (circular)
Peak transparency	15% - 20%
Image scale	0.08" pixel $^{-1}$
Exposure time (for S/N $\sim$ 100 and 2 pixels/resolved element)	7 - 18 ms
Acquisition rate (1024 x 1024 pixel^2 @5 Mpixels/sec)	3 frames$\cdot s^{-1}$

Table 1.1: IBIS Instrumental Characteristics

4. Large Field of View:
   the Field of View (80" in diameter) is large enough to study active regions too;

5. Short exposure time $\Longrightarrow$ High spatial resolution.
   The instrumental transparency (10%-16%) is large enough to allow short exposure times of 5-20 ms. Therefore, the seeing can be frozen and the images can be corrected *post facto* for wavefront distortion (*phase diversity*), achieving a spatial resolution near the theoretic limit of the telescope;

6. High acquisition rate $\Longrightarrow$ High temporal resolution.
   As the positioning of the FPIs plates is very fast, the wavelength setting time is defined by the filter wheel repositioning time. This implies that, if a sequence of images acquired within the same line profile is desired, a mean wavelength setting time of $\sim$ 20 ms must be expected; whenever it is necessary to change the interferential filter in the configuration, the wavelength setting time may increase to 0.5 seconds.

Chapter 2

CCD and CMOS devices for solar imaging spectroscopy

Monochromatic images, acquired with IBIS, are currently recorded by a Princeton Instruments PentaMAX CCD camera. The detector is a Kodak KAF-1400 with 1317 × 1035 pixels, a dynamic range of 12 bits and an acquisition rate of 5 Mpixels$\cdot s^{-1}$.

One of the targets of this thesis was to select and study a new sensor to install on the IBIS spectral channel, in order to increase the efficiency of IBIS data acquisition. Improvements in the IBIS acquisition system, which we will examine individually below, concern an increased sensitivity/quantum efficiency, a decreased detector readout time, a larger array size and an increased full-well/programmable detector gain.

For this purpose, we selected two sensors which satisfy these requirements: the SI-1920 HD CMOS sensor and the Andor iXon DV885 EMCCD camera. In this chapter we will describe laboratory measurements of the basic operating parameters of these two sensors.

2.1 IBIS CCD system improvement

A Princeton Instruments PentaMAX CCD camera, using a Kodak KAF-1400 sensor, is currently installed on the IBIS spectral channel to acquire monochromomatic images. The size of the sensor is 1320×1035 pixels, though generally only a sensitive area of 1024 x 1024 pixels is used to record images. The nominal pixel rate is 5Mpixel/sec, though the sustained readout rate is generally only one half of this (in unbinned mode). The data is output with 12-bit accuracy and each ADU corresponds to 10.2 e , which gives an effective full well of approximately 40,000 photoelectrons. The quantum efficiency of the KAF is shown in Appendix C.

There are several areas where improvements in the IBIS acquisition system would increase the efficiency of IBIS data acquisition. The primary changes, which we will examine individually below, are:

1. Increased Sensitivity / Quantum Efficiency;
2. Decreased Detector Readout Time;

3. Larger Array Size;

4. Increased Full-Well/Programmable Detector Gain.

The exposure times used with IBIS are generally limited to approximately 10-50 milliseconds in order to ensure that during the integration the atmospheric conditions do not change. The detected photoelectron flux for the solar continuum ranges between 200 and 450 e /pixel/msec depending on the wavelength range. With an exposure time of 50 milliseconds the number of detected photoelectrons is $(1–2)\cdot 10^4$, corresponding to ∼1000–2000 ADU. The count levels inside a spectral line can be up to 5 times less. If we consider a line core intensity of 0.2 I_c (where I_c is the line continuum intensity) and an exposure time of 50 milliseconds, the number of detected photons might be as few as 2000 e or 200 ADU.

The situation is even worse when operating in a spectropolarimetric mode in which the beam is split in front of the CCD in order to provide two simultaneous images in two polarization states. In this case the photon fluxes are divided by a factor of more than two (including the other losses due to additional optical surfaces in spectropolarimetric mode). Multiple images can be combined, either by simple co-adding or through more advanced image reconstruction techniques, in order to reduce the noise levels. This requires acquiring a sufficient number of images to reach the desired photometric accuracy (more than 5 images would be required to achieve 1% accuracy in the example above).

The current CCD has a QE of between 30–40 % throughout the operating range of IBIS. Increasing this by a factor two would directly reduce the photon shot noise in the images by a factor of 1.4. This would directly benefit the quality of the image and the reliability of the spectral profiles extracted from the data scan.

Together with the low photon flux available at the IBIS detector, the low duty cycles presently achieved with IBIS combine to make the overall system efficiency somewhat low. Readout times for full resolution images are 400 milliseconds for the full 1024×1024 field of view. Taking a partial field of view of 1024×512 pixels (still at full resolution), the readout time drops to less than 200 milliseconds. Assuming an exposure time of 20 milliseconds, this leads to duty cycles of 0.05 to 0.1. This means that regardless of the detector efficiency, nineteen out of twenty photons are being lost. A CCD with a faster readout, by allowing more exposures in a given time period, would effectively allow more photons to be detected.

Moreover, the current readout speeds limit the number of spectral points that can be sampled in an observing sequence. In order to sample the full line in less than the solar evolution times, only 30 points in a line can be selected. In order to apply image reconstruction techniques, 5–10 images per wavelength are required. At the current imaging rates, this might further reduce the number of spectral sampling wavelengths that can be obtained within the solar evolution timescale.

Increasing the readout speeds of the detector by a factor of four, corresponding to a true sustained pixel rate of 10 Mpixel/sec, might be reasonable and feasible. This would correspond to an increase of four in the overall system efficiency and a factor two decrease in noise levels. A readout time of 50-100 milliseconds, would be more appropriate to the exposure times currently used with IBIS, giving a duty cycle closer to 0.2-0.5. Even faster effective readout

rates of 20-40 Mpixel/sec would provide additional advantages, but above these speeds the gains are minimal. A frame transfer CCD is another option to improve the duty cycle, but it would have to have a readout time comparable to the usual exposure times in order to provide a significant increase in efficiency. For example, for T = 20 msec, a 20 Mpixel/sec, full frame CCD would provide 14 frames/sec while a frame transfer device of the same speed would allow as many as 20 frames/sec.

It should be noted that a faster camera system for the narrow-band channel would require a similarly fast camera for the "broad-band" channel. This broad-band camera may not have such stringent requirements in terms of quantum efficiency or linearity, but it will require some consideration to fit such a camera into the current system. This includes both mechanical constraints and issues concerning the data flow through the current CCD control system. A sustained data rate of 10 images per second with a size of 1k×1k and 2 byte/pixel implies a data rate of 70 GB/hour. This is for a single camera, implying that IBIS could easily take 0.5 terabytes in a single day. However, current image reconstruction techniques benefit from acquiring more atmospheric samples, while the available spectral resolution/sampling in IBIS is similarly limited by the achievable data rate.

A larger detector would provide more imaging area at the IBIS focal plane. This would allow additional techniques, such as Phase Diversity, to be applied directly at the narrowband image plane. However, given the already low light levels with IBIS, it would appear to be preferable to use a separate system on the parallel optical bench to measure the atmospheric distortions through Phase Diversity techniques. Both the PD camera and the IBIS camera would be exposed strictly simultaneously through a common shutter. The distortions measured in the PD channel could then be applied to the reconstruction of the narrowband IBIS images. This is the heart of the Multi-Object Multi Frame Blind Deconvolution technique. This would avoid additional splitting of the already weak narrowband beam and provide maximum flexibility in the experiment setup.

A larger detector would also allow the full image to be observed in both polarization states when using spectropolarimetric mode. The current setup provides a quasi-rectangular image of 42"×80" selected from the center of the field. The full field is approximately 0.7 times larger than this area. While this would be advantageous, it would probably require the acquisition of the new polarizing beamsplitter setup since the current design provides a fixed separation.

The current detector has a full well of 40,000 e which allows a maximum signal to noise ratio of 200:1. With a 12 bit digitization and 10 e /ADU, the useful detector range is well sampled and the photon shot noise is above the other noise sources for signal levels above several hundred photoelectrons. However, there might be cases where a higher signal to noise level is desired and having a larger available full well would be useful. Some examples would be the search for faint polarimetric signals that require signal to noise levels of 1000:1. This requires the accumulation of at least 10^6 photons, which would require summing 25 exposures with the present camera, ignoring the reduced intensity as one scans through a spectral line.

Two different systems, the SI-1920 HD CMOS sensor and the Andor iXon DV885 EMCCD camera (see Appendix C), have been selected as better meeting

the above requirements. A description of the basic principles of EMCCD and CMOS sensors is reported in Appendix B

2.2 Characterization and calibration of image sensors

As previously stated, two sensors, the SI-1920 HD CMOS sensor and the Andor iXon DV885 EMCCD camera, have been selected to replace the current CCD camera installed on the IBIS spectral channel. In this section we describe laboratory measurements of the basic operating parameters of the two selected cameras. Accurate quantitative estimates of the characteristics of a camera system are necessary for the reduction of images to standard photometric data. The gain, readout noise and full well capacity are most commonly measured by analysis of the photon transfer curve, which is explained in theoretical detail by Janesick (2001). In the following section we give a derivation of the simplified method we used in practice.

2.2.1 Photon Transfer Curve

The digital signals recorded by the CCD/CMOS sensor, usually called data numbers (DN) or A/D units (ADU), need to be changed into microvolts and then into electrons and finally into photons in order to calibrate the system. The relation between ADU and microvolts at the camera output depends on the gain of the amplifiers in the system and the conversion from microvolts to electrons is related to the capacitance of the output node of the amplifier. The ADU produced by the camera system are linearly related to the numbers of electrons by the following expression:

$$S_0 = GN_e + b \tag{2.1}$$

where S_0 is the recorded output signal in ADU, N_e is the number of electrons, G is the gain or transfer factor expressed in ADU/electrons and b is the electronic offset or bias level.

The parameters to be determined are the readout noise and the gain G. This factor corresponds to the output signal in ADU for an electron accumulated in the pixel and depends on the geometrical properties (surface and perimeter) of the readout diode. As concerns the noise, for a CCD/CMOS sensor there are different noise sources:
- Read noise (R), measured in absence of signal.
- Photon noise (p), associated to the photons falling on the sensor. This noise follows a Poisson statistics.
- Noise due to pixel non-uniformity.

If we remove the pixel non-uniformity, since the noise sources are independent and random they add together in quadrature, so that the total noise (N) is given by:

$$N^2 = p^2 + R^2 \tag{2.2}$$

The noise squared (N^2) is the variance. It is important to realize that this expression applies to photoelectrons and not to ADU counts, but the measured

quantities (S_m and V_m) are in ADU. S_m is the mean, bias-subtracted signal, in counts, while V_m is the variance, the square of the standard deviation (or noise) of a single observation from that mean.

To convert from electrons to ADU we need to multiply each noise term by G, to obtain:

$$(G \cdot N)^2 = (G \cdot p)^2 + (G \cdot R)^2 \tag{2.3}$$

The first term is the observed variance in ADU (V_m). The photon noise p is the square root of the mean number of photoelectrons (S_m/G), so $p^2 = S_m/G$. We obtain:

$$(V_m) = (G \cdot S_m) + (G \cdot R)^2 \tag{2.4}$$

This is the equation of a straight line of slope G and intercept $(G \cdot R)^2$. This method of deriving G and R is known as the *variance method* or the *photon transfer method*. At the lowest signal the noise is dominated by the fixed readout noise whereas for larger signals the dominant noise is the photon one. At very large signals the sensor begins to saturate and the noise actually falls. In fact, if we plot the rms noise against the signal, in a logarithmic scale, we obtain a typical curve in which we can identify two regions: a first region, relative to low signal values, dominated by the read noise and a second region, for higher signals, with slope 1/2 and related to the photon noise. This is evident from Eq. 2.4 in which, for high signals, we can neglect the $(G \cdot R)^2$ term. By extracting the square root of both terms and considering their logarithm we obtain:

$$log(rms) = \frac{1}{2} \cdot log(S_m) + \frac{1}{2} \cdot log(G) \tag{2.5}$$

In a logarithmic scale we obtain a straight line of slope 1/2 and intercept G. Experimentally, the photon transfer curve is obtained in the following way:

1. Take a bias image (dark frame with t=0);
2. Take two images for each exposure time I_1 and I_2 and repeat the procedure for different times;
3. Calculate the mean image;
4. For each illumination level the mean dark-subtracted image is computed in a sub-region of the sensor free from artifacts (100 $\times$100 pixels);
5. Compute the difference between the two images I_1 and I_2 and divide the resulting image by $\sqrt{2}$;
6. Calculate the variance of the difference image.

2.2.2 Linearity

An important characteristic of a scientific imaging system is the linearity in response to incident light, particularly when applied for quantitative photometric analysis. Linearity indicates the exact proportionality between the amount of light falling on the sensor and the output signal.

The transfer function relating the number of photons incident on the sensor and the digital output is determined by a multi-stage process that begins with the creation and reading of charge carriers (electron-hole pairs) followed by

conversion of electrons from the charge domain into the voltage domain as an amplified voltage signal. This analog signal passes through a series of processing steps, and is further amplified before finally being digitized. With proper device design, the transfer function results in a linear variation of the final digitized output signal in relation to the amount of light incident on the sensor, such that the output signal is equal to the photon input multiplied by a proportionality constant.

The good linearity of the sensor allows us to calibrate observations of very faint objects by using shorter exposures on much brighter standard objects. Different methods can be utilized to measure sensor linearity. One of these consists in recording the output signal while varying the intensity of incident flux. Since it is difficult to vary light intensity in the laboratory with high accuracy, linearity curves are usually derived by observing a constant source with various exposure times. This method is based on the assumption that exposure times can be very accurately controlled and the 1/f noise sources are negligible.

2.2.3 Andor DV885 EMCCD camera tests

The ANDOR DV885 EMCCD camera allows us to take acquisitions at different electron multiplying gain values, that can be varied from unity up to thousands of times directly through the software. An important feature of the camera is the high pixel readout rate, that can be set from 13 MHz up to 35MHz. We studied the camera behaviour by varying only the readout rate and keeping the multiplying gain off.

Fig. 2.1 illustrates linearity plots of the Andor iXon DV885 EMCCD sensor obtained at the three available readout rates, without inserting the multiplication stage. These plots are obtained by acquiring a series of 10 images for each integration time, with nominally flat spatial profiles and associated dark frames. The output signal is calculated by averaging the dark subtracted intensity on a central region (150×150 px^2).

Although an EMCCD sensor responds in a linear manner over a wide dynamic range, when full well conditions are reached under high average illumination intensity, a nonlinear response is usually observed and saturation occurs. Saturation exists when an increase in intensity produces no further change in recorded signal. A nonlinear response also results under extremely low illumination levels.

A linear least-squares regression analysis is fit to the data and the deviation for each data point from the calculated best-fit line is determined and reported in Fig. 2.1.

In Fig. 2.2 we report the photon transfer curves for the Andor iXon DV885 EMCCD at three different readout rates (13, 27 and 35 MHz). The images from an illuminated source at a series of integration times are converted into the variance vs. signal representation as described in the previous section. From the first plot in Fig. 2.2, relative to a readout rate of 13 MHz, we can derive a conversion factor of $\simeq 1.06$ e^-/ADU and a readout noise of $\simeq 13$ e^-. The other plots reported in Fig. 2.2 are obtained by repeating the same measure with a higher readout rate (27 or 35 MHz). In such cases, the photon transfer curve deviates from a linear behaviour: for higher signals the variance increases more slowly than the output signal. We interpret this behaviour as due to an

inefficiency in the readout process. During this phase, a part of the collected charge is not transferred from one pixel to another, causing a smoothing in the signal fluctuations.

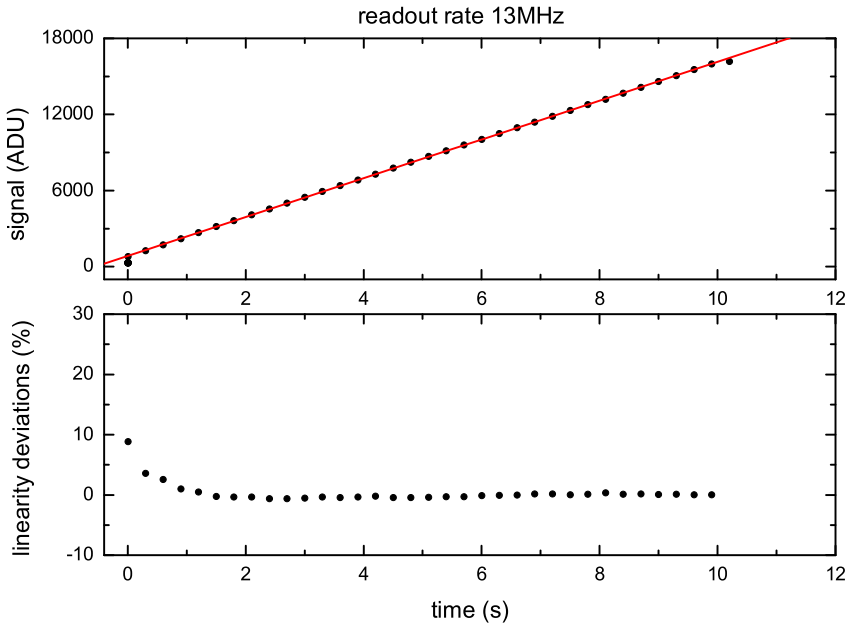
readout rate 13MHz
signal (ADU)
18000
12000
6000
0
0
2
4
6
8
10
12
linearity deviations (%)
30
20
10
0
-10
0
2
4
6
8
10
12
time (s)

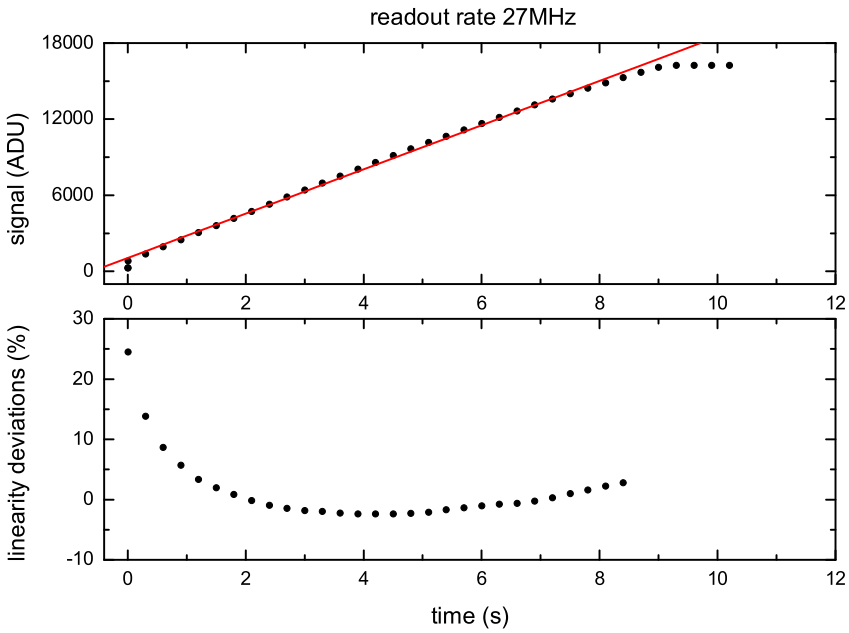
readout rate 27MHz
signal (ADU)
18000
12000
6000
0
0
2
4
6
8
10
12
linearity deviations (%)
30
20
10
0
-10
0
2
4
6
8
10
12
time (s)

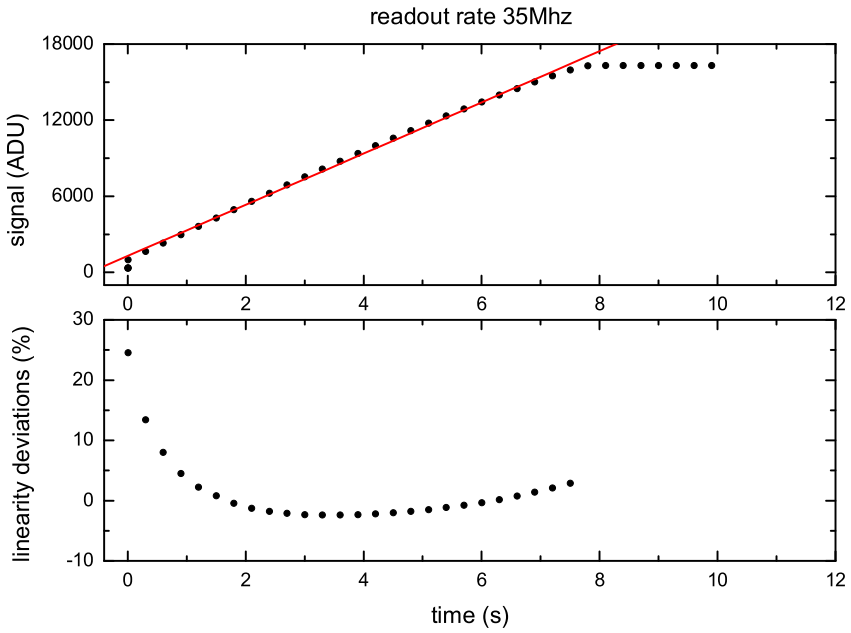

Figure 2.1: Linearity plot of the Andor's iXon DV885 EMCCD sensor at three different readout rates (13, 27 and 35 MHz). Deviations from linearity are reported in the bottom panel.

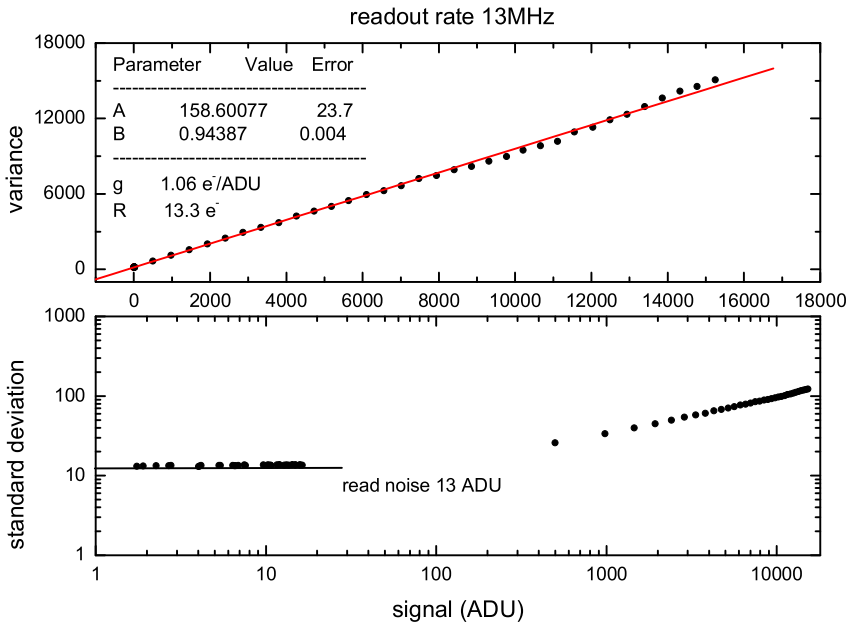
readout rate 13MHz
Parameter Value Error
A 158.60077 23.7
B 0.94387 0.004
g 1.06 e-/ADU
R 13.3 e-
variance
standard deviation
read noise 13 ADU
signal (ADU)

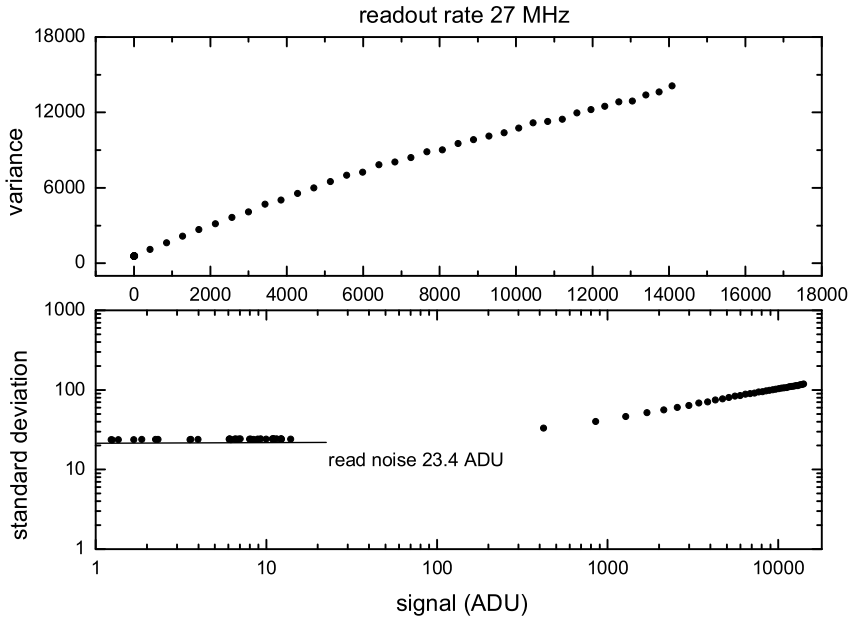
readout rate 27 MHz
variance
standard deviation
read noise 23.4 ADU
signal (ADU)

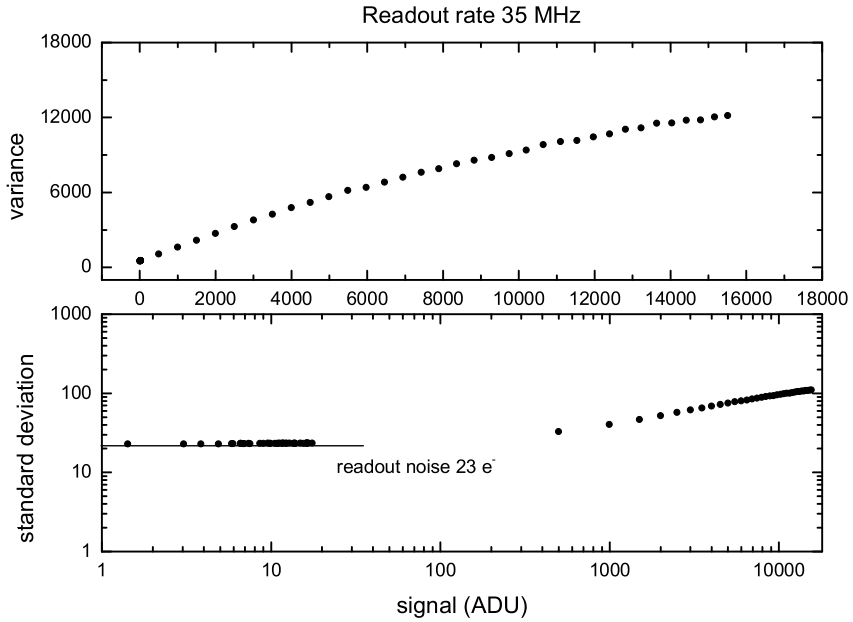

Figure 2.2: Photon Transfer Curve of noise versus signal for the Andor's iXon DV885 EMCCD camera at three different readout rates (13, 27 and 35 MHz). A variance plot (*top*); a logarithmic plot (*bottom*).

2.2.4 SI-1920 HD CMOS sensor tests

In Fig. 2.3 we report the linearity plot of the SI-1920HD CMOS sensor. In this case we built the linearity curve by varying the incident lamp light by using various calibrated densities. Having fixed the exposure time to 100 ms, for each density we repeat our measures 100 times, in order to remove possible sources of temporal noise. The output signal is calculated by averaging the measured intensity on a central region (150×150 px^2).

A linear least-squares regression analysis is fit to the data and the deviation for each data point from the calculated best-fit line is determined and reported in Fig. 2.3.

The photon transfer curve for the SI-1920HD CMOS sensor is shown in Fig. 2.4. We obtain a conversion factor of $\simeq 13.2$ e^-/ADU and a readout noise of $\simeq 3.6$ e^-.

The values of G and R obtained from our measurements are summarized in the following table (Table 2.1).

	Andor DV885			SI-1920HD
G (ADU/e^-)	0.94			13.2
R (e^-)	13 at 13MHZ	23.4 at 27MHZ	23 at 35MHz	3.6

Table 2.1: Values of G and R measured for the two selected cameras

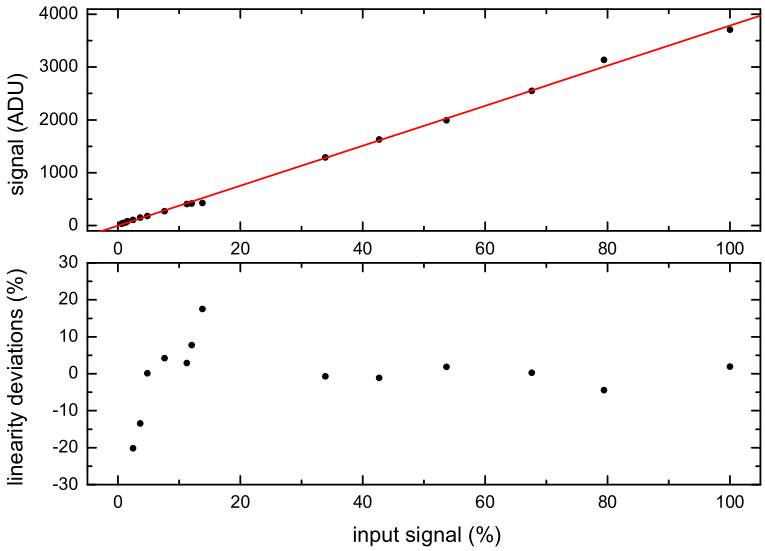

Figure 2.3: Linearity plot of the SI-1920HD CMOS sensor (*top*). Corresponding deviations from linearity (*bottom*)

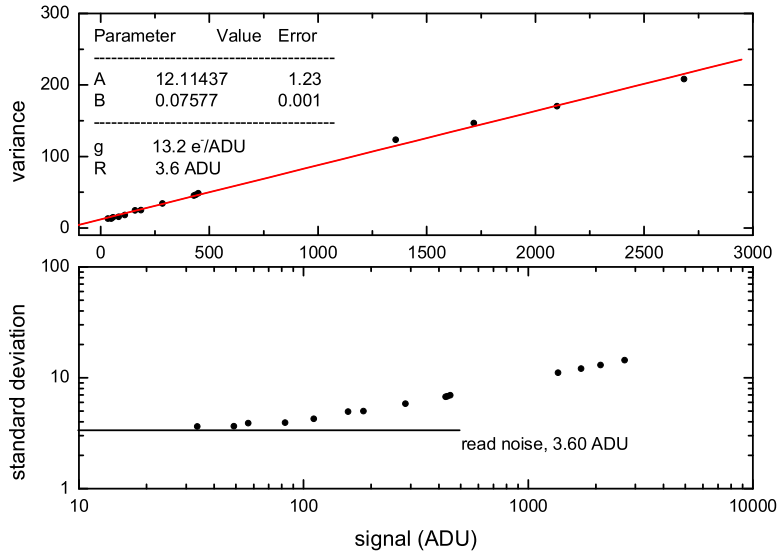

Figure 2.4: Photon Transfer Curve of noise versus signal for SI-1920HD CMOS sensor. A variance plot (*top*); a logarithmic plot (*bottom*).

Chapter 3

Pipeline for IBIS data processing

To support IBIS and for the analysis of high resolution solar images we collaborated in implementing an image processing pipeline including both a standard image calibration and a high performance IDL software package developed specifically for high resolution solar images.

Generally, image processing includes two steps. The first one, usually referred to as pre-treatment, consists in correcting raw images, in FITS format, for dark current, CCD non-linearity, flat field and blueshift. The output of this initial process is a set of Basic Calibrated Data (BCD). The second step consists in implementing an advanced calibration (image displacement correction, temporal sampling correction, image restoration, non-linear fitting of spectral lines, subsonic filtering, image segmentation, feature tracking) depending on the analysis to be carried out. In this way a set of Advanced Calibrated Data (ACD) is obtained.

3.1 Image pre-treatment

The first step in the data reduction is to correct individual raw images, in "ADU" units, for some spurious effects that are accumulated in the image during the acquisition process. This correction is usually referred to as the pre-treatment as it has to be undertaken prior to any further calibration process.

Generally, the raw images recorded by the CCD (or CMOS) camera show intensity variations across the field of view that are not due to the solar image, but rather caused by instrumental effects that alter the observed intensity in each point of the field of view. Some of the possible causes for the variations in instrument response are:

- inhomogeneities in the CCD response for each pixel, including noticeably hot or cold pixels: quantum efficiency and full well capacity can vary across the photo-sensitive surface of the sensor;
- fringes produced by the various optical elements in the path;
- optical vignetting across the imaged area;

- ghost images or spurious reflections;

While the first two effects are generally considered to be of multiplicative nature in the spatial response of the sensor, the last two give rise to a signal which adds to the values of pixels. Their correction needs a more accurate analysis that we do not discuss here.

Regarding the multiplicative effects, they can be calibrated by applying the *flat-fielding* technique, which takes the intensity response of individual camera pixels into account. The name indicates the final aim of the procedure, to measure the spatial response of the detector in the case of a *flat field*, i.e. a field whose flux is perfectly uniform in all points. The information on where the observed intensity has to be reduced or increased is recorded in a matrix, called *gain table*, with the same size as the images taken by the camera. The gain table is used to compensate for the intensity response instrumental effects that alter the observed intensity in each point of the field of view.

To apply the *flat-fielding* technique, we have to take the so-called flat-field (ff) and dark-current (dc) images. The first are images of a uniform source obtained in the same observing conditions as the astronomical images. Dark current are taken by obstructing the light path which forms the astronomical image. It is very important to take these images very close in time and in the same observing conditions as the astronomical images. To use a lamp with a diffusive glass plate or to defocus the telescope in order to provide a uniform source of illumination is not recommended because the observing conditions are changed significantly. Good *flat field* images are obtained by taking many images while moving the telescope at high speed, randomly scanning areas near the center of the solar disc. The average of all these images, which are smeared by the effect of the telescope motion, cancels all structures of solar origin, but many images (100 or more) are needed for a good result.

Generally, the algorithm applied to compensate the above described effects in a raw astronomical image $i_{raw}(n, m)$ is the following:

$$i_{corr}(n, m) = \frac{i_{raw}(n, m) \quad dc(n, m)}{ff(n, m) \quad dc(n, m)} \tag{3.1}$$

where *flat field* images are normalized by their mean value in order to preserve the photometry.

Regarding the IBIS data reduction, the first step is to remove dark current and CCD non-linearity effects from both the data and the flat-field images. The dark current represents the residual intensity observed without illumination and produced by the temperature of the chip, depending only on the exposure time. This residual signal is removed by simply subtracting a mean dark current value, obtained by averaging more dark frames taken with no illumination, from each observation.

Regarding the flat field correction we cannot simply apply Eq. 3.1, but a more careful approach is required. First of all, as we are observing spectral lines, there is an additional variation in the recorded data cube given by the variation in flux at different points along the spectral line. To take this effect into account, it is necessary to acquire many flat field images (generally 100) at the same wavelength as the science data and in the same optical configuration. All the *flat field* images, relative to the same wavelength, are then averaged to

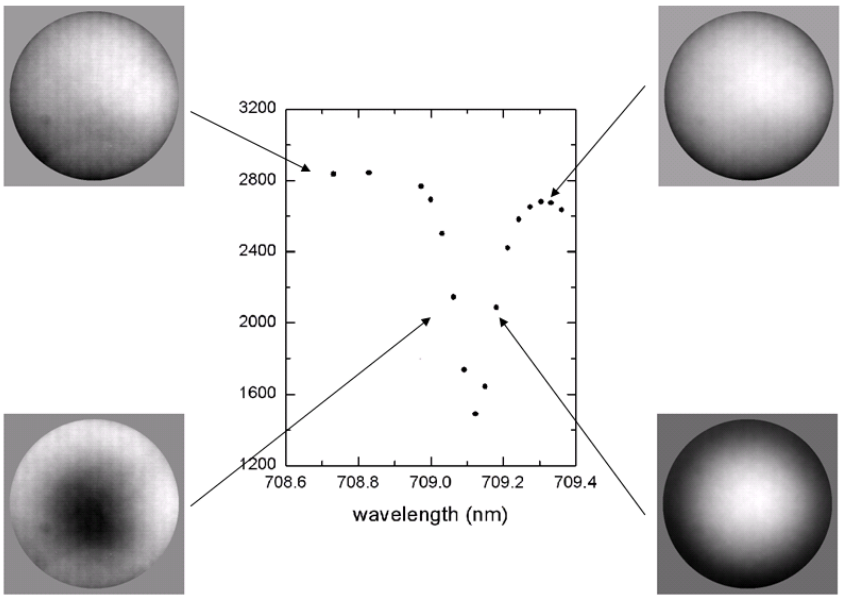

Figure 3.1: The profile of the Fe I spectral line at 709.0 nm obtained with IBIS and flat field images taken at selected wavelength positions. The intensity modulation, produced by a radially dependent blueshift, is evident in all shown images.

reduce the visibility of spatial structures on the Sun even more, producing a "flatfield scan".

Another effect observable in the field of view of IBIS data is a spatial intensity modulation, produced by a radially dependent blueshift (Fig. 3.1). Such an effect is due to the classical mounting of the two Fabry-Perot Interferometers. In this configuration every image point corresponds to rays with a specific angle with respect to the optical axis propagating through the FPIs (see Chapter 1). This causes a systematic blueshift of the instrumental profile when moving from the optical axis towards the edge of the FoV, therefore reaching its maximum on the outermost pixels. This maximum is about 60 mÅ at 6000 Å wavelength and is about 100 mÅ at 8500 Å wavelength.

As the images of the flat field sequences acquired with IBIS are not strictly monochromatic, we cannot divide flat field images by their mean value in Eq. 3.1. In this operation we have to take blueshift effects into account. For this reason, before producing the gain table, we determine the instrumental "blueshift map" by calculating the line core shifts of all the pixels in the FoV with respect to a reference profile and fitting this resulting map with a parabolic surface. The reference profile is obtained by averaging the line profiles of the pixels in a central region (100×100 pixels) of the FoV.

The next step toward the construction of the gain table is the removal of the spectral line information from the flat field images. For this purpose, an average spectral profile is constructed, by remapping all pixel profiles to a common wavelength scale, by applying the blueshift map, and then averaging. The remapping process is performed by linearly interpolating the measured spectral

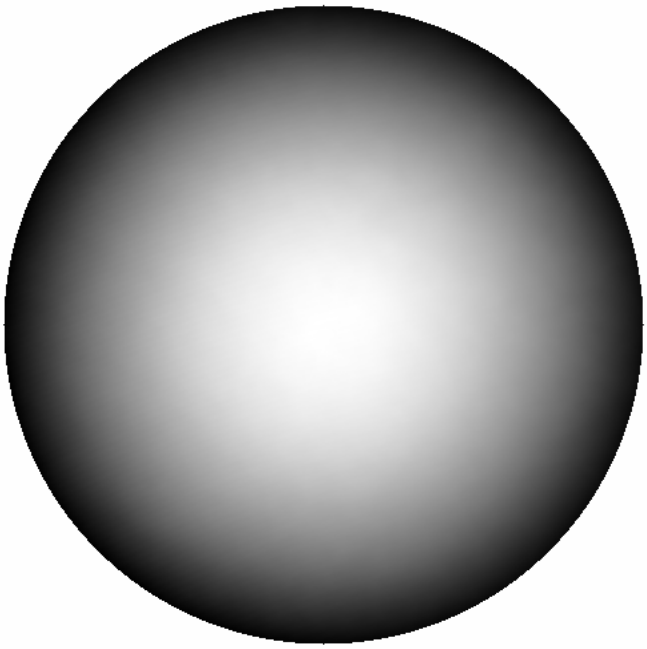

Figure 3.2: Observed instrumental "blueshift map" obtained by calculating the line core shifts of all the pixels in the FoV with respect to a reference profile.

profiles. Isolated patches of reduced intensity are strongly suppressed in the mean profile due to the large-scale averaging.

A new array is generated by applying once again the overall average spectrum on each pixel of the field and then shifting it accordingly to the calculated blueshift map. This array represents the ideal blueshifted flat field scan that is expected for a "perfect" system (i.e. with only the blueshift contribute and no gain variation). It gives the expected data array for observations of a homogeneous field by a system with perfectly uniform response. This ideal blueshifted flat field scan can then be compared to the observed averaged spectral scan, with the differences indicating variations of the system response at that physical location and wavelength.

The final gain table scan is constructed by dividing the flat field scan by the ideal blueshifted flat field scan, so that it does not contain unwanted spectral information. Only individual camera pixels with reduced or enhanced intensity show up in the gain table, as the shape of the spectrum is the same in both measured and synthetic scans. The gain table is then applied to the raw data in order to correct each pixel for the flat field response. Finally, the blueshift correction for the flat fielded data is computed and applied with the same process used for the flat fields.

3.2 Correction for image motion

To study the dynamics of solar features (e.g their life-times, proper motions, oscillations, morphological or photometric evolution) time series of high resolution images are necessary. If we display images of a time series as a movie we observe a global agitation referred to as *image motion*. Each image is globally displaced with respect to one another. Images in a time series are globally displaced with respect to one another. This movement is due to the overall wavefront tilt induced by atmospheric turbulence and by mechanical vibrations in the telescope. To compensate such displacements we can compare each image with a reference image $i_R(q)$, by applying cross-correlation techniques. Thus, for the j-th frame of the series, $i_j(q)$, the cross-correlation is:

$$C(\delta) = \int i_j(q) i_R(q+\delta) dq \tag{3.2}$$

Since the maximum of the correlation represents the best match between both images, the position δ_{max} of this maximum gives the relative displacement of $i_j(q)$ with respect to $i_R(q)$. Therefore, shifting $i_j(q)$ by δ_{max} the displacement will be compensated. If the observed structures do not evolve significantly during the whole sequence, we can use the first image of the series or an average of all images as reference image. Nevertheless, if structures evolve on a time scale smaller than the duration of the series, we first perform a comparison of consecutive images, two by two. The cross-correlation between the images $i_j(q)$ $i_{j\ \ 1}(q)$ gives the displacement, $\delta_{(j,j\ \ 1)}$, of the former relative to the latter, and the vectorial summation of displacements,

$$\delta_j = \sum_{k \leq j} \delta_{k,k\ \ 1} \tag{3.3}$$

gives the cumulative displacements of $i_j(q)$ relative to the first image of the series. Thus, all frames are realigned to the first of the series.

3.3 LoS velocity maps

A single scan from a tunable 2-D filter instrument provides an observer with a spectral line profile at each pixel of the image. These line profiles can be used to derive the line-of-sight (LoS) velocity, which is one of the most important quantities which one can determine from a spectroscopic measurement. Vertical velocity fields are obtained by computing the wavelength shifts of the line core with respect to a reference wavelength: for each pixel a Gaussian fit of the line profile is evaluated. The shift of this Gaussian function relative to a reference mean line profile can be interpreted as Doppler shifts:

$$\Delta\lambda_D = \frac{\lambda v}{c} \tag{3.4}$$

where λ is a reference wavelength, c is the speed of light and v is the velocity of the solar plasma generating the line spectral line. If the source is moving away from the observer the observed wavelength is greater (red-shifted), and if the source is moving toward the observer the wavelength is shorter (blue-shifted).

A Doppler shift gives us the line-of-sight component velocity of the plasma. If the source is located at the solar disk center, as in our case, this velocity measure corresponds to the vertical motion of the plasma. However, if the signal comes from the location away from the disk center the observed line-of-sight velocity contains both the vertical and horizontal velocity component of the moving plasma. The magnitude of this effect depends on the heliocentric angle θ:

$$v_{LoS} = v_{\perp} cos\theta + v_{\parallel} sin\theta \tag{3.5}$$

where v_{LoS} is the observed line-of-sight velocity, and $v_{\perp}$ and $v_{\parallel}$ are the vertical and horizontal velocity components, respectively.

Line-of-sight velocities are derived from the shift of the line profile with respect to a reference position. This could be the laboratory value, but there are several practical reasons which have made this solution unpopular:

- the laboratory wavelength is not always known with sufficient precision;
- relative motions between the Sun and an observer, which includes the Earth's rotation and orbital motion and the solar rotation, need to be taken into account;
- the velocities have to be corrected for the gravitational redshift and the convective blueshift.

In practice, a position of a mean line profile of undisturbed granulation or of a spot/pore is used as a reference. We decided to use a quiet granulation field as a velocity reference. In addition, all the relative motions between the Sun and an observer are automatically taken into account.

3.4 K-ω filter

It has been known for several years that the Sun is oscillating with very low amplitudes in millions of global eigenmodes. The complicated pattern of the Sun's oscillation was first observed by Leighton et al. (1962) by means of Doppler imaging observations of the photosphere. They measured small displacements in the wavelength of atmospheric absorption lines alternating between towards and away from the observer. More in detail they reported a quasi-sinusoidal variation of velocity with an amplitude of few $m \cdot s^{-1}$ and a period of around 5 min.

By studying the distribution of the oscillations in the plane of horizontal wavenumber k_h against angular frequency ω, it is evident that the power is not evenly distributed, but follows certain ridges (Fig. 3.3). It was not until 1975 that the rich mode structure of the 5-min oscillations was resolved by the Doppler observations of Deubner (1975) which covered extended areas of the Sun ($\sim 0.5 R_{\odot}$) over several hours of observing. It resulted that most of the oscillatory power is concentrated in the range of frequencies between 2.5 and 4.5 mHz and below wave-numbers of about 0.8 Mm $^{-1}$.

The discovery of the 5-min velocity oscillations in the photosphere was followed by a surge of theoretical work attempting to explain why oscillatory power with a period of around 5 minutes should be preferred over other periods. The

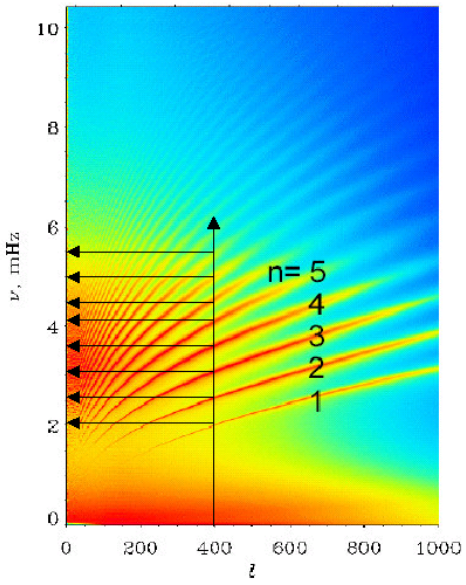

Figure 3.3: Ridges of the p modes in the l ν plane. Each of these ridges corresponds to a fixed number of wave nodes n in the radial direction.

explanation of the observed pattern in terms of standing acoustic waves trapped in cavities extending well into the interior came from Ulrich (1970) and independently from Leibacher & Stein (1971). The oscillation modes are trapped in spherical-shell cavities starting essentially at the visible surface and extending inward. The outer boundaries are defined by the abrupt change in sound speed associated with the steep temperature gradient in the superadiabatic region just below the surface. The inner boundaries result from the refraction of the waves back toward the surface, caused by the inwardly increasing sound speed (essentially, temperature). While the outer limits of all of the cavities are confined to a narrow region just below the photosphere, the depth of a given cavity depends on both the oscillation frequency and the spherical-harmonic degree of the associated mode. Consequently, there are modes whose entire cavities are confined very near the surface, while others extend much deeper, even reaching the center of the Sun itself. Depending on the frequency and degree, these modes sample different, but overlapping, regions of the solar interior. As the precise frequency of a particular cavity depends intimately on the thermodynamic, compositional, and dynamic state of the material in the cavity, they can be used to probe the temperature, chemical composition, and motions throughout the interior of the Sun.

Peaks of oscillatory power around 180 and 240 s are observed in Doppler observations of chromospheric lines such as H_α or Ca K. Also the 5-min modes are shifted to somewhat higher frequencies when a k_h ω diagram is constructed from observations in chromospheric lines. Observations of oscillations at frequencies much below 100 s are difficult because the wavelength becomes comparable to the photon mean free path in the upper photospheric line formation region.

In order to study the convection dynamics, before analyzing velocity and intensity fields, we have to take into account the 5-min acoustic oscillations, which play an important role in determining the apparent dynamics of solar granulation. They are removed by applying what is called a subsonic Fourier filter. A raw image sequence, which can be considered to be a single three-dimensional function of intensity (I_x,I_y) and time (t), is Fourier transformed into a function of k_x, k_y and ω. The subsonic filter is defined by a cone $v = \omega/K$ in $(\mathbf{k}, \omega)$-space. All Fourier components inside the cone (i.e., with phase velocities less than v) are retained, while all those outside are set to zero. Then a new sequence of images is calculated by an inverse Fourier transform. For the subsonic filter we have used a value for the cutoff velocity v of 7 $km \cdot s^{-1}$.

3.5 Velocity fields formation height

Spectral images acquired with IBIS and corresponding LoS velocity maps can roughly be associated with a given layer in the solar atmosphere. The determination of the line-forming layers can be carried out with the use of contribution functions, which give the contribution of the different atmospheric layers to an observed quantity. When studying the formation of a spectral line it is very important to distinguish between the region where the emergent radiation is originated and that where the line depression is formed. For example, if we consider the emergent radiation intensity I, we can write:

$$I(\lambda)_{\tau=0} = \int_0^\infty CF^I(\lambda, \tau) d\tau \tag{3.6}$$

The emergent intensity at $\tau = 0$ can be obtained by formally solving the radiative transfer equation:

$$\frac{\mu}{\rho}\frac{dI}{dz} = k(I(z) \quad S(z)) \tag{3.7}$$

where $\mu = cos(\theta)$ (θ is the incident angle), ρ is the gas density, z the geometrical depth, k the absorption coefficient and S the Source Function. Introducing the Optical Depth $d\tau = k\rho dz$, the solution for $\tau = 0$ is:

$$I(\lambda)_{\tau=0} = \int_0^\infty S(\tau) e^{\tau/\mu} \frac{d\tau}{\mu} \tag{3.8}$$

where $S(\tau)e^{\tau/\mu}$ is the fraction of the emergent intensity originated in the layer between τ/μ and $\tau/\mu + d\tau\mu$ i.e. the Contribution Function to I, CF^I.

Let's consider the depression in an absorption line R:

$$R(\lambda)_{\tau=0} = \frac{(I_c(\lambda)_{\tau=0} \quad (I_l(\lambda)_{\tau=0})}{I_c(\lambda)_{\tau=0}} \tag{3.9}$$

where c and l stand for the continuum and the line intensities, respectively. In such a case the Contribution Function to R has a more complicate expression:

$$R(\lambda)_{\tau=0} = \int_0^\infty S_R(\tau) e^{\tau_R/\mu} \frac{d\tau_R}{\mu} \tag{3.10}$$

where

$$S_R = \left(1 \quad \frac{S_l}{I_c}\right) / \left(1 + \frac{k_c}{k_l}\frac{S_c}{I_c}\right) \tag{3.11}$$

Line	$\chi_{ion}\,(eV)$	$\chi_{ex}\,(eV)$	$\lg(gf)$	ζ	$\xi\,(km/s)$
FeI 709.0 nm	7.87	4.231	1.3	17	1.00
$FeII$ 722.4 nm	16.18	3.889	3.3	50	1.75

Table 3.1: Line parameters used for the calculation of line profiles. ζ is a fudge factor multiplying the Unsöld value of γ in the Lorentz part of the absorption profile, while ξ is the usual microturbulence term. The values of ζ and ξ are chosen to optimize the comparison with atlas data.

and

$$d\tau_R = \rho(k_l + k_c\frac{S_c}{I_c})dz \tag{3.12}$$

Another method to derive the formation depth of a spectral line consists in studying the Response Functions (hereafter RFs) which describe the effect that perturbations of a given physical parameter have in an emergent line characteristic (Mein, 1971; Beckers & Milkey, 1975; Canfield & Stencel, 1976; Canfield, 1976; Caccin et al., 1977). For example, if RF_p^C is the response function of the feature C for a certain parameter p, the feature fluctuation that corresponds to a small disturbance Δp, can be written as:

$$\Delta C(\lambda) = \int_0^\infty RF_p^C(\lambda, z)\Delta p(z)dz \tag{3.13}$$

In short, the RF_p^I is, at each depth, the function we must use to weigh the perturbation p in order to get the variation of the emergent intensity I.

In our case, in order to associate a suitable "formation zone" to observed photospheric lines, we study their sensitivity to the perturbations of velocity, as a function of the depth. In detail, we treat the effects of linear dynamic perturbations on the line profiles and study the velocity response functions RF_v of the emergent intensity at the observed wavelengths within the lines (Caccin et al., 1977; Berrilli et al., 2002), that provide the corresponding intensity perturbation as:

$$\delta I(\lambda) = \int_\infty^{+\infty} v(z)RF_V(z, \lambda)dz. \tag{3.14}$$

The velocity response function is given (to the first order) by the following formula:

$$RF_V(z, \lambda) = \frac{\partial\chi(z, \lambda, v)}{\partial v}(S(z, \lambda) \quad I(z, \lambda))e^{\ \tau(z,\lambda)}. \tag{3.15}$$

where $\chi(z, \lambda, v)$ is the total opacity for volume unit, $S(z, \lambda)$ the source function and $\tau(z, \lambda)$ the optical depth.

The calculations have been made using Kurucz's solar atmospheric model (Kurucz, 1994) and assuming LTE, so that the source function $S(z, \lambda)$ is velocity independent. The validity of this model and of the line parameters we used (Table 3.1) is given by the comparison between the theoretical synthesis of the lines and the atlas data (Kurucz et al., 1985).

This approach, previously employed by Berrilli et al. (2002) to derive the RF_v^I for three particular spectral lines: Fe I 557.61 nm, Fe I 537.96 nm and C I 538.02 nm, has been here adopted to calculate the formation depth of the

Line	h_{core} (km)	h_{mean} (km)	$FWHM$
FeI 709.0 nm	150	100	200
$FeII$ 722.4 nm	40	40	140

Table 3.2: Line formation depth for the line center and the whole line. The latter is obtained by averaging the different RF_V computed in the sperimental wavelenghts and its FWHM is also given.

two IBIS photospheric spectral lines used in this thesis: Fe I 709.0 nm and Fe II 722.4 nm. The formation depth, i.e. the location of the maximum of the RF_V, depends on the wavelength, hence on the given points of the line profile. This dependence is more evident for the Fe I 709.0 nm line, while for Fe II 722.4 nm the RF_V maximum is almost the same for each wavelength (Fig. 3.4). Since we derive the velocity shift by a fitting procedure that uses all the experimental spectral points, we consider the mean of the corresponding RF_V. The formation heights for the average lines are reported in Table 3.2. The major contribution to the formation of these absorption lines comes from layers 100 km and 200 km above the photospheric surface, respectively.

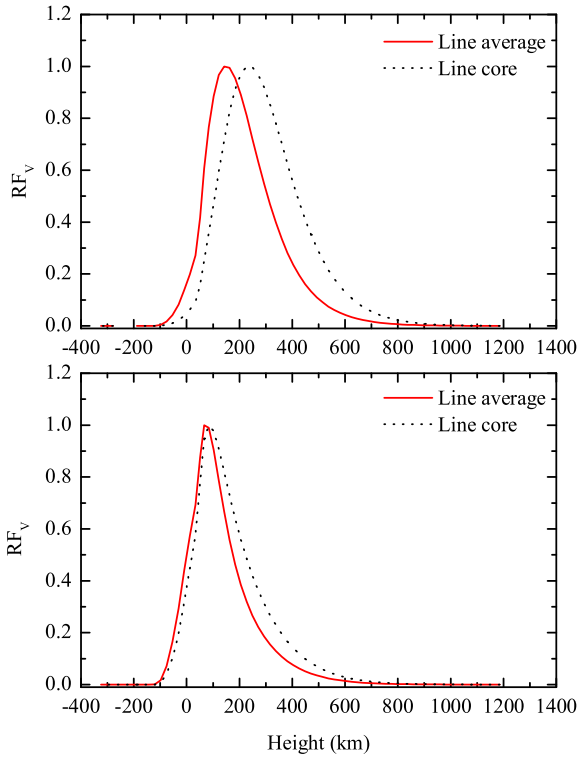

Figure 3.4: Velocity response functions for the Fe I 709.0 nm (*top*) and Fe II 722.4 nm (*bottom*) lines relative to line core (*black dotted*) and mean line profile (*red continuous*). $RF_v{}^I$s are in arbitrary units.

Chapter 4

Scientific results

The inhomogeneous and structured aspect of the solar photosphere basically originates from the interaction between convective flows, conveying energy from the deeper layers of our star, and the magnetic field, emerging at the surface. The photosphere shows a wide variety of magnetic features, ranging from the largest sunspots, with field strengths up to several kG, down to the 0.1 Mm scale magnetic elements, with typical field strengths of $\simeq$ 1500 G.

The scientific subject of the thesis is the study of the emergence and organization of the magnetic field on the solar surface both as isolated structures and as clusters. Pores are one of the various isolated features forming in the photosphere by the emergence of magnetic field onto the solar surface. Their uniqueness is that they lie at the border between tiny flux tubes, associated with magnetic elements, and complex regions, associated with sunspots.

In the first section of this chapter we report results obtained by investigating the photospheric structure of a roundish pore with a light bridge, possibly formed by the quasi-merging of two pores of the same polarity, as derived from the previous day MDI/SOHO magnetograms and continuum images. The analysis has been carried out by using both broad-band and monochromatic images, referring to a photospheric layer, acquired with the Interferometric BIdimensional Spectrometer (IBIS). More in detail, we focus our study on the pore LoS velocity and mean radial structure and on intensity and velocity small scale properties of a light bridge.

By adopting the same IBIS dataset, we studied the oscillatory properties of the quiet and active solar chromosphere in relation to the underlying phtotosphere, with particular regard to the effects of the magnetic topology. In particular, we analyzed the propagation of waves in the atmosphere in correspondence of a pore, of a magnetic network area and of a quiet Sun region.

In the last part of this chapter we present recent results about the organization of magnetic fields in the quiet Sun, obtained by applying a void-searching algorithm to a time-series of MDI magnetograms. This algorithm, capable of detecting voids between magnetic fragments, allowed us to study the scale distribution of magnetic intercluster voids.

4.1 Imaging spectroscopy of a solar pore

The most prominent recurrent magnetic structures in the photosphere are the sunspots, with typical field strengths of ≃3000 G. A closer inspection with higher spatial resolution reveals the presence of 0.1 Mm scale magnetic elements, with typical field strengths of ≃1500 G. In this family of solar magnetic structures, pores represent the link between the transient small-scale flux concentrations and full-fledged, long-lived sunspots.

Magnetic structures on the solar surface aare classified into small-scale and large-scale, depending on their organization: sunspots and pores are large-scale coherent structures, whereas the other types consist of individual (unrelated) patches of magnetic flux, even if they can cover the same or even a larger area than a sunspot. Only large-scale coherent structures appear darker than their surroundings due to the suppression of convection.

Pores are the smaller version of sunspots, which share some of their properties, but also differ markedly in others. The term is attributed to intense magnetic flux concentrations, typically ≃1700 G, of larger scale (1000 to 6000 km), which appear much darker than their surroundings due to the suppression of convection by the magnetic field.

Pores have been found to form by the accumulation of flux swept towards them by converging horizontal flows (Leka & Skumanich, 1998; Hirzberger, 2003). Across a pore, the magnetic field strength exhibits a variation from 600 G to 1700 G, as reported by Sutterlin et al. (1996) and Leka & Skumanich (1998). This behaviour was confirmed by Keppens & Mártinez Pillet (1996) who, by measuring the magnetic structure in a large number of pores by means of Advanced Stokes Polarimeter data, found a decrease of the vertical magnetic field component from 1700 G, in the pore center, to 900 G at its magnetic edge. More in detail, magnetic field lines are found to be roughly vertical in the center of pores, while they are inclined by about 40° 80° at their boundaries.

Most recent MHD simulations (Cameron et al., 2007) of an isolated pore roughly reproduced these values, rendering a central vertical field of 2.5 2.0kG, which decays to 1.5kG at the visible boundary of the pore (1.1 Mm in that simulation), where the field inclination value reaches $\sim 50°$.

In Table 4.1 we summarize typical parameters of sunspots and pores, taken from the papers by Mártinez Pillet et al. (1999), Sutterlin & Wiehr (1998), and Keil et al. (1999): the spot visible diameter D_{vis}, the minimum umbral intensity I_{min}, the magnetic field strength at the center of the umbra $B(0)$ and at the visible boundary $B(R_{vis})$ and the magnetic field inclination at this boundary $\gamma(R_{vis})$. For a review about pores and sunspots see Sobotka (2003) and Thomas & Weiss (2004).

Concerning the formation of pores and sunspots, from observations (e.g., Wang & Zirin, 1992; Keil et al., 1999) it results that they form from the merging of small magnetic elements, driven by supergranular and subsurface flows. After a pore has formed, it is surrounded by a ring of downflows, i.e. the gas is streaming downwards all along the boundary between the dark pore and the bright granulation (e.g., Keil et al., 1999; Tritschler et al., 2002; Sankarasubramanian & Rimmele, 2003). The flow has been found to be organized into thin needle-like structures, with the pin pointing towards the pore (Sankarasubramanian & Rimmele, 2003) and to be time-variable (Hirzberger, 2003). The numerical simulations of Knölker & Schüssler (1988) or Steiner et al. (1998),

Parameter	Pores	Sunspots
$D_{vis}(Mm)$	1–6	6–40
$I_{min}(I_{ph}=1)$	0.2–0.7	0.05–0.3
B(0)(G)	1700	3000
B(R_{vis})(G)	1200	800
$\gamma(R_{vis})$	40° 60°	$\sim 70^\circ$

Table 4.1: Typical parameters of sunspots and pores

in which the interaction of magnetic elements with granulation were modeled, predict the development of persistent downflows at the boundary of flux concentrations. The flows are driven by the radiative cooling of the hot granular material, which can effectively radiate energy away into the less dense evacuated flux concentration. After cooling, the material condenses and starts to submerge.

Sunspots and pores are distinguished by the presence or not of a penumbra: sunspots develop a penumbra while pores do not. In young and irregular spots, often only some parts of a penumbra are developed. Near large pores, some transient filamentary structures resembling penumbra can be observed. Pores may develop into full-scale sunspots by forming a penumbra. The evolution presumably is triggered by the inclination of the magnetic field lines to the surface, which influences the ability to maintain overturning convection in the surroundings. The opposite effect may happen at the end of a sunspots' decay: the spot may loose its penumbra and only a dark umbra similar to a pore is left.

The dark appearance of pores and sunspots is classically interpreted as due to the inhibition of the transport of energy by convection, which characterizes the rest of the photosphere. The deficit of energy transport in pore and sunspot umbrae is the most dramatic manifestation of the interaction between magnetic fields and convection. However, the structure of pore umbrae is not uniform, in fact they exhibit significant variations of continuum brightness in the range between about 30% and 120% of the mean photospheric intensity, I_{phot} (Bonet et al., 1995).

From high spatial resolution observations bright structures (umbral dots and light bridges) are clearly visible inside sunspot and pore umbrae. These structures might be a manifestation of convective motions not completely inhibited in the subphotospheric layers.

Umbral dots are small, bright structures embedded in the darker umbral background with sizes ranging from 0.2" to 0.8". The histogram of sizes shows that the number of dots increases with decreasing size down to the resolution limit (Sobotka et al., 1997). Their lifetimes range from 10 to 40 minutes, with only 1% living longer than 2 hours (Sobotka et al., 1997). Observations show that umbral dots move horizontally within the umbra with speeds from 0 to 800 ms ^{1}.

Light bridges (hereafter LB) are bright irregular elongated features that divide the umbra of sunspots or pores (Sobotka, 2003; Thomas & Weiss, 2004), manifesting a great range of variability in their morphology and physical properties. It is self-evident that the plasma in a LB is hotter than its surroundings because of its brightness; how this excess temperature is maintained is less obvious. A first interpretation of photospheric LBs came from Vásquez (1973), who

accounted for them as the result of sunspot decay preceding the restoration of the granular surface. Hirzberger et al. (2002) suggested a magneto-convective origin for the LBs, deducing that the presence of the magnetic field reduced the intensity fluctuations of the convective pattern. This findings were supported by Rimmele (1997), who measured a positive correlation between brightness and upflow velocities in a LB.

Observations indicate that LBs have a weakened field, compared to the nearby umbra, and that field strength increases while inclination decreases with height, suggesting that the background magnetic field closes above the LB in a canopy-like configuration (Jurĉák et al., 2006). The magnetic canopy (Leka, 1997) forms when a field free region intrudes into the pore umbra, so that the magnetic lines fan out over such a region, to be eventually forced into a vertical direction again by the same polarity magnetic field expanding likewise from the other part of the umbra. There are no systematic findings about the vertical velocities on LBs (Leka, 1997), but, as already said, a correlation between brightness and upflow has been reported by Rimmele (1997), supporting the idea of a sub-photospheric convection origin for the LBs. A most recent work by Bharti et al. (2007a) showed a LB velocity structure to be constituted by two $500/\quad 1400 m \cdot s^{-1}$ downflows running alongside a $+200 m \cdot s^{-1}$ upflow.

Knowing the physical processes responsible for the fine structure of pores and sunspots is important for understanding their subphotospheric structure. Two classes of theoretical models are currently considered to be compatible with observations: the monolithic and inhomogeneous flux tube model (e.g., Choudhuri, 1986) and the cluster model, sometimes also referred to as "spaghetti model" (e.g., Parker, 1979a). Both models, although starting from different assumptions, can be used to explain the heating of umbrae as well as the existence of fine and bright features embedded in the dark umbra. In the monolithic model, a sunspot (pore) is considered as formed by a monolithic but inhomogeneous flux tube with magnetoconvection inside, models of which describe the modification of plasma flows by the magnetic field and vice versa. In this case, observed fine features are related to convective motions not completely inhibited in the sub-photospheric layers. The cluster model describes a sunspot (pore) as formed by a tight bundle of isolated thin flux tubes, separated by field-free plasma which can penetrate into layers near the visible surface. This "cluster" or "spaghetti" model was proposed by Severnyi (1965) and by Parker (1979a,b). In this model umbral dots and light bridges can be explained as radiative signatures of field-free columns of hot gas penetrating from below into the photosphere (Choudhuri, 1992).

4.1.1 Observations and data processing

The data presented in this chapter were acquired on September, 28th 2005 at the 0.76 m DST in Sunspot, New Mexico. We observed a central region of the solar disk including a pore with light bridge (AR10812). The observation was carried out with the IBIS 2D-spectrometer (cfr. 1.4) installed at the Dunn Solar Telescope, Sacramento Peak, NM, USA.

The dataset consists of 200 sequences, containing a 16 image scan of the Fe I 709.0 nm line, a 14 image scan of the Fe II 722.4 nm line and 6 spectral images of the Ca II 854.2 nm line (one line core image and 5 line wing images). The exposure time for each monochromatic image was 25 ms. The CCD camera

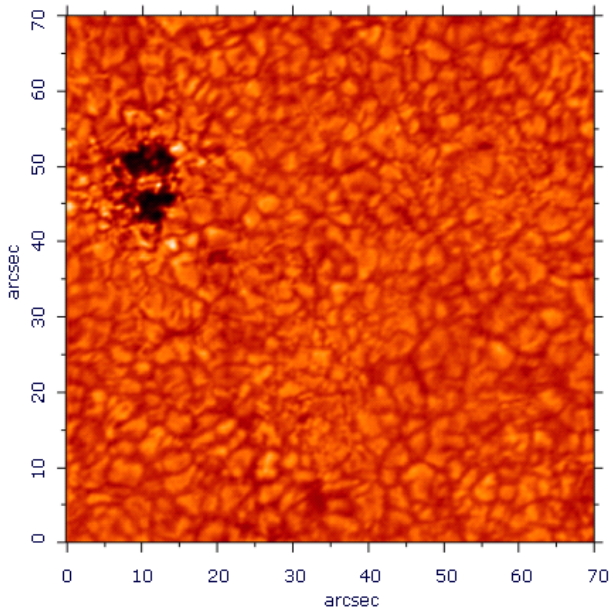

Figure 4.1: Broad-band image of the observed FoV, including the pore, after applying a Multi Frame Blind Deconvolution restoring program (van Noort et al., 2005)

.

was rebinned to 512 ×512 pixels, so that the final pixel scale for the images was 0.17"·pixel ^{1}. The time interval between two successive images and two successive spectral series was 0.3 s and 14 s, respectively.

In addition to the narrow-band images, G-band (λ =430.5 nm) and broad-band (λ =721.5±5nm) images (Fig. 4.1) were simultaneously recorded.

Each image was corrected for CCD non-linearity effects, dark current, gain table, monochromatic flat-field and blue shift (see Chapter 3). Vertical velocity fields were computed for the Fe I and Fe II lines by computing the Doppler shift: for each pixel a Gaussian fit of the line profile was evaluated. The shift of this Gaussian function, relative to a reference mean line profile, produced the Doppler shift, while the amplitude of the Gaussian produced the center line intensity fields. The 5-minutes oscillations were removed from the velocity fields applying a 3-dimensional Fourier filter in the K_h ω domain with a cutoff velocity of 7 km·s ^{1}.

After the whole reduction procedure, we consider a region of interest centerd on the pore(Fig. 4.2) of about 24"×24". This is the region tracked by the adaptive optic system, so we are confident that it is characterized by a high spatial resolution. In our analysis, we neglect the velocity offset due to the convective blueshift (Keil et al., 1999) and define absolute values by setting to zero the mean velocity of the quiet granular field. The Contribution Functions for Fe I 709.0 nm and Fe II 722.4 nm lines (§3.5) were calculated by Penza et al. (2004). The major contribution to the formation of these absorption

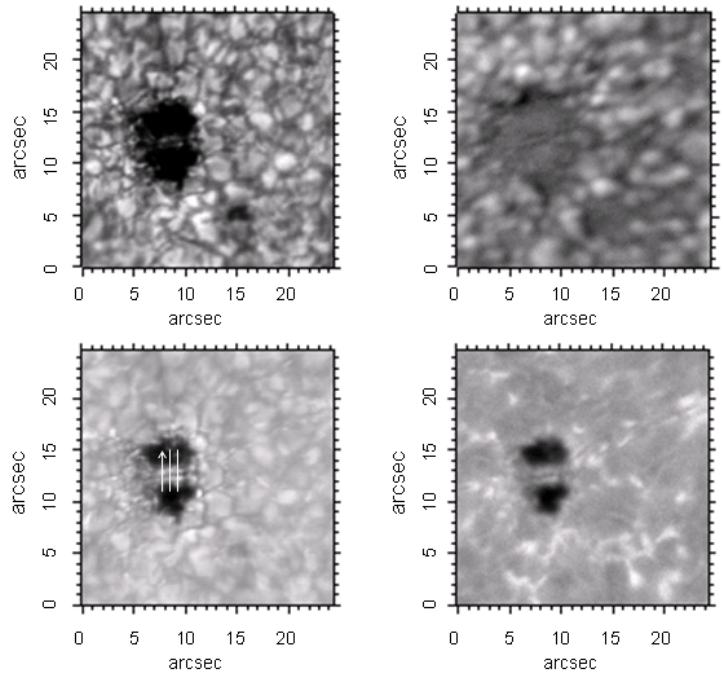

Figure 4.2: A representative synoptic panel of the analyzed sub-region. Upper left panel: broad band intensity image. Upper right panel: Doppler velocity field computed from Fe I 709.0 nm line scan. Lower left panel: G band intensity image. Lower right panel: Ca II wing intensity image. The white segments orthogonal to the light bridge in the lower left panel denote the cuts across which the intensity and velocity profiles plotted in Fig. 4.8 have been computed.

lines comes from layers 100 km and 200 km above the photospheric surface, respectively. The Ca II 854.2 nm chromospheric line forms at $\simeq$ 800 km above the photosphere. Our observations, on the red wing of this line (λ_0 + 12 nm), may be associated with a photospheric height, as indicated by the Contribution Functions computed for a quiet Sun model (Qu & Xu, 2002). This estimation is an approximation as the region we observe is deeply immersed in a non-quiet and non-homogeneous atmosphere.

4.1.2 Global properties of the pore and adjacent region

We present here results obtained by investigating the characteristics of AR10812, a pore divided into two parts by a light bridge. More in detail, the emerging intensity, and coupled temperature, and LoS velocity patterns of the observed pore and of the adjacent region let us investigate the radial structure of the pore and the convective regimes associated with different regions, inside and around the pore.

The radial mean structure is derived performing radial profiles, of intensity

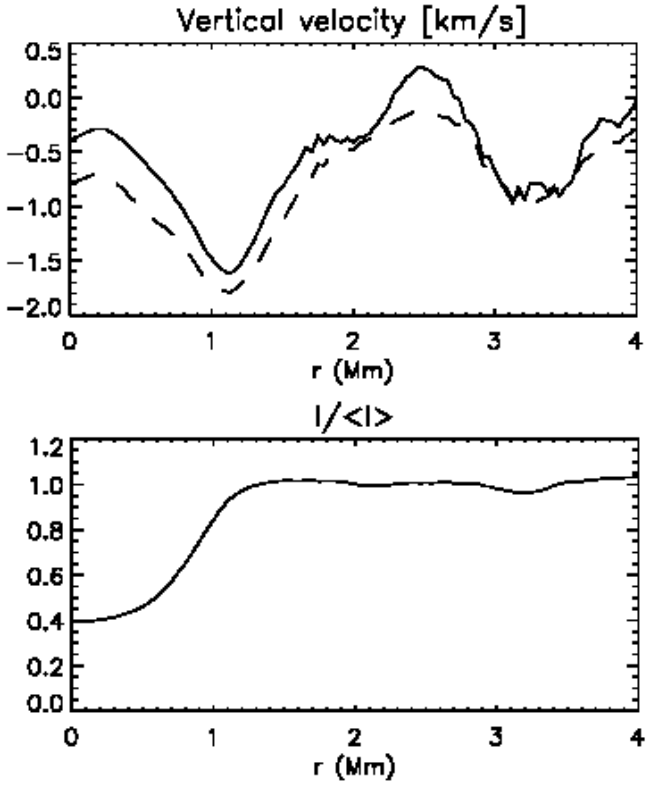

Figure 4.3: Azimuthally averaged profiles radially outward from the center of the pore. *Upper panel*: vertically emerging bolometric intensity, normalized to the corresponding average quiet-sun intensity; *lower panel*: LoS velocity (Cameron et al., 2007)

.

and velocity mean maps, starting from the pore geometrical barycenter and averaging them over the azimuth. The mean maps are computed averaging the 200 Fe I 709.0 nm LoS velocity and continuum intensity single maps obtained from the dataset. The light bridge region is masked and does not contribute to the mean radial profiles. Fig. 4.4 shows the velocity and intensity profiles of azimuthally averaged quantities.

The analysis of velocity and intensity mean radial profiles indicates the presence of three different regions. The first one is a quasi-plateau of about $200m \cdot s^{-1}$, compared to the quiet mean granular velocity set to zero, and it matches the pore umbra. The second region is characterized by a mean value of about $350m \cdot s^{-1}$ and rms fluctuations of $\simeq 100m \cdot s^{-1}$. It corresponds to the annular downflow nearby the pore. The third region is a large corona of quiet Sun granulation. The comparison of LoS velocity and intensity radial profiles shows that the position of the velocity minimum is beyond the pore boundary, as defined by the maximum of the intensity derivative, and just precedes the intensity plateau corresponding to the quiet granulation.

To proceed further in the analysis, we use this information to define the

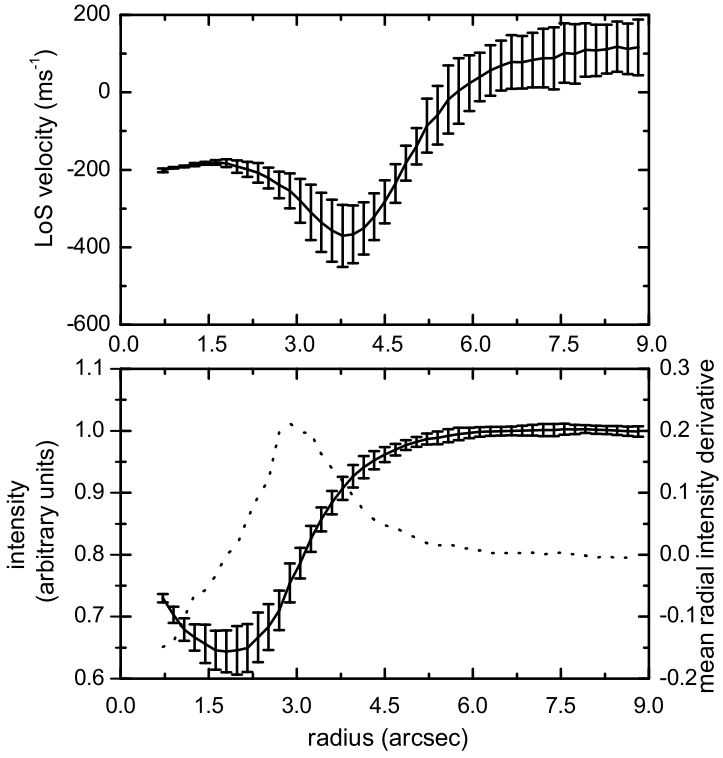

Figure 4.4: Plot of the mean LoS velocity (*upper panel*) and of the mean intensity (*lower panel*) against the distance from the pore center. Error bars for LoS velocity and for intensity have been computed as standard deviations from the mean. In the lower panel the derivative of the mean radial intensity (*dotted*) is also reported, whose maximum defines the pore umbra boundary.

three RoIs in the FoV. We define the umbra as the region included in a circle of 2.7" from the pore geometrical center (the inner circle of Fig. 4.5, *upper panel*), excluding the light bridge. We define the rim as the region surrounding the umbra up to 4.6" from the pore center (the region between the two circles in Fig. 4.5, *upper panel*). We take as reference a normal granulation region further away from the pore centre, from 6.1" to 8.2".

To perform a more thorough analysis of the rim region, we investigate it via the time-slice approach. For each LoS velocity map in the dataset, the annular rim region has been projected onto a cylindric coordinate system, centered in the pore geometrical center, so as to became rectangular. Then the average value in the ρ axis has been computed to obtain the mean value of the velocity for each θ direction at each instant. By indexing these vectors by increasing time, we obtain a LoS velocity time-slice of the rim region (Fig. 4.5, *lower panel*).

An ispection of the time slice reveals that the rim region has a negative mean value of the LoS velocity for the whole period spanned by the dataset, but it is

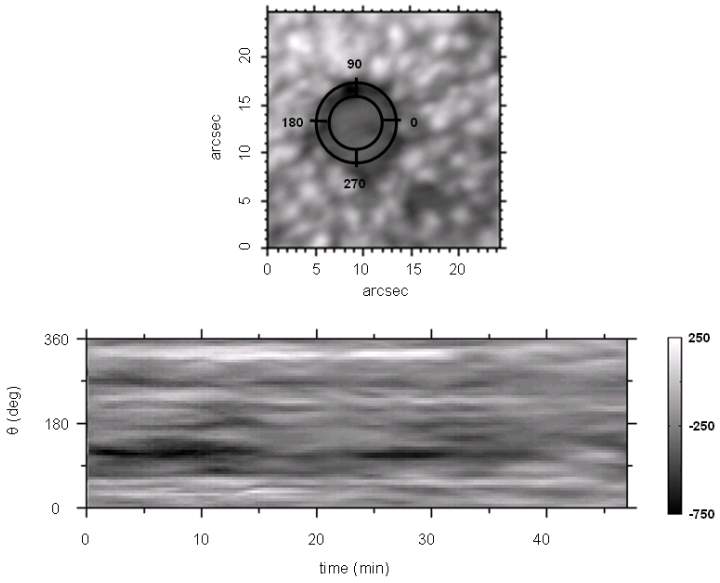

Figure 4.5: (*Top panel*): Doppler map of the analyzed pore region averaged over the whole dataset time span. The region inside the innermost circle is the umbra region, the region included between the two circles is the rim region (~ 2 arcses width). The ticks label the θ axis used in the projection for the time-slice diagram of the rim region. (*bottom panel*): time-slice diagram computed over the rim region.

irregular in space and intermittent in time. Also, a strong downflow plume (up to $1km \cdot s^{-1}$) is recurrent in the upper-left boundary of the pore.

Of particular interest is that simulated radial profiles of emergent intensity and vertical velocity of solar pores (Fig. 4.3), recently performed by means of the MURaM code (Cameron et al., 2007), are in excellent qualitative agreement with our experimental observations (Fig. 4.4). The azimuthally averaged profile of the vertical velocity resulting from this simulation shows a downflow of $1.5km \cdot s^{-1}$ at the photospheric level just outside the pore boundary. We remark that in this simulation MHD predicts that intense downflows, driven by the extra radiative cooling of the plasma surrounding magnetic elements and fed by upper layers horizontal flows, should encircle such magnetic elements.

In compressible convection calculations, the flow appears to be driven primarily by concentrated cold down-drafts, with more gently rising extended updrafts (Hurlburt et al., 1984; Stein & Nordlund, 1989, 1998; Spruit et al., 1990; Nordlund & Stein, 1997; Spruit, 1997; Steiner et al., 1998). Indeed, it is expected that cool temperatures around flux tubes, associated with suppressed convection, force plasma flows to develop downward plumes and, as a consequence, inflows at the visible surface (e.g., Hurlburt & Rucklidge, 2000). Converging and downward motions in sub-photospheric regions around magnetic structures are predicted by both monolithic and cluster models (cfr. 4.1) proposed to explain the formation of pores and sunspots. The cluster model needs down-

drafts and converging flows below the structure to hold together the flux tubes (Parker, 1979a). On the other hand, numerical experiments on monolithic flux tubes in a compressible convective atmosphere also show sub-photospheric motions of this type. Moreover, models computed by Deinzer et al. (1984), Knölker & Schüssler (1988) and Steiner et al. (1998) for small flux tubes (spatial scales near 200 km) and surrounding photosphere (out to about 2400 km) predict the presence of downward jets beyond the outer boundaries of the flux tubes with velocities nearly reaching the local sound speed. Many observational studies report annular regions of strong downflows around a pore (e.g., Keil et al., 1999; Sankarasubramanian & Rimmele, 2003) and the possible presence of supersonic speeds near the edge (Uitenbroek et al., 2006), confirming results of such numerical simulations. In particular Sankarasubramanian & Rimmele (2003) reported a $\sim 0.5''$ wide annular downflow structure around a pore, which accelerated from $200m \cdot s^{-1}$ at $\sim 500km$ above the photosphere to $1800m \cdot s^{-1}$ at $\sim 40km$.

More in detail, it is expected that such downflow channels surrounding the pores are not always closed rings, but their shapes are strongly changing in time. In particular, Hirzberger (2003), by analyzing highly resolved Doppler maps, found that the maximum velocities in the downflow channels occur on intergranular dark lanes around the pores, indicating a close relation between the dynamics of these downflow channels and convective flows around the pores.

In order to investigate the nature of convective regimes associated with the pore and its neighborhood we investigate the form of the probability distribution functions (PDFs) of the LoS velocity in the three regions, previously defined: i.e., the umbra ($\sim 7 \times 10^4$ measures), the rim ($\sim 10^5$ measures), and a surrounding annular region of granulation ($\sim 1.3 \times 10^5$ measures).

The PDFs are shown in Fig. 4.6. The velocity PDFs of the umbra and of quiet granulation regions are nearly Gaussian, while the PDF relative to the annular downflow region exhibits non-gaussian extended exponential tails. In particular, the nearly Gaussian PDFs come from regions where convection is present in a quasi-steady condition.

Actually, we observe:

1. a large and slightly asymmetric PDF, associated with the normal granulation, with mean velocity near zero and standard deviation $\simeq 170ms^{-1}$. As recognized, this kind of convective pattern is present in quiet Sun regions characterized by the presence of weak granular magnetic features. The PDF shows a positive skewness close to the downflows where the plumes are most vigorous. Indeed, asymmetry could be interpreted by a surface convection pictured in terms of upflows and downflows rather than as a hierarchy of eddies (Stein & Nordlund, 1998). In this picture upflows are warm and low density. Conversely, downward plasma fluid converges into filamentary plumes to conserve mass as it descends into higher density layers;

2. a tiny, all negative, and slightly asymmetric PDF, associated with the pore umbra. The retrieved mean value and standard deviation are around -200 ms^{-1} and 50 ms^{-1}, respectively. When the magnetic field inhibits the convective heat transfer in a sufficiently large volume, a pore is formed, and velocity fluctuations are reduced. However, the convective energy transfer cannot be totally suppressed and upflow plumes and umbral dots

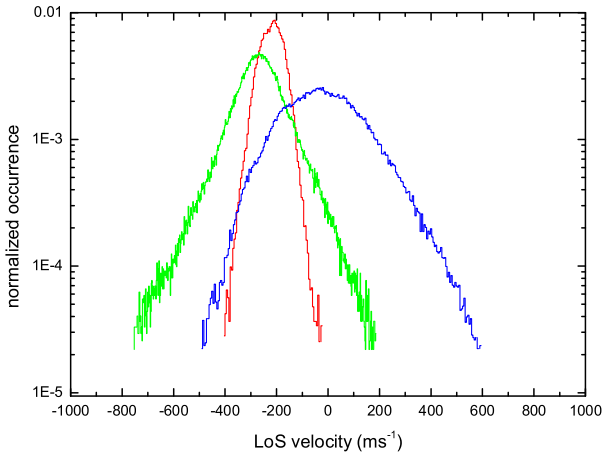

Figure 4.6: Probability distribution functions (PDFs) of the LoS velocity inside three different regions: the pore umbra (*red line*), the normal granular region surrounding the pore (*blue line*) and the intermediate annular region, the rim, (*green line*) shown in Fig. 4.5.

naturally emerge, as pointed out by magneto-convection numerical simulation with radiative transfer under strong field condition (Schüssler & Vögler, 2006). Indeed, the proposed narrow upflow plumes with nearby downflows, dominating the convective energy transport inside the pore, could explain the observed slight left-skewed distribution.

The broad non-gaussian PDF with extended exponential tails comes from velocities measured in the annular downflow region (see Fig. 4.5).

The computed mean value and standard deviation are around -270 ms^{-1} and 140 ms^{-1}, respectively.

Theoretically, a variety of explanations may be proposed to explain exponential tails in observed probability distributions. For instance, in experimental fluid systems, exponential tails could arise if the velocity fluctuations exhibit intermittent behavior in their magnitude on relevant spatial or temporal scales, as we observed in the annular downflow time-slice (Fig.4.5). Possibly, a non-Gaussian PDF shape may be read as evidence of the presence of several populations associated which different convective structures separated by structured magnetic field (see Fig. 1 in Cameron et al., 2007).

4.1.3 Fine structure and dynamics in a light bridge

Fig. 4.2 shows the pore region (AR10812) as observed in the G band, in the broad-band channel of IBIS and on the red wing of Ca II 854.2 nm line. The corresponding LoS velocity pattern, computed from Doppler shifts of the Fe I 709.0 nm line, is also displayed. The pore umbra appears separated into two parts by a light bridge. The most notable feature in all intensity maps shown in Fig. 4.2 is a dark lane running along the light bridge axis. In order to study in some

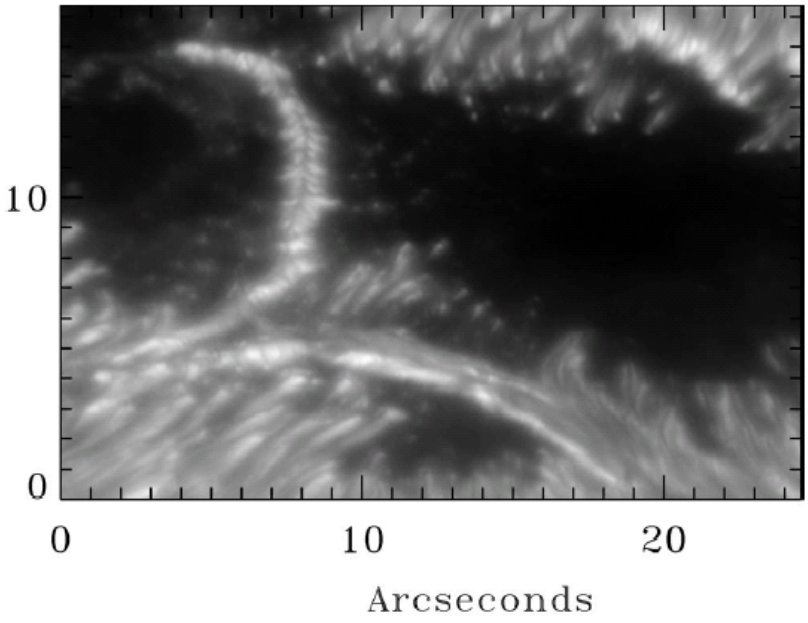

Figure 4.7: Blue continuum image (λ=487.7 $\pm$8 nm) of two light bridges within the largest umbra of NOAA 10036 near the solar limb taken with the Swedish 1-m Solar Telescope (SST) on La Palma, Canary Islands. The image is oriented such that the vertical direction is along a solar radius, with the closest limb towards the top. In this perspective view, the light bridge at the upper left shows a raised, segmented structure, while the bridge along the bottom shows little segmentation and extends well into the penumbra (Lites et al., 2004).

detail the structure of the light bridge, we performed several cuts through the light bridge in the direction of the arrow (see Fig. 4.2), roughly perpendicular to the dark lane. The cuts cover the whole light bridge and its immediate environment. In the last three panels (b, c and d) of Fig. 4.8 we show measurements of Ca II line wing, G band and broad band intensity along three representative slices cutting the light bridge. The profiles clearly indicate a decrease in intensity inside the light bridge, highlighting the presence of a dark structure.

An inhomogeneous and structured aspect seems to be a characteristic of many light bridges, which appear to be segmented along their length (Berger & Bierdyugyna, 2003; Lites et al., 2004). These segments are surrounded by very narrow dark lanes oriented roughly perpendicularly to the axis of the bridge, and also by a dark line, also very narrow, running parallel to the axis of the bridge and located approximately at its center. When viewed near the limb, the segmented light bridge appears as an elongated, tent-like structure, with the central dark lane being the high point of a ridge elevated above the dark background (Lites et al., 2004).

The presence of the dark lane inside the light bridge can be considered as related to an opacity effect (Schüssler & Vögler, 2006; Spruit & Scharmer,

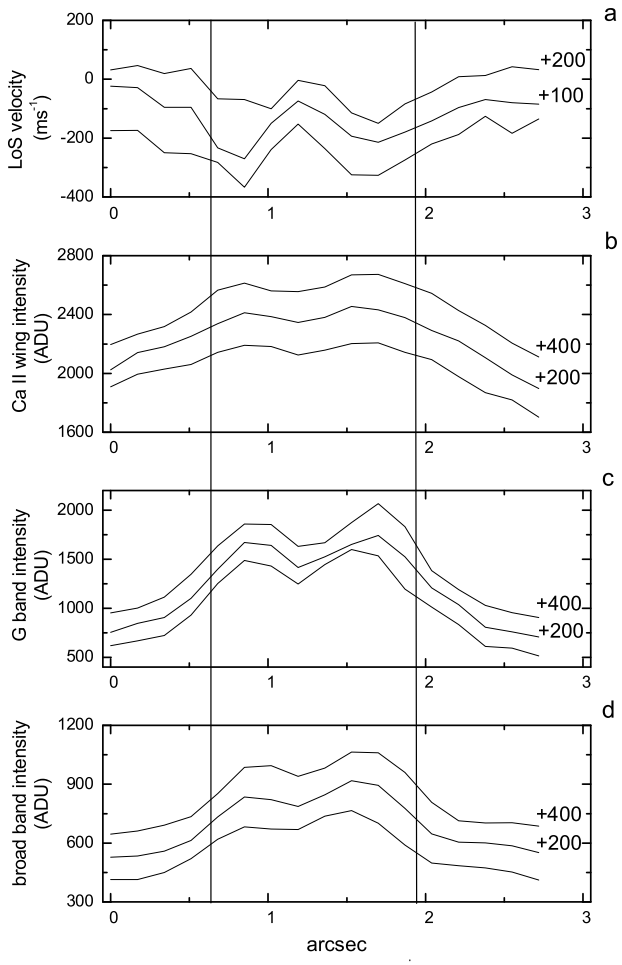

Figure 4.8: Plots of the light bridge intensity, in the red wing of the Ca II 854.2 nm line (b), in the G band channel (c) and in the broad-band channel of IBIS (d), and of the corresponding Fe I 709.0 nm line LoS velocity (a). All profiles have been computed across the light bridge and have been shifted vertically by arbitrary amounts to provide separation for the sake of visualization.

2006). In fact, as previously stated, light bridges are explained in terms of field-free, possibly convective, upflowing plasma which intrudes from below into an otherwise stable, magnetic structure Leka (1997). According to this picture, the magnetic field lines in light bridges take the form of a magnetic canopy (Leka, 1997; Jurĉák et al., 2006), above the field-free intrusion that appears with the umbra's separation. Above the forming bridge, the normally diverging field lines from the two umbrae fan out and up, until they are blocked by the field lines of their neighbor and forced to converge above this nonmagnetic intrusion, again in the vertical direction. The dark lane forms in the field-free part of the photosphere below the cusp of the magnetic field. The higher gas pressure in

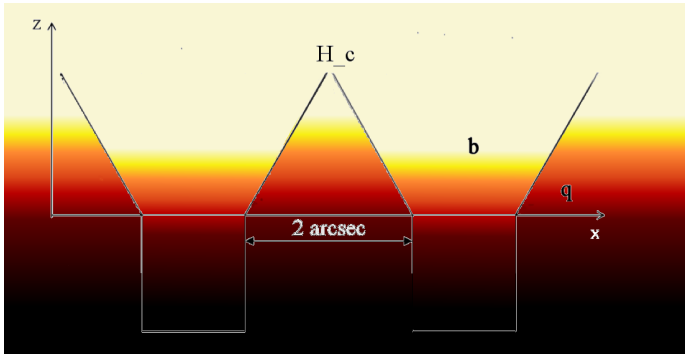

Figure 4.9: Cross-section of the light bridge structure modeled as a field free plasma region trapped by two magnetic flux tubes. Colors represent atmosphere density. For the sake of visualization z axis is not in scale with x axis. The two atmospheres are shifted by Z_w (the Wilson depression).

the region between the two magnetic tubes shifts the τ=1 surface to the higher layers of the atmosphere, which are comparatively cooler.

However, this segmented structure is not common to all light bridges. For example, the light bridges that extend into the penumbra do not have distinct grains or dark lanes but show features elongated along their length which resemble more the fine structure of the penumbra (Fig. 4.7).

An elongated feature inside the light bridge is observable also in our highest resolution velocity maps. Velocity measurements of the light bridge are reported in Fig. 4.8, in comparison with the ones relative to intensity. Such profiles show the occurrence of a kind of reversal in intensity and velocity of small scale features, i.e. intensity maxima along the light bridge match more intense downward velocities.

If we choose the darkest part of the umbra as a zero-point reference for the LOS velocity, accordingly to Bharti et al. (2007a) we measure a weak upflow, $\sim 50 \quad 100\ m \cdot s^{-1}$ along the LB axis, in correspondence of the intensity dark lane, and a downflow, around -150–200 m$\cdot s^{-1}$, along the LB boundary. Bharti et al. (2007a), observing a sunspot light bridge, report a strong downflow up to 500-1400 m$\cdot s^{-1}$ at the edge of the light bridge and an upflow around 100-200 m$\cdot s^{-1}$in the middle part of the LB.

The observed anti-correlation between photospheric intensity and LoS velocity recalls the *inverse granulation* phenomenon, which consists in the inversion of temperature fluctuations with respect to the velocity field. However, we observe dark intensity features in broad-band images, while the inverse granulation phenomenon involves intensities associated to upper photospheric regions. In fact, the occurrence of reversed granulation was observed around 120 km above the quiet Sun photosphere by Berrilli et al. (2002), in Fe I 537.9 nm and Fe I 557.6 nm photospheric line center images, around 140 km by Puschmann et al. (2003), using one-dimensional slit-spectrograms taken in quiet sun, and around 200 km by Janssen & Cauzzi (2006), using FeI 709.0 nm line center images.

As a consequence, we think that the anti-correlation between continuum intensity and photospheric velocities, reported here and in the paper of Bharti

et al. (2007a), both referring to LB features associated to an active region near the solar disk center, comes from a geometric effect due to the superimposition of the convective flow pattern with a field free region (i.e., with high opacity). This hypothesis could be easily verified via LB structures simulations or observations at different μ.

As a final remark, we note that the topology of the observed velocity structure along the light bridge resembles some specific types of roll patterns known from laboratory experiments on Rayleigh-Bénard convection and may be a signature of modified photospheric convective flows confined by two magnetic walls.

4.1.4 A light bridge structure interpretation

Radiative MHD simulations of light bridges by Nordlund & Stein (2007, unpublished) and Heinemann (2006) discussed in Heinemann et al. (2007) suggest how dark cores over the center of the light bridges are formed. They are found to be a consequence of hydrostatic pressure and radiative energy balance around the 'cusp' of the magnetic field, at the height in the atmosphere where field lines from both sides close over the gap.

Following the idea suggested by Nordlund and Heinemann to explain a dark lane present in a light bridge we propose an analytical model of the light bridge, in which we consider a field free model below a magnetic zone partially emptied of plasma.

The emergent intensity is calculated by considering the quiet and the magnetic contributions in the radiative transfer equation. An Eddigton grey model, with a source function ($S_q(\tau)$) linearly dependent on the optical depth (τ), is used for the quiet atmosphere:

$$S_q(\tau) = \frac{\sigma}{\pi}\frac{3}{4}T_e^4(\tau + 2/3) \tag{4.1}$$

where T_e is the effective temperature of the quiet Sun. We adopted for τ an exponential dependence on geometrical depth (z):

$$\tau(z) = e^{z/H_q} \tag{4.2}$$

where H_q is the scale height and is about 60 km.
A depressed model is used for the magnetized atmosphere, as suggested by **?**). In our model the optical depth ($\tau_m(z)$) is equal to:

$$\tau_b(z) = e^{(z \quad Z_w)/H_b} \tag{4.3}$$

Z_w is the so called "Wilson depression" and H_b is the scale height in the pore, which could be different from H_q. The relation between τ and τ_b is $\tau_b = w\tau^\beta$, where $\beta = H_q/H_b$ and $w = e^{\ z_w\beta/H_q}$. By setting the flux inside the pore equal to $\sigma {T_e^{(b)}}^4$, $T_e^{(b)}$ being the corresponding effective temperature of the pore atmosphere, we have:

$$S_b(\tau) = \frac{3\sigma}{4\pi}{T_e^b}^4(w\tau^\beta + 2/3) = \frac{3\sigma}{4\pi}{T_e^b}^4(\tau_b + 2/3) \tag{4.4}$$

In order to describe the separating surface between the quiet and the magnetic regions we use the expression $\bar{z}(x) = ax^\alpha + z_0$, where $a = H_c/x_0^\alpha$, H_c

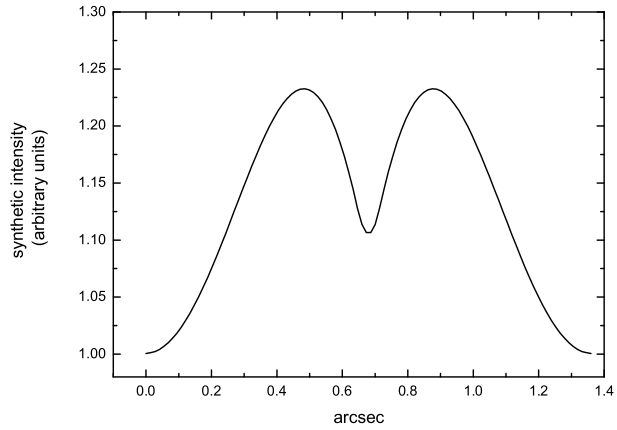

Figure 4.10: Synthetic emergent intensity across the light bridge computed by the model and convoluted with a Gaussian function of 0.3" σ, simulating an atmosphere seeing degradation comparable to that affecting our dataset.

being the cusp height and x_0 half of the bridge size. The atmosphere is described by the quiet model for $z < \bar{z}$ and by the magnetic model for $z > \bar{z}$. As a consequence, the intensity integral can be splitted into two terms:

$$I = \int_{\infty}^{\bar{z}} S_b(z)\chi_b(z)exp(\quad \tau_b(z))dz + \int_{\bar{z}}^{\infty} S_q(z)\chi_q(z)exp(\quad \tau(z))dz \qquad (4.5)$$

Moreover, by applying the variable change between z and τ, respectively for quiet and magnetic term, we obtain:

$$I = \int_0^{\tau_b(\bar{z})} S_b(\tau)exp(\quad \tau))d\tau + e^{(\tau(\bar{z}) \quad \tau_b(\bar{z}))} \int_{\tau(\bar{z})}^{\infty} S_q(\tau)exp(\quad \tau)d\tau \qquad (4.6)$$

which when solved gives

$$I(x) = T_e{}^{b4}\left[5/3 \quad e^{\ w\tau(\bar{z})^\beta}(5/3 + w\tau(\bar{z})^\beta)\right] + T_e^4(5/3 + \tau(\bar{z}))e^{\ w\tau(\bar{z})^\beta} \qquad (4.7)$$

The trend of the intensity as a function of x (i.e. along the bridge) depends on the value of w, β, $T_e^{(b)}$ and on the shape of $\bar{z}(x)$, which contains the information about the height of the magnetic field cusp and the size of the bridge. We choose a generic expression $\bar{z}(x) = dx^\alpha + z_0$, where $d = H_c/x_0^\alpha$, H_c being the cusp height and x_0 the half of the bridge size. In Fig. 4.10 we show the synthetic emergent intensity across the light bridge as computed by the model for a sensible choice of parameters: $\alpha = 2$, z_0=50 km H_c=220 km, x_0=500 km, β=1.6, $T_{eff}^{(b)} = 4350K$, $z_w = 150km$. With such a "combination" of parameters we can qualitatively reproduce the presence of a dark lane across the light bridge.

4.1.5 Temporal evolution

Observations (e.g., Wang & Zirin, 1992; Keil et al., 1999) reveal that sunspots and pores result from the merging of small magnetic elements, driven by super-

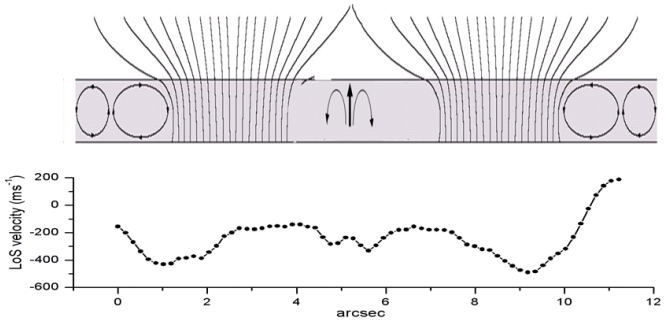

Figure 4.11: (*Top panel*): schematic cross-section of the analyzed structure. In the background a sketch of the flows around the pore: the model is obtained by considering two magnetic flux tubes, each derived from the simulation by Hurlburt & Rucklidge (2000). (*Bottom panel*): computed mean LoS velocity, averaged along the whole length of the light bridge (dot+spline).

granular and subsurface flows. Small flux elements coalesce forming small pores and spots. After the pore has formed, it can develop into a sunspot forming a penumbra if the magnetic flux increases, and the field becomes more inclined at the edge of the pore. The magnetic configuration becomes unstable, and the interaction of the strongly inclined field with the surrounding convective motions can cause the formation of a penumbra. The possible evolution of pores into sunspots depends on a dynamic stability criterion (Bray & Loughhead, 1964; Wang & Zirin, 1992; Rucklidge et al., 1995). According to the model of Rucklidge et al. (1995), if pore and sunspot sizes are tracked against their magnetic flux there is hysteresis for the formation of a penumbra. As the magnetic flux within a pore increases, its radius increases without necessarily forming a penumbra until a critical flux and radius is exceeded. However, once a minimum flux is exceeded (which is less than the critical flux) the pore is unstable and outside perturbations can cause the rapid formation a penumbra. Thus, this model accounts for the overlap in sizes between small sunspots and larger pores.

Our dataset refers to a single day of observations. The previous history of the pore, classified as AR10812, is derived from MDI/SOHO magnetograms (Fig. 4.13) and continuum images (Fig. 4.14). By analyzing MDI images, corresponding to three days before our observation run, we established that the pore was made up of two different structures, showing the same polarity.

By considering the evolution of the analyzed region and taking into account a simulation by Hurlburt & Rucklidge (2000), we propose a sketch of the whole structure of the observed pore (Fig. 4.11). We hypothize the pore has been originated by the merging of two separate magnetic structures with the same polarity both surrounded by downward flows. These downflow structures persist in the quenching region (corresponding to the light bridge), where the convection results strongly modified by the presence of the magnetic field, and also in the annular region surrounding the pore. This scheme is analogous to that reported by Jurĉák et al. (2006) to explain the magnetic canopy above light bridges.

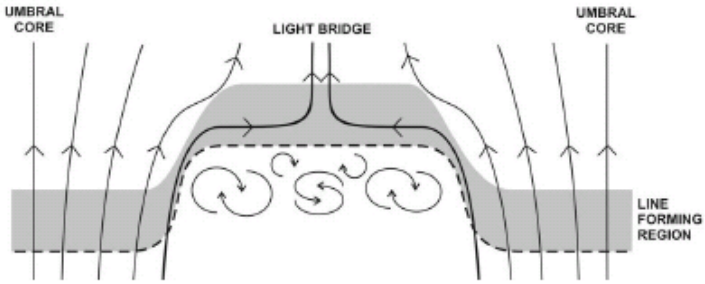

Figure 4.12: Schematic view of the magnetic canopy above LB (Jurĉák et al., 2006).

This interpretation is supported by the observed mean LoS velocity structure reported in Fig. 4.11. This LoS velocity profile is obtained by averaging profiles computed along twelve slices orthogonal to the light bridge and crosswise to the pore.

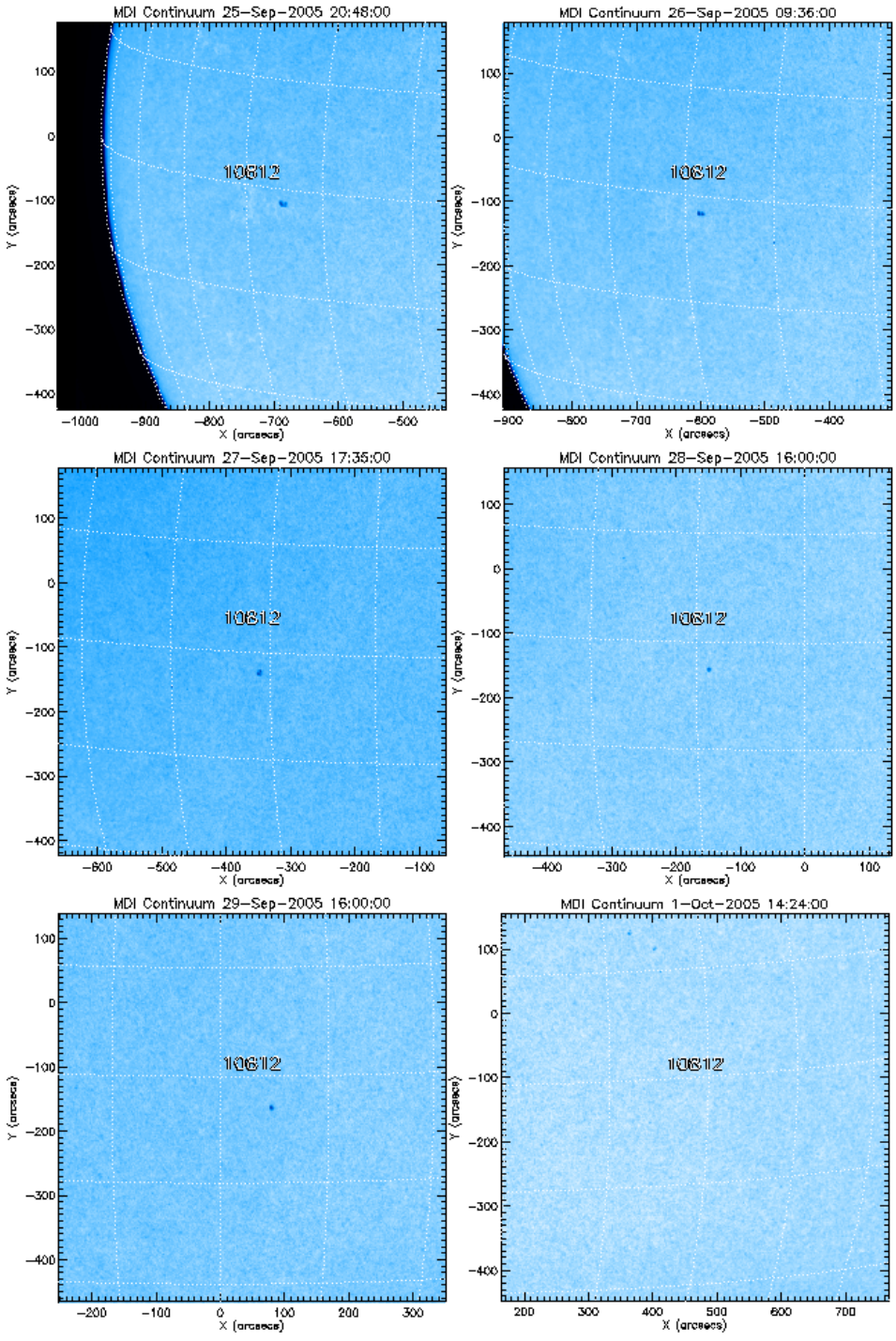

Figure 4.13: MDI-SOHO continuum images of the AR10812 region.

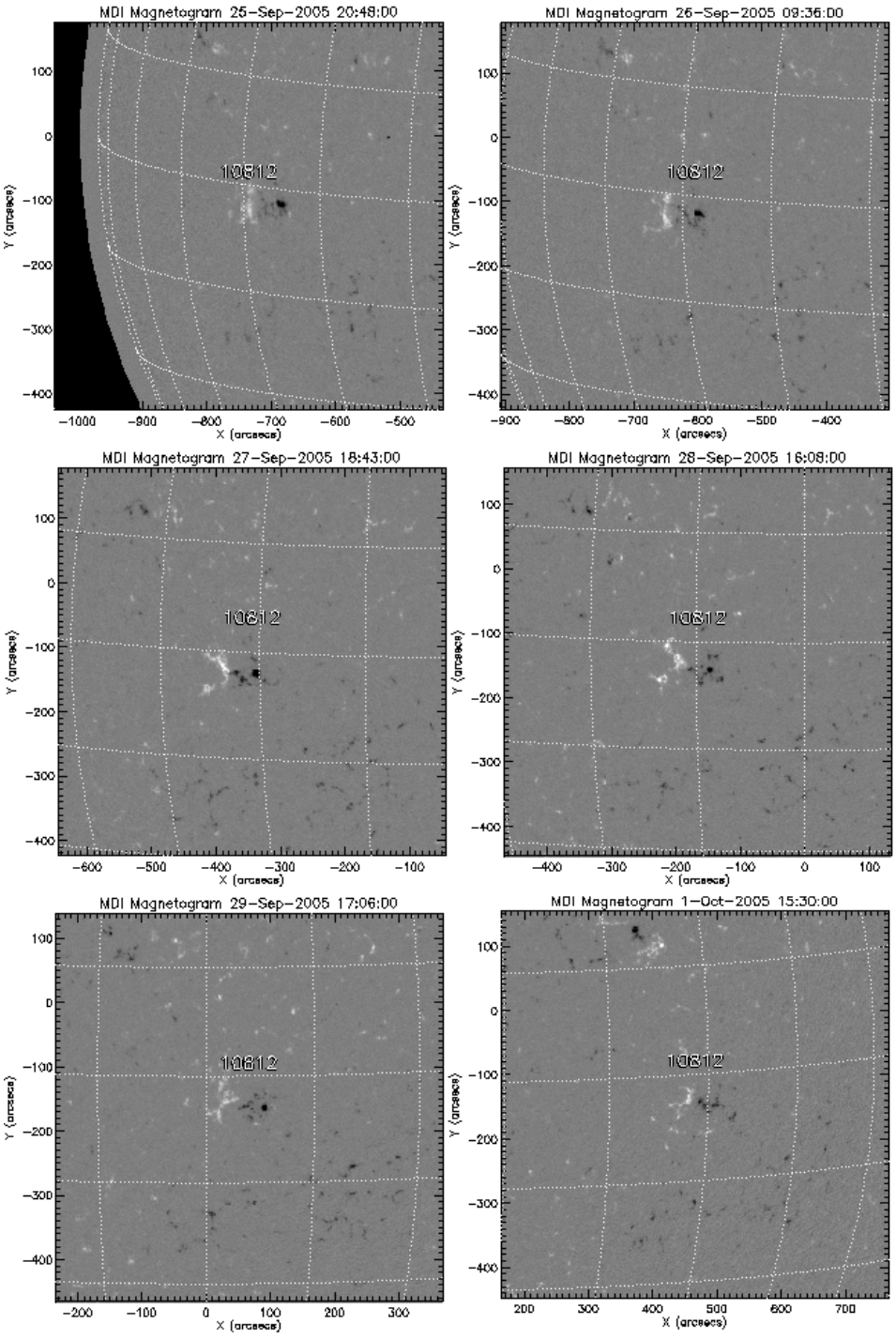

Figure 4.14: MDI-SOHO magnetograms of the AR10812 region.

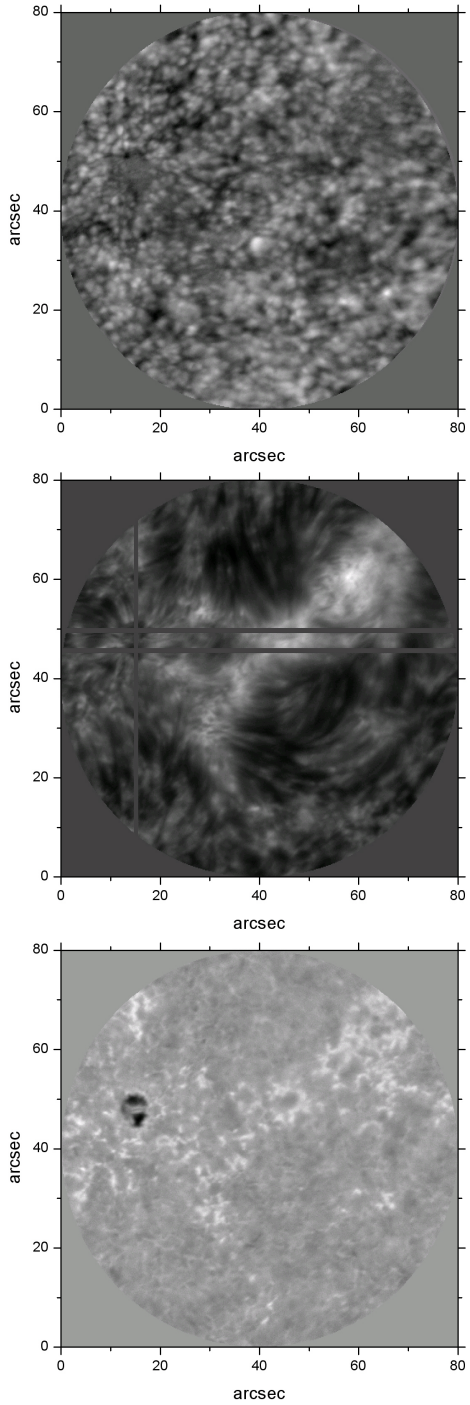

Figure 4.15: An example of an IBIS dataset. *Top panel*: Doppler velocity field extracted from Fe I 709.0 nm line scan. *Central panel*: Ca II 854.2 line core intensity image. *Bottom panel*: Ca II 854.2 line wing intensity image. The grey horizontal and vertical slices, drawn in the central panel figure, denote the regions we analyzed in the space-time diagrams plotted in Fig. 4.16 and Fig. 4.17, respectively.

4.2 Solar atmospheric oscillations in a region with a pore

It has been shown with linear adiabatic perturbation theory that small-amplitude oscillations of the solar body about its equilibrium state can be classified into three types: pressure modes (p-modes), where the pressure is the dominant restoring force; gravity-modes (g-modes), where gravity or buoyancy is the dominant restoring force; and a class of surface or interface modes (f-modes), which are nearly compressionless surface waves. The p-modes are essentially standing acoustic waves; in solar models they have cyclic frequencies between 250 and 5000 Hz. The g-modes are standing internal gravity waves with estimated frequencies below the 450 μHz. In the Sun the only modes that have been definitely observed are the so-called 5-minutes oscillations, with frequencies between 1500 and 5000 μHz; these correspond to p-modes or, at high degree, also f-modes.

The properties of acoustic waves propagating in a magnetized solar atmosphere have received considerable attention. The solar stratified atmosphere operates like a high pass in electronics: it lets only high frequency sound waves, with frequency above the acoustic cutoff frequency ($\nu > \nu_{ac}$), propagate in the upper layers without restrictions. As shown in Appendix A, the acoustic cutoff frequency ranges from $\omega_{ac} \simeq 4 \times 10^{-3}\ s^{-1}$ (corresponding to a period of ~ 25 min) in the solar interior to $\omega_{ac} \simeq 3.5 \times 10^{-2}\ s^{-1}$ (corresponding to a period of ~ 3 min) $\simeq 500$ above the photosphere. Waves of frequencies less than the photospheric ω_{ac} bounce back into the solar interior.

The presence of magnetic fields influences the propagation of waves through the solar atmosphere. In particular, as reported in Appendix A, in presence of a vertical magnetic field sound waves propagate along field lines. On the other hand, the presence of an inclined field reduces the acoustic cutoff frequency by a factor $cos\theta$. As a consequence, the acoustic waves can tunnel through a significantly smaller evanescence region before propagating once again in the upper layers.

The study of the generation and propagation of such waves in the solar atmosphere is an important subject of astrophysical research, since it provides information about the atmospheric structure and dynamics (e.g., Lites, 1992; Bogdan, 2000; Socas-Navarro et al., 2000; Bogdan & Judge, 2006), while at the same time it helps us to identify the key mechanisms of chromospheric and coronal heating.

The solar chromosphere is arguably the least understood region of the solar atmosphere. Studying its heating is one of the principal research areas of solar physics. A temperature minimum at ~ 500 km above the photosphere, and the subsequent reversal of the temperature profile, suggests the presence of some unknown heating mechanism to balance the energy lost by radiation. Identifying such mechanism is a complex problem, since the predominant mechanical processes are probably of a non-linear hydrodynamical and magnetic nature. Furthermore, the atmosphere is strongly stratified and is threaded by magnetic fields. Thermal and radiative conditions therefore deviate drastically from local thermodynamic equilibrium and the magnetic fields, expanding with height, can greatly complicate chromospheric dynamics.

A number of heating processes have been proposed, among them the magnetic field reconnection (Parker, 1988), the resistive dissipation of electric cur-

rents (Rabin & Moore, 1984) and the mechanical heating via the dissipation of energy carried by waves.

By adopting the IBIS dateset, described in the previous section, we investigated the oscillatory properties of the quiet and active solar chromosphere in relation to the underlying phtotosphere. Fig. 4.15 shows a typical LoS velocity map, computed from Doppler shifts of the photospheric Fe I 709.0 nm line, and the corresponding image acquired in the core of the chromospheric Ca II 854.2 nm line. In Fig. 4.15 we also show the same FoV observed in the red wing of the Ca II 854.2 nm line, which is often used as a proxy of the magnetic field. Bright features on this image can be associated with photospheric magnetic fields.

We can differentiate between different magnetic domains within the FoV. The dark structure is the pore, with a well recognizable light bridge. The bright structures around the spot and further away from the AR are the bright chromospheric network. It is made up of an assembly of small-scale magnetic elements. The dark regions correspond to the internetwork cells, which are considered essentially as magnetic field-free regions.

Therefore, our dataset allows us to study the photospheric and chromospheric dynamics of different solar structures: a solar pore with a light bridge, a network region and an internetwork region.

4.2.1 Sunspot and pore oscillations

For more than 30 years oscillatory motions have been observed in pores and sunspots, identifiable both as intensity and velocity variations in photospheric and chromospheric lines. The existence of the chromospheric umbral oscillations was first reported by Beckers & Tallant (1969). In 1972 the umbral oscillation both in the photosphere and in the chromosphere was the main subject in many papers (Bhatnagar & Tanaka , 1972; Giovanelli, 1972; Bhatnagar et al., 1972; Beckers & Schultz, 1972). Historically, sunspot oscillations are classified as falling into one of three categories (e.g., Thomas, 1985; Lites, 1992; Bogdan, 2000): 5-min umbral-photospheric oscillations, 3-min umbral-chromospheric oscillations and running penumbral waves. The separation is unfortunate because all these oscillations are manifestations of global coherent oscillations of the entire sunspot.

The 5 minute band oscillations have periods between 200 and 400 s, with a dominant peak around 5 minutes. They are observed in sunspots and pores with nearly the same spectra as in the quiet Sun (Beckers & Schultz, 1972; Penn & Labonte, 1993; Bogdan, 2000; Staude, 1999). They are coherent over a significant fraction of the umbra and in sunspots they extend into portions of the neighboring penumbra. Peaks in the power spectrum are probably due to the interference of many modes, similar to the quiet Sun. They are readily detected in lines which form low in the photosphere. In the chromosphere either they have low amplitudes or they are not present at all. Such oscillations were first detected in the photosphere by Beckers & Schultz (1972) who suspected a strong possibility of contamination of the velocity signal by the 5 minute oscillations in the surrounding quiet photosphere. Subsequent observations firmly established the presence of 5 minute oscillations in sunspot and pore umbrae through the use of telluric spectral lines as a wavelength reference and the use of either purely umbral spectral lines (Bhatnagar et al., 1972; Rice & Gaizauskas, 1973; Soltau

et al., 1976; Livingston & Mahaffey, 1981) or the Stokes V-profile (Thomas et al., 1982, 1984) of a magnetic line to measure velocities in order to minimize the contribution of scattered light from the surrounding photosphere.

Such oscillations represent the response of the magnetic flux tube to forcing by the 5-minute p-mode oscillations in the surrounding convection zone (Thomas, 1981; Thomas et al., 1982).

The 3 minute band oscillations have period between 100 and 200 s and they have been observed in the photosphere, chromosphere and transition region above the umbra with a dominant peak at 3 minutes (5.5 mHz). They are easily observed in the chromosphere, where their amplitude is large. On the contrary, in the photosphere they are observed with difficulty and are not even detectable because of their lower amplitude. The 3 minute oscillations are coherent on smaller spatial scales than their 5-min counterparts. Such type of oscillations consist of resonant modes of oscillation of the umbra itself. The nature of chromospheric oscillations in pore and sunspot umbra has been the subject of discussion from the moment of their discovery until the present day. Two different theoretical models have been proposed to explain them. One model introduces a resonant cavity consisting of fast magneto-atmospheric waves that are nearly trapped in the photosphere and subphotosphere. The wave modes can be excited either by overstable convection in the umbral subphotosphere or by filtering of high-frequency components of the 5-minute p-mode oscillations in the surrounding convection zone (Uchida & Sakurai, 1975; Scheuer & Thomas, 1981; Thomas & Scheuer, 1982). The other model attributes these oscillations to a resonant mode of slow magnetoacoustic waves that are nearly trapped in the chromosphere and especially between the temperature minimum and the transition region. The oscillations can be excited by non-linear coupling with the photospheric modes or by acoustic waves from the convection zone at these frequencies (Zhugzhda et al., 1983, 1984; Gurman & Leibacher, 1984)).

Running penumbral waves (RPWs) represent the dominant oscillatory phenomenon in the sunspot penumbra. They were first observed in H_α by Zirin & Stein (1972) and indipendently by Giovanelli (1972, 1974). Their name is due to their characteristic behaviour of expanding radially outward, from the inner to the outer edges of the penumbra. They show up as alternating dark and bright bands in velocity images, starting out as arcs surrounding the umbra with azimuthal extents of 90°-180° and sometimes even 360°. They have periods of 180-300 s and propagate more or less uniformly outwards, with a steady decrease in the apparent radial propagation speed. Some authors found that RPWs originate from elements that oscillate inside the umbra and propagate through the penumbra.

In order to study the oscillation properties of a solar pore with a light bridge we utilized the data acquired on September 28, 2005 largely described in §4.1.1. We focused our analysis on data acquired in the mid-photospheric Fe I 709.0 nm line and in the low-chromospheric Ca II 854.2 nm core line. The formation height for the average Fe I 709.0 nm line is $\sim 100km$. The Ca II 854.2 nm line forms at $\sim$ 800 km above the photosphere. According to the Contribution Functions computed for a quiet Sun model (Qu & Xu, 2002), our images, acquired in the center of the Ca II 854.2 nm line, refer to a height of $\sim$ 1300 km.

The most common tool used in observational studies of oscillatory properties is the Fast Fourier Transform. Standard Fourier analysis was applied to the

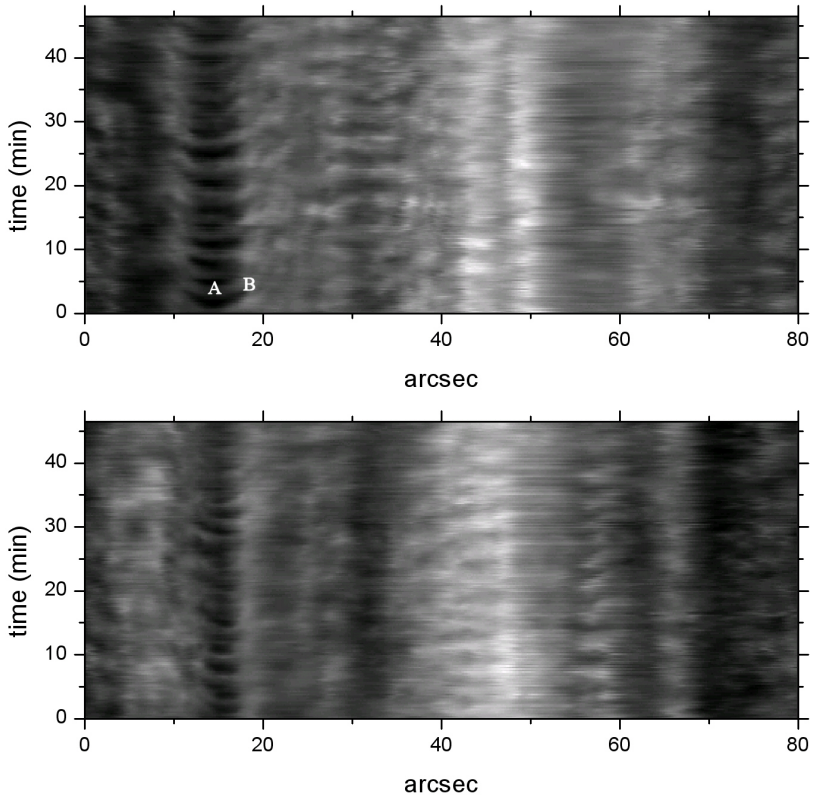

Figure 4.16: Space-time diagrams of Ca II 854.2 nm line core intensity signal. They are obtained by following in time the line core intensity signal along two horizontal slices crossing the pore (see Fig. 4.15). The vertical dark lines mark the umbra boundaries.

temporal series of photospheric line-of-sight velocities and of chromospheric line core intensities. Other analysis techniques might be more applicable to the study of the spatio-temporal dynamics, but Fourier analysis provides an initial insight into the chromospheric behaviour. Before applying the Fourier analysis to our time series, we displayed the sequence of images as a movie in order to get an idea of the dynamics. The pore shows a clear oscillatory behaviour, with a signature of radially outward waves. Such behaviour is evident in the space-time diagrams shown in Fig. 4.16 and Fig. 4.17, in which the x-axis corresponds to the space and the y-axis to the time. They are obtained by following in time ($\sim$ 45 minutes) the Ca II 854.2 nm line core intensity along horizontal (Fig. 4.16) and vertical (Fig. 4.17) slices, of 6 pixel width, crossing the pore (see Fig. 4.15). More in detail, the two-dimensional time-slice diagrams are obtained by assembling the "one-dimensional" slice images taken in successive instants; we contract these slices to one pixel width by averaging over the 6 pixels.

In all these diagrams the pore is clearly distinguishable from other solar regions: the dominant period of oscillations is around 3 minutes. As previously stated, three-minute oscillations are commonly observed in the chromosphere umbra of sunspots and pores. This result is confirmed by the mean power

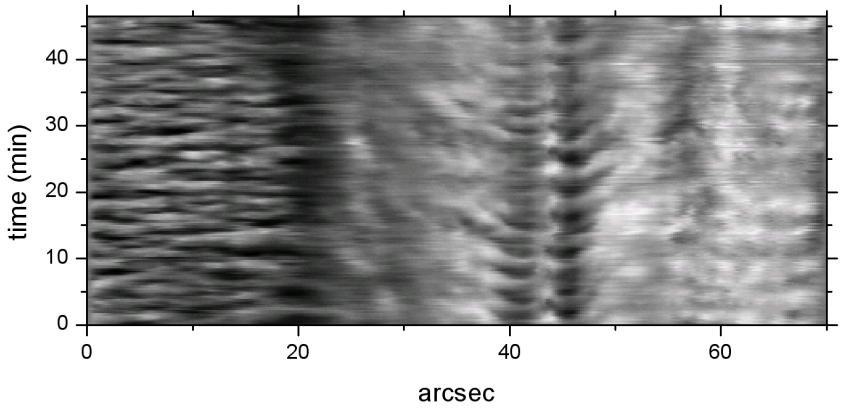

Figure 4.17: Space-time diagram of Ca II 854.2 nm line core intensity signal. It is obtained by following in time the line core intensity signal along the vertical slice crossing the pore (see Fig. 4.15).

spectrum (Fig. 4.18) calculated for the chromospheric intensity signals. It is obtained by averaging the power spectra computed for all pixels belonging to the pore, excluding the light bridge contribution. In Fig. 4.18 we also report the mean power spectrum calculated for the photospheric velocity signal. It shows a peak around 3.3 mHz, due to the 5-minute oscillations, while in the chromosphere the power spectrum exhibits one main peak around 6 mHz and a secondary peak around 4.5 mHz. Note that there is nearly no power at all in the 5 minute band (3.3 mHz). The chromospheric spatially averaged power spectrum depends on the portion of the pore umbra we select. If we consider a larger umbral region we obtain an averaged power spectrum different in shape, but with peaks always in the 3 minute range. Several authors found that the shape of the power spectrum differs from one point to another inside the umbra.

In order to investigate the spatial distribution of the oscillating frequencies we computed maps of frequency of maximum spectral power. These maps are obtained by calculating the power spectrum, pixel by pixel, and selecting the maximum power frequency, corresponding to the most representative oscillating frequency for the selected pixel. In Fig. 4.20 we report photospheric and chromospheric maximum power frequency maps. The photospheric maximum power frequency map shows that the dominant oscillation period in the photospheric layer is around 5 minutes, independently from the quiet or active solar region. On the other hand, the maximum power frequency map relative to the chromosphere confirms that the distribution of power varies inside the pore umbra, in which there are points oscillating with different frequencies, in the range between 4 mHz and 6 mHz (3 minute band).

An important property emerging from the chromospheric maximum power frequency map is the dominance of oscillations in the 5 minute band in the regions surrounding the pore and in the light bridge. As previously stated, the presence of an inclined magnetic field reduces the acoustic cutoff frequency allowing waves otherwise evanescent to propagate. Thus, in the center of the

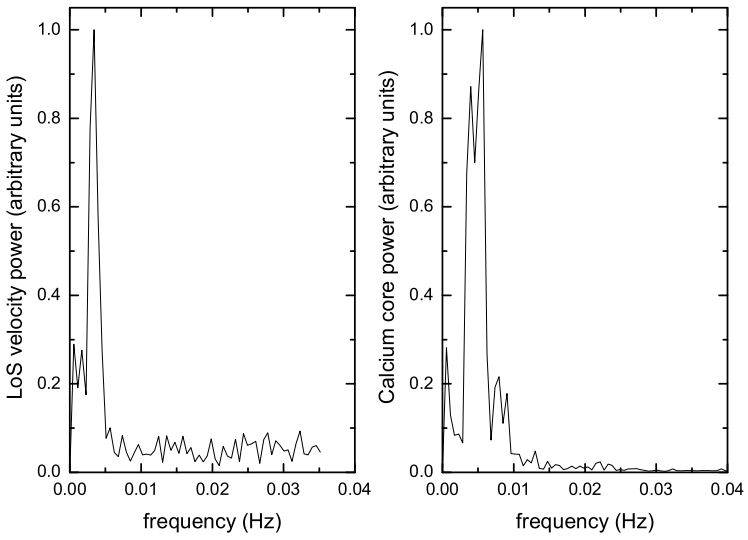

Figure 4.18: Power spectra of the photospheric LoS velocity signal (*left panel*) and chromospheric line core intensity signal (*right panel*) averaged over the entire pore umbra.

pore, where the magnetic field lines are found to be roughly vertical, sound waves with frequency above the acoustic cutoff frequency propagate along the field lines, unaware of the presence of the magnetic field. At pore boundaries, where generally magnetic field lines are inclined by about 40°-80°, the acoustic cutoff frequency end up being reduced and waves with frequency below the acoustic cutoff frequency can propagate.

We compared the "maximum power frequency" maps with power maps computed in selected frequency regions in order to verify that the indicated maximum power frequencies represent the most characteristic oscillating frequencies for the corresponding pixels. In Fig. 4.21 we report two chromospheric power maps obtained by averaging the power spectra over two selected temporal frequency bands: 2.8-3.9 mHz (the "evanescent" range) and 5.5-8.4 mHz (the "high frequency" range). Each image is linearly scaled, the brighter the region, the higher the power, black means that there is no power.

By comparing these two maps it results that inside the light bridge the power is all concentrated in the 5 minute band, in which it appears brighter than the surrounding umbra. The pore appears dark in both power maps, which means that there is no significant power inside it. This effect is related to the low count-rate inside the pore and it is removed if we consider the power spectrum averaged over the entire pore area, as just shown in Fig. 4.18. We do not report the same maps calculated for the photospheric intensity signal, in which all power is concentrated in the 5 minute band.

All spatio-temporal distributions of the Ca II 854.2 nm line core intensity, shown in Fig. 4.16 and Fig. 4.17, show a clear structure resembling a "chevron"

in correspondence of the pore umbra. While three minute oscillations are a common phenomenon in the chromosphere umbra of most pores and sunspots, clearly distinct "chevron" structures do not appear so frequently. The position of the "chevron" along the time axis implies the presence of propagating wave motions in the umbra chromosphere. In our case the spatial size of the "chevron" corresponds to the umbra size. From observations of sunspots (e.g. Kobanov et al., 2006), the chevron size slightly exceeds the umbral one; outside the inner boundary of the penumbra the oscillation power drops sharply. The fact that the three-minute "chevron" scale is restricted by the umbral size does not support the common idea of a direct connection between the three minute oscillations and running penumbral waves (RPW). From the slope of the chevron we can calculate the velocity of wave propagation. The temporal distribution of the Ca II 854.2 nm line core intensity for the points A and B (see Fig. 4.15) are plotted in Fig. 4.19. The calcium line core intensity signal at the point B is characterized by the mean time delay of 42 s with respect to the intensity signal at the point A. Since the distance between these points is 2.5", the phase velocity was slightly less than 20 $km \cdot s^{-1}$.

4.2.2 Network and inter-network dynamics

It has long been thought that the cutoff frequency for magnetoacoustic gravity (MAG) waves, in general, depends on the local plasma β (the ratio of gas to magnetic pressure) and the inclination of the magnetic field lines. Bel & Leroy (1977), by using an isothermal solar atmosphere model, predicted that in regions of weak magnetic field ($\beta >> 1$) the cutoff frequency should not be dependent on the magnetic field and should have the value 5.2 mHz. On the other hand, in highly magnetized regions ($\beta << 1$) the effective gravity on a particular magnetic field line would be modified by the cosine of the angle ($cos\theta$) subtended by that field line with respect to the direction of gravity. As a consequence, the cutoff frequency $\nu_a c$ should have a value reduced by the same quantity with respect to the theoretical quiet-Sun value. The Bel & Leroy model has been improved by a number of researchers (Zhugzhda & Dzhalilov, 1984a,b,c; Schwartz & Bel, 1984; Schwartz, et al.; Zhugzhda et al., 1984), who studied the propagation of MAG waves in similar regions with arbitrarily inclined magnetic fields and more realistic atmospheric models.

On the basis of these considerations one would not be able to observe any signature of low-frequency ($\nu < \nu_{ac}$) traveling waves in regions typically referred to as the "quiet Sun". The quiet Sun, in the chromosphere, is bifurcated into the magnetic network, which identifies the boundary of supergranulation cell, and the largely field-free inter-network medium in the cell interior. Proper motions in the supergranular cell (inter-network) push the magnetic flux to concentrate along the boundary (network). Thus the magnetic flux is stronger there, which is thought to be the physical reason why the network structure shows a greater emission than the inter-network at the top of the solar atmosphere.

By analyzing the chromospheric quiet-Sun wave spectrum we can identify an upward propagating component at low frequencies which carries a larger energy flux than its high-frequency ($\nu > \nu_{ac}$) counterpart which is normally associated with wave heating of the solar atmosphere. In fact, quiet Sun network and internetwork are characterized by different wave frequencies: the network is dominated by oscillations with periods of 5 minutes while the internetwork

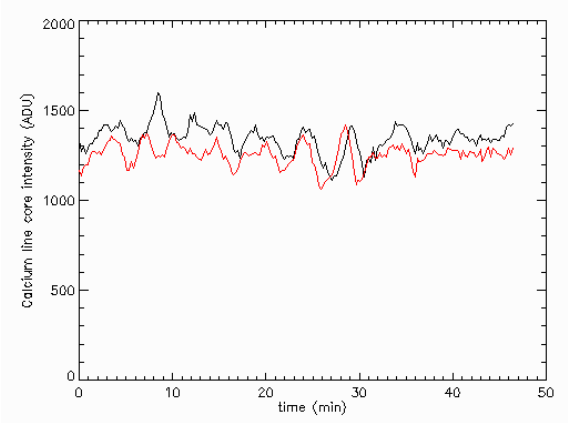

Figure 4.19: The time delay between calcium line core intensity signals measured at the points A (*red line*) and B (*black line*).

shows a concentration of power in the 3 minutes range.

By analyzing the above described IBIS dataset, we investigated the oscillatory properties of network and internetwork regions. The frequency maps of maximum spectral power, reported in Fig. 4.20, confirm the different dynamical properties of network and internetwork. In the internetwork the dominant wave period is around 3 minutes. On the other hand, the network is dominated by oscillations with periods of 5 minutes and longer. These results are also evident in the CaII chromosheric power maps shown in Fig. 4.21, relative to two different frequency ranges. At frequencies below the acoustic cutoff, significant chromospheric power is found within and immediately around the magnetic network. The power map obtained for frequencies above the acoustic cutoff shows a concentration of power in the internetwork regions.

The high frequency internetwork oscillations have been successfully explained by acoustic waves that travel into the chromosphere and form shocks in the higher layers (Carlsson & Stein, 1997). On the other hand, the nature of the network oscillations is still not known, although the fact that the network consists of small-scale strong-field magnetic elements hints with a connection to these flux tubes.

Recent numerical simulations have shown the appearance of 5 minute waves in coronal loops near strong active regions (De Pontieu et al. 2005, De Moortel et al. 2002) and in chromospheric spicules (De Pontieu et al., 2004) as a result of the angular dependence of ν_{ac} on the inclination of the magnetic field. The spicule phenomenon is considered related to the leakage of p-mode oscillations into the chromosphere and to the nonlinear evolution of photospheric flows and tunneled oscillations into the inhomogeneous solar atmosphere. While all these analysis have mostly been based on analysis of active regions, one might expect to observe the leakage of low-frequency waves ($\nu < \nu_{ac}$) also at the boundaries of convective cells, where the field lines are substantially inclined. Indeed, Jefferies et al. (2006) show that quiet magnetic network elements provide "portals" through which low-frequency magneto-acoustic waves can propagate into the solar chromosphere. Such waves contribute to heat the ambient solar

chromosphere more than high frequency acoustic waves. Such results have been recently confirmed by Vecchio et al. (2007) who show that a large fraction of the chromospheric acoustic power at frequencies below the acoustic cutoff, residing in the proximity of the magnetic network elements, directly propagates from the underlying photosphere.

The power map relative to the high frequency regime shows another interesting feature: in regions surrounding the pore and the network, the 3-min power is considerably lower than in the internetwork away from the AR. The lack of power in these regions, called "magnetic shadows", has been explained in terms of the interaction between the acoustic waves (the global p-modes) traveling upward, and the expanding magnetic field of the pore and of the network elements. As the flux tubes expand with height, their field lines get more and more inclined until they either become horizontal or encounter field lines from other flux tubes. Thus they form the so-called magnetic canopy. From theoretical studies it results that the interaction of the acoustic waves with the overlying magnetic field can cause either a reflection of the waves or a mode conversion. If this interaction occurs below the observed height, then in both cases we would get less acoustic power.

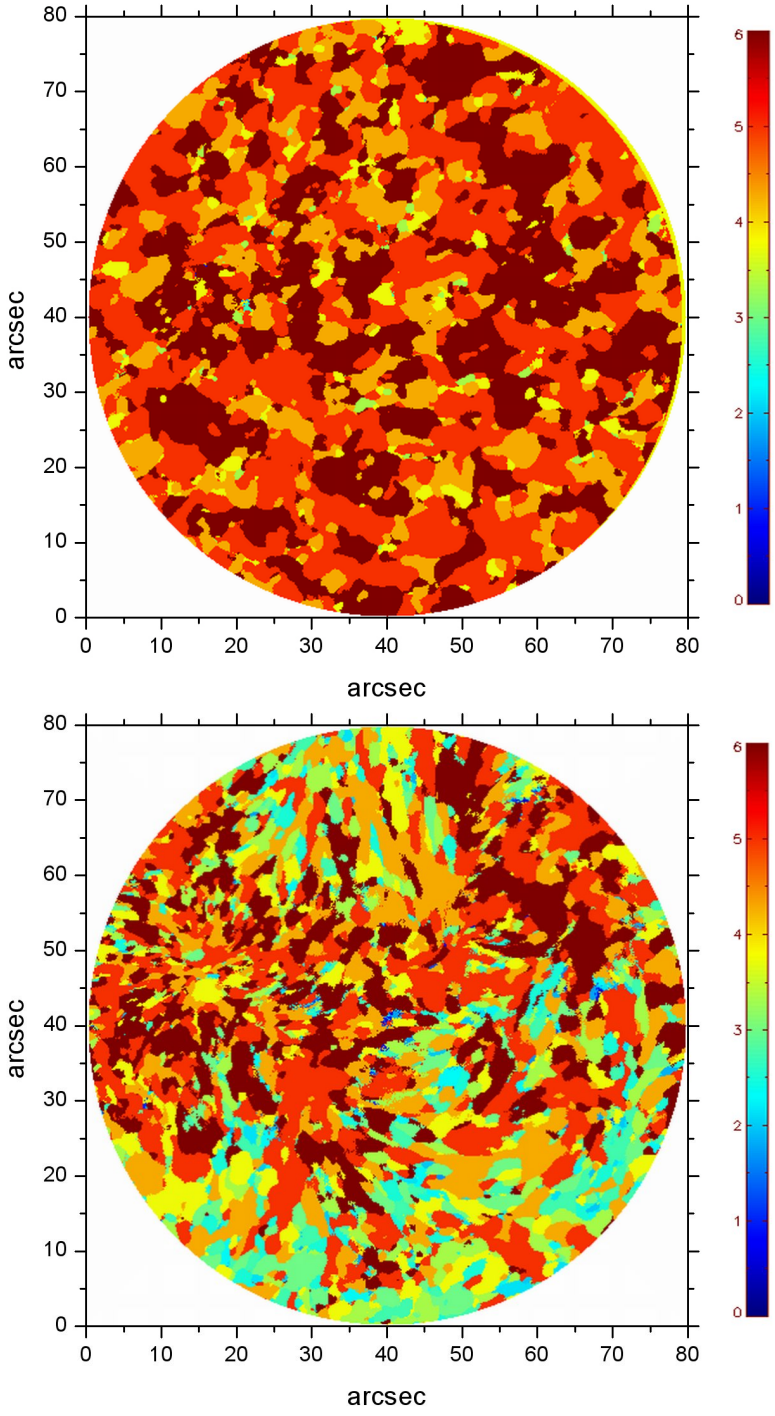

Figure 4.20: Maps of "frequencies of maximum spectral power" computed from Fe I 709.0 nm LoS velocity signal (*right panel*) and Ca II 854.2 nm line core intensity signal using a 200-point FFT. Color scale in minutes.

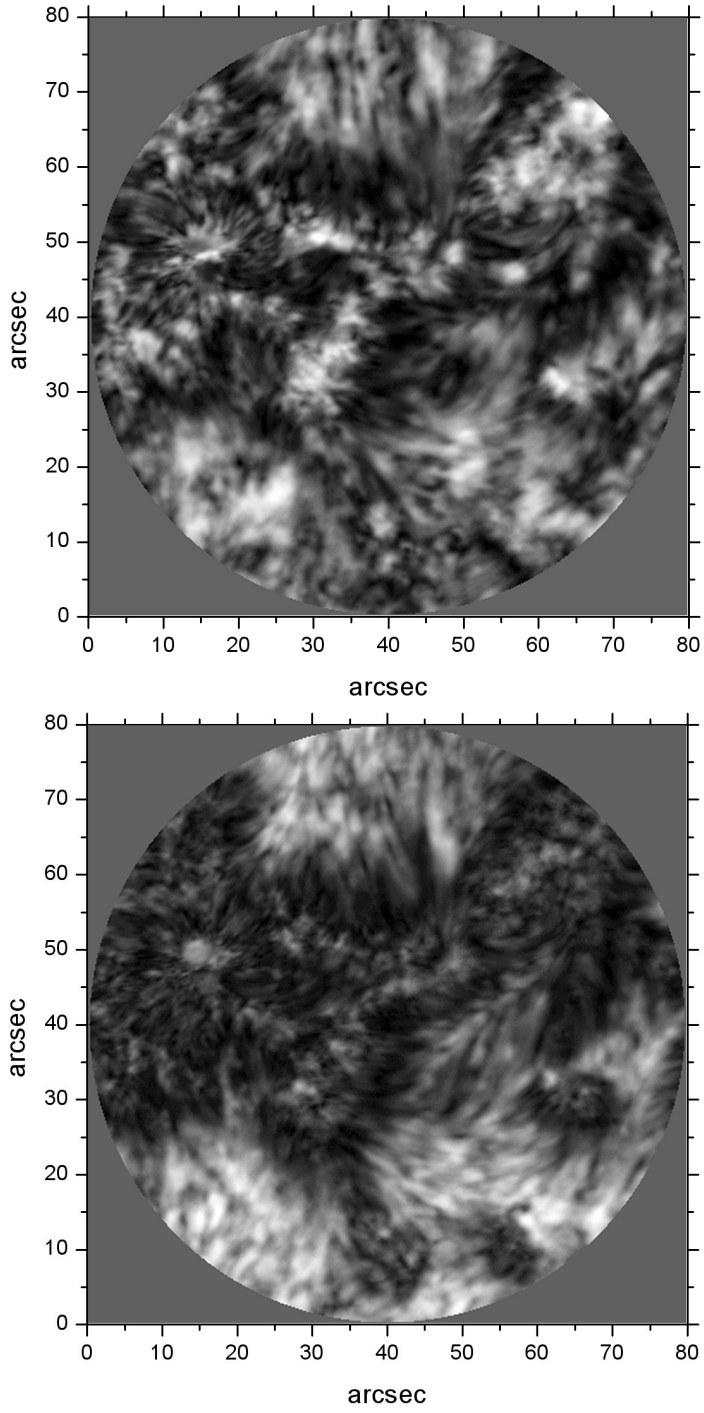

Figure 4.21: Ca II 854.2 nm line core intensity power maps, calculated over the full observing period, and averaged over two selected temporal frequency bands: 2.8-3.9 mHz (the "evanescent" range) and 5.5-8.4 mHz (the "high frequency" range).

4.3 Analysis of the distribution of magnetic elements in MDI magnetograms by a voids method

The solar atmosphere, acting as a nonlinear dissipative system subjected to an external forcing (i.e. non-zero energy flow), presents a state of reduced symmetry with the consequent formation of spatial structures and temporal evolution of associated patterns. This physical framework is complicated by the differential rotation of the whole solar structure, and by the rising and dissipation of magnetic field advected by matter flows.

The spatial features emerging on the solar surface are usually considered as a direct manifestation of convective matter flows, originating in the outer layers of the solar structure and occurring on different scales. They are traditionally classified by size and lifetimes as patterns of granulation (1 Mm, 0.2 h), mesogranulation (5-10 Mm, 5 h) and supergranulation (15-35 Mm, 24 h). Studying such photospheric structures is important to understand processes occurring just below the solar surface.

One of the main topics in solar research is understanding how turbulent convection on the Sun transports mass and energy through the convection zone, how it couples with the magnetic field and how it manages to deposit the energy released from the corona in the higher parts of the solar atmosphere.

Granulation was observed for the first time by Herschel (1801) and identified as convection by Unsöld (1930). For such a pattern a correlation between intensity and velocity, and thus a direct verification of its convective origin, has been unambiguously provided (Richardson & Schwarzchild, 1950; Stuart & Rush, 1954; Plaskett, 1954; Leighton et al., 1962; Canfield & Mehltretter, 1973). A comparison between high-resolution observations of continuum intensity (de Boer et al., 1992; Wilken et al., 1997; Hirzberger et al., 1997, 2002) and Doppler velocity (Nesis et al., 1992, 1993, 1997; Krieg et al., 2000; Berrilli et al., 2001; Hirzberger et al., 2002) indicates that granules consist of an ascending part flowing seemingly in laminar regime, surrounded by more turbulent downflow lanes.

The supergranulation, first discovered by Hart (1956) by analyzing self-correlating solar dopplergrams, was described in detail by Leighton et al. (1962). This scale is visible both as a vertical and horizontal velocity pattern. The last can be detected either by direct Doppler measurements away from disk center (Leighton et al., 1962; Deubner, 1971; Giovanelli, 1980; Rimmele & Schroeter, 1989; Srikanth et al., 2000; Hathaway et al., 2002) or, near disk center, by tracking the advection of magnetic elements or smaller scale flows (Simon, 1967; November & Simon, 1988; Simon et al., 1988; Wang & Zirin, 1989; Muller et al., 1992; November, 1994; Wang et al., 1996; Zhang et al., 1998a,b; Roudier et al., 1999; De Rosa et al., 2000; Shine et al., 2000; Lisle et al., 2000).

The intermediate-scale pattern, known as mesogranulation, was first reported by November et al. (1981). It can be observed from Doppler measurements of vertical velocities, or from tracking of granules. Mesogranules seem to be advected to the boundaries of supergranules (Muller et al., 1992; Shine et al., 2000), disappearing on their way. However, the origin and even existence of mesogranulation is still an open topic.

All these features were initially considered as a direct manifestation of vari-

ous sized convection cells (Schrijver et al., 1997; Raju et al., 1999). Their origin is sometimes related to the ionization of H, He and He^+, which occur at depths in the solar interior coinciding with the three convective scales. However, the complex observational scenario seems not to be describable by a conventional convective origin. Moreover, the attempts to measure a convective temperature gradient correlated to the meso-and supergranular pattern produced ambiguous results. Such an uncertainty is related to the difficulty in disentangling intensity signals arising from different small-scale contributors such as granulation and weak magnetic elements (Rast 2003). More recently, on the basis of observations (Oda, 1984; Straus et al., 1992; Straus & Bonaccini, 1997; Lawrence et al., 1999; Rieutord et al., 2000; Muller et al., 2001; Berrilli et al., 2005) and numerical simulations (Rast, 1995, 1999; Ploner et al., 2000), some authors suggested a different scenario according to which meso- and supergranulation do not represent the surface outcome of large-scale convective motions, but arise from a collective interaction of the granules.

The interaction between photospheric convective flows, which determine the formation of the above described cellular patterns, and the solar magnetic field influences the spatial configuration and the evolution of magnetic elements in the outer layers of the Sun.

This interaction has been a subject of study for many years. Magnetic fields emerge on the solar surface forming a wide variety of structures. According to the different morphology of magnetic fields at the photospheric level, the solar surface can be divided into active and quiet regions. The emergence pattern of active regions and their spatial distribution are believed to be a direct manifestation of the solar dynamo.

It is well known that the magnetic field in the solar atmosphere originates from magnetic elements in the photosphere. Plasma flows in the photospheric layers carry the magnetic field to the edges of the supergranular convection cells, resulting in a larger magnetic flux along the cell boundaries than in their interiors. This results in the so-called magnetic network, which is made up by concentrations each carrying a magnetic flux in the range of 10^{18} to 10^{19} Mx with field strengths of the order of kilo-Gauss (Schrijver et al., 1997). The upward extension of these boundaries is observed as network lanes, which are bright in chromospheric emission, increasing in contrast with height and showing contrast ratios of nearly an order of magnitude larger in the extreme-ultraviolet (Reeves, 1976). As stated in the previous section, it is believed that the network magnetic field provides the basic channel for energy transport and heating of the solar chromosphere and corona and for the acceleration of the solar wind (Reeves, 1976; Gabriel, 1976; Marsch & Tu, 1997; Vocks & Mann, 2003; Aiouaz et al., 2005). Knowledge of the geometric expansion of the network with height can provide constraints on the energy budget of the solar atmosphere.

The bright chromospheric network, which keeps track of the turbulent flows occurring in the convective zone below, is usually used as a describer to individuate and study the properties of the supergranule cells. In the past some authors attempted to derive mean values of cell sizes from the spatial scale of the distribution using the autocorrelation two dimensional analysis, while others derived their results by analyzing dimensions of visually identified cells in CaK digitized spectroheliograms. In particular, Leighton et al. (1962) derived the mean cell size of the supergranular pattern by computing the average distance between

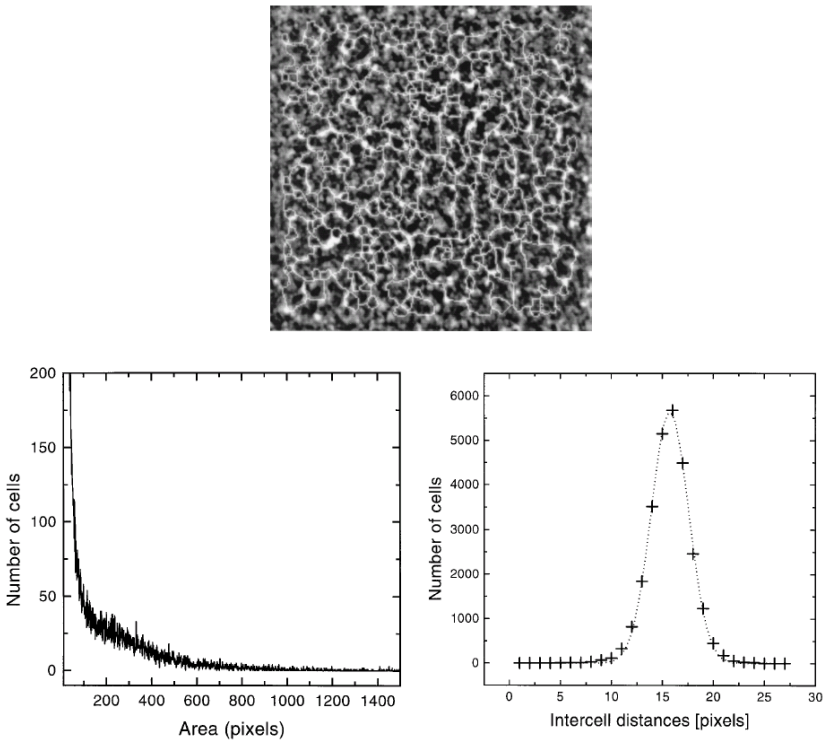

Figure 4.22: *Top*: Skeleton (light line) superimposed on the corresponding PSPT Ca K intensity image. *Bottom, left panel*: distribution of cell areas (Berrilli et al., 1997); *bottom, right panel*: histogram of calculated inter-cell distances (crosses). The dotted line shows a Gaussian fit on the data.

the centers of adjacent cells in the velocity pattern they observed. Subsequently, results of an autocorrelation analysis carried out by Simon & Leighton (1964) showed that, like photospheric granulation, supergranulation exhibits a fairly large spread in individual cell sizes, ranging from 20 Mm to 55 Mm.

Berrilli et al. (1997) developed an image processing procedure able to automatically isolate the brighter boundaries of the network cells from a sample of PSPT (Precision Solar Photometric Telescope) Ca K images. Such a procedure consists in applying an algorithm of skeletonization, based on that developed by Zhang & Suen (1984), on a binary image representative of the chromospheric network, in which pixels set to "1" are representative of the network, while pixels set to "0" contain mainly the solar background. The distribution of the areas of the cells thus identified (about 24000) shows a continuous increase of the number of cells toward the smaller scales (Fig. 4.22). The authors derived also the mean distance between the barycenters of adjacent cells by performing a triangulation on their positions (Fig. 4.22). The distribution of intercell distances is described by a Gaussian function characterized by a mean intercell distance of 23Mm and a FWHM of 5 Mm. As reported by Roudier & Muller (1987) or by Title et al. (1989) for granulation, the pattern of the supergran-

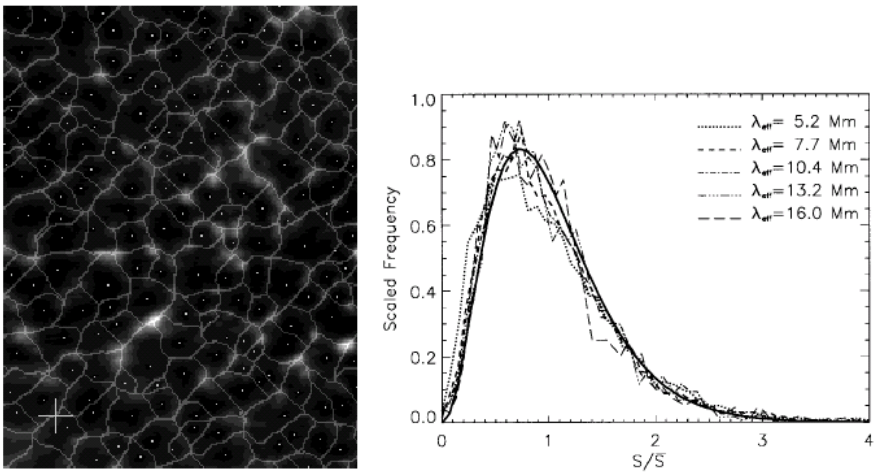

Figure 4.23: (*Left panel*): Cell outlines plotted over the averaged Ca K intensity image; (*right panel*): Distribution functions for different spatial smoothings, λ_{eff}, and for a temporal smoothing Δt=8 hr, scaled to the same width and total surface (Hagenaar et al., 1997).

ules, as derived by the chromospheric network, may be characterized by a mean intercell distance, while it does not show a mean cell size.

As opposed to the previous threshold method, Hagenaar et al. (1997) applied a gradient-based method to identify supergranular network from an uninterrupted two-day sequence of Ca II K images, acquired with a 10 cm aperture telescope located at the South Pole (Jefferies et al., 1988). This method allows the network to be defined by only moderate intensity differences. The surface is tassellated along "high ridges" into a collection of "basins": the algorithm groups pixels into a pattern of areas ("basins") within which hypothetical precipitation anywhere onto that area collects at the same point. That collection point is found by stepping down from pixel to pixel in the direction of the nearest neighbor with the lowest intensity until a minimum is reached.

Before applying the algorithm, as the network, consisting of separate flux concentrations of different size and brightness, looks incomplete, a temporal averaging is applied to increase the signal-to-noise ratio and to trace all locations where flux has appeared at some point in the time interval considered. Moreover, a spatial smoothing fills in the network at locations where it is not fully defined.

The authors determined the distribution function of cell areas for different spatial smoothings (Fig. 4.23) and, in any case, found a broad, asymmetric spectrum of areas. The distribution is found to be invariant for different spatial smoothings if the cell areas are normalized to a unit mean. Extrapolation of the average cell size to zero spatial smoothing yields a characteristic cell diameter of L=13-18 Mm. This is roughly half the generally quoted supergranular length scale L≈32 Mm as determined with autocorrelation methods.

The region in between network structures, the inter-network, is not field-free (Livingston & Harvey, 1975), but shows a small average flux density appearing

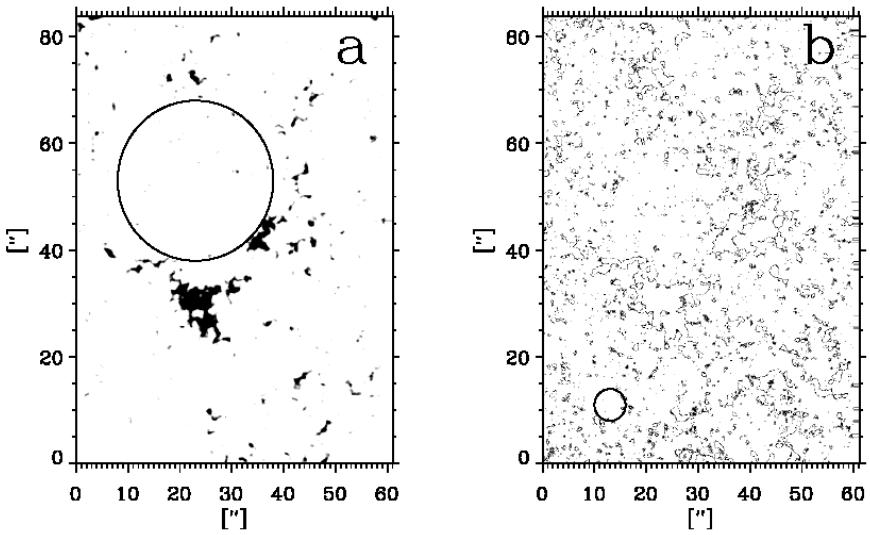

Figure 4.24: Full FoV magnetogram showing signals within a certain range of flux densities. a) Strongest signals in the magnetogram, i.e., those whose unsigned flux density is larger than 150 G. They trace the network. (The artificial circle, with a diameter of 3000, has the typical size of a network cell.) b) Only strong IN signals are shown (flux densities between 60G and 100 G). The circle has a diameter of 600, typical of the mesogranular pattern (from Sánchez Almeida, 2003).

to be of the order of a few to 50Mx/cm^2. It is believed that a substantial fraction of the quiet photospheric field is locally generated by a dynamo action driven by convective motions, namely the granular flows (Cattaneo, 1999). Granules may generate magnetic fields in the interior of supergranules, in the so called internetwork, which may harbor most of the unsigned magnetic flux on the solar surface. The residual from such fields can be transported to the boundaries of supergranules by the horizontal flows.

From magnetoconvection simulations it results that at the granular scales the magnetic fields are concentrated in the boundaries of the granules (in intergranular lanes) also driven by the granular horizontal flows. Such numerical results have been recently confirmed by observations (Lin & Rimmele, 1999; Domínguez Cerdeña et al., 2003; Khomenko et al., 2003). The presence of magneto-convective concentration also at mesogranular scales has been predicted by numerical simulations (Cattaneo et al., 2001) and then recently observed with 2D spectro-polarimetry (Domínguez Cerdeña et al., 2003), IR spectropolarimetry (Trujillo Bueno, 2003) and from magnetograms (Sánchez Almeida, 2003).

Domínguez Cerdeña et al. (2003), by using a time series (40 min) of high spatial resolution images of intensity and simultaneous magnetograms, found the existence of a web-like pattern with the spatial scale of mesogranulation (say, between 5" and 10"). More in detail, the mesogranular structures, detected by computing their horizontal velocities using local correlation tracking (LCT, (November & Simon, 1988)), in magnetograms correspond to a strong

concentration of magnetic flux, which seems to be carried by the horizontal motions of the plasma. Such a result is confirmed also by Sánchez Almeida (2003). By analyzing a set of magnetograms, the author showed how the strongest magnetic signals trace a network with scales similar to meso and supergranulation. Fig. 4.24 contains two versions of the full FoV magnetogram showing signals within a certain range of flux densities. The magnetic signals larger than 150 G concentrate on a network cell, with dimension typical of a supergranule. Analyzing only magnetic signals whose absolute value ranges between 60 G and 100 G, voids with the mesogranular size are present.

Following the paper of Sanchez Almeida we study the scale distribution of magnetic intercluster voids. In order to obtain a more objective criterion, voids between magnetic fragments are detected applying a numerical algorithm. This automatization of void searching is able to give a more uniform and objective picture of the void structure of different particle distributions.

4.4 Void-searching algorithm

Void searching algorithms are largely used in cosmology to study the spatial galaxy distribution of the Universe. The most prominent features of the large scale structure of the Universe are voids, the discovery of which is important for theoretical models about the origin of the structure of the Universe.

For each application, the main goal of a void searching algorithm is to detect voids and quantify their properties in an automated and objective manner, not biased by the human eye. Several methods for void searching have been developed, each one based on a different void definition. When developing such algorithms, it is necessary to know exactly what one is looking for.

The first work identifying voids in a quantitative manner is that of Vettolani et al. (1985), which examined ensembles of empty cells. They center a sweeping sphere on each galaxy, classifying as impure all cells that are in contact with it. These cells are discarded and a void is defined as an ensemble of pure cells. Einasto et al. (1989) approximate the minimum diameters of voids by using a definition of voids as empty spheres. A different definition of voids is used by Ryden (1995) and Ryden & Melott (1996), who search for elliptical empty regions in two-dimensional particle distributions varying the shape and direction of the ellipses. In order to find arbitrarily shaped voids, other algorithms have been developed. For example, Kauffmann & Fairall (1991) use an algorithm which consists in putting into the galaxy distribution the largest possible cube not containing galaxies and then completely mapping the void by adding smaller rectangular volumes outside the parent cube. El-Ad et al. (1996); El-Ad & Piran (1997) search for empty regions by connecting spheres with variable radii $r < r_{min}$.

In our work we adopted the algorithm developed by Aikio & Mähönen (1998) in order to find voids in three dimensional redshift surveys. Before implementing the algorithm, we have to define a void. Let us consider a distribution of particles in a square region $\mathrm{L}^2 \in \Re^2$ with side length L. We define a scalar field, called *distance field* (DF), $D : L^2 \rightarrow R$ as the distance of a given point x in L^2 to the nearest particle:

$$D(x) = \min_n \{ \mid x \quad X_n \mid \} \tag{4.8}$$

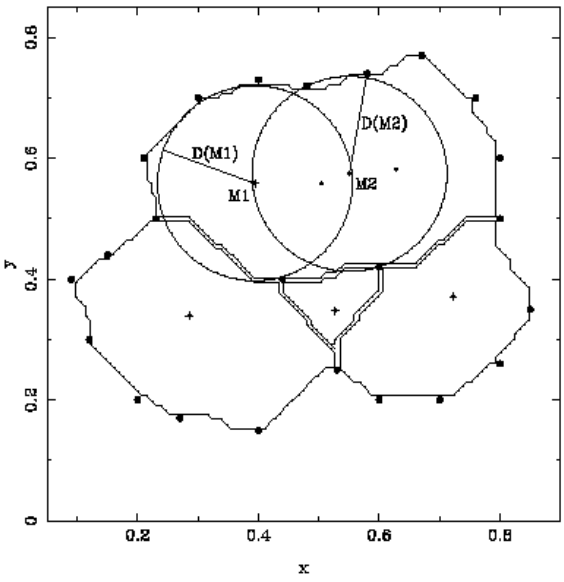

Figure 4.25: Example of a two-dimensional particle distribution with four voids. Dots denote the maxima of the DF while crosses mark the main maxima of voids. Circles with radius $D(M_1)$ and $D(M_2)$ are drawn around the two maxima M_1 and M_2. The two subvoids can be joined because the distance between the maxima M_i is smaller than the distances $D(M_i)$. Since $M_1$is the main maximum of DF inside the void, the radius $D(M_1)$ is the main radius of the void (from Aikio & Mähönen, 1998)

.

where X_n, n=1,. . ., N are the locations of the particles. The local maxima of DFs, which are the points in L^2 with the longest distance to the nearest particle correspond to the "centers" of empty regions.

To numerically calculate the DF, we divide the region L^2 into k^2 *elementary cells*, where $k = L/s$ and s, called a *resolution parameter*, gives the spatial resolution of the void analysis. For each elementary cell, we calculate the minimum of distances to the particles, so obtaining a discrete DF, D(x). Then we calculate the local maxima of DF, (let M_i be the cell corresponding to the maximum of DF). It is possible that more than one maximum of a DF, with approximately the same values of the DF, falls inside a void. Such local maxima belong to subvoids of the same void. Let $M \in L^2$ be a local maximum of the DF and $v_m \subset L^2$ a region around M. We define v_m as a subvoid if moving from a point $x \in v_m$ in the direction of the highest ascent of the DF we end up at the maximum M. Although a subvoid clearly belongs to one determined void, the subvoid does not necessarily cover the whole void volume. Let the distance between maxima M_1 and M_2 be $d_{1,2} =\mid M_2 \quad M_1 \mid$. We say that subvoids v_{M_1} and v_{M_2} belong to the same void V if

1. the maxima M_i and M_j are nearer to each other than the nearest particle, i.e.

$$d_{i,j} \leq \min\{D(M_i), D(M_j)\} \tag{4.9}$$

where $D(M_k)$ is the value of the DF at point M_k;

2. if there exists a chain of subvoids $\{v_{M_k}\}_{k=1}^{n}$ such that $d_{i,1} \leq \min\{D(M_i), D(M_1)\}$, $d_{k,k+1} \leq \min\{D(M_k), D(M_{k+1})\}$ for all k=1,. . . , n-1 and $d_{n,j} \leq \min\{D(M_n), D(M_j)\}$ (i.e. there exists a chain of subvoids obeying the condition in Eq. 4.9).

In Fig. 4.25 a two dimensional particle distribution with four voids is illustrated. The local maxima of the DFs (centers of subvoids) are shown by dots, while crosses mark the main maxima of voids. In the topmost void, four subvoids are detected. They belong to the same void as they satisfy the condition 2.

Once the elementary cells M_i corresponding to main maxima have been identified and labelled, we have to determine the void which the rest of the elementary cells belong to. This is done by using the "climbing algorithm". The void to which an elementary cell x belongs is found by climbing from x to the neighboring cell of x, say x', with the highest value of DF. The climbing continues from x' to the neighboring cell x" that again has the highest value in the DF. The climbing stops when a maximum cell M_i is achieved. The cell x, and all the elementary cells along the path, belong to the same void as M_i.

The output data of the algorithm are the number and locations of the elementary cells in each void. The area of the void is the number of cells in the void, n_A, multiplied by the volume of elementary cells, s^2. The main radius of the void, R_V, is defined as the maximum of the DF inside the void, i.e. it is the maximum of the DF maxima $D(M_k)$ inside the void:

$$R_V = \max_{M_k \in V} \{D(M_k)\} \tag{4.10}$$

The corresponding elementary cell is called the *main maximum* of the void M_V. The main radius defines the radius of the *central* (or *main*) *circle* of voids.

4.5 Applying the algorithm to simulated distributions

Before applying the algorithm to real distributions of magnetic field on the solar surface, we have tested it on some simulated patterns. Our goal is simply to verify that our algorithm works reliably. We start our analysis with the most simple distribution of particles. Fig. 4.26 (*left panel*) shows a 210×210 two-level image obtained by displacing particles, of linear dimension m=1 px, on a square lattice, with a lattice constant m_l=10 px. The centers of each void, corresponding to the maxima of the distance fields (DFs) inside a void, are marked with red crosses.

In the right panel of Fig. 4.26 are the voids found by the algorithm labeled with different colours. In Fig. 4.27 we report the distribution of the radii and of the areas of the identified voids. The algorithm identifies 400 voids with a radius equals to 7.07 and and area of 81 pixels. The area of the void is calculated by counting the number of elementary cells (in our case one pixel corresponds to an elementary cell) inside each identified void.

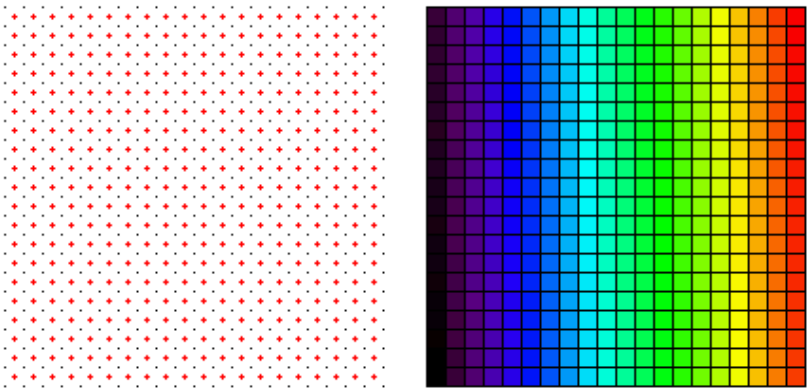

Figure 4.26: (*Left panel*): 210×210 two-level image in which particles, of linear dimension m=1 px, are distributed on a square lattice with a lattice constant m_l=10 px. Red crosses mark the void centers, corresponding to the maxima of the distance fields (DFs) inside a void. (*Right panel*): voids found by the algorithm are labeled with different colours

.

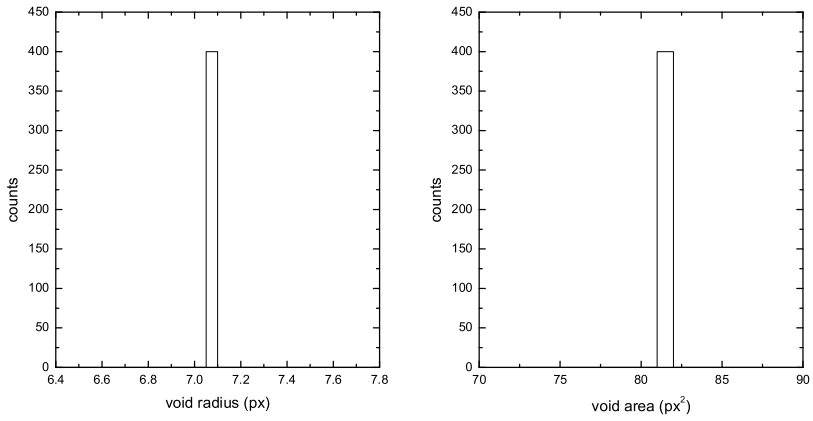

Figure 4.27: Distribution of the void radii (*left panel*) and areas (*right panel*) for the simple pattern shown in Fig. 4.26

.

In Fig. 4.28 (*left panel*) we report another example: a 232×247 two-level image obtained by displacing particles, of linear dimension m=1 px, on a hexagonal lattice with a lattice constant m_l=10 px. In the right panel of Fig. 4.28 are the voids found by the algorithm labeled with different colours. By studying the distribution of void radii and areas (Fig. 4.29) we find 210 voids with a radius equals to 9.43 and and area of 224 pixels.

In Fig. 4.30 we show three samples of pseudo-random patterns obtained by

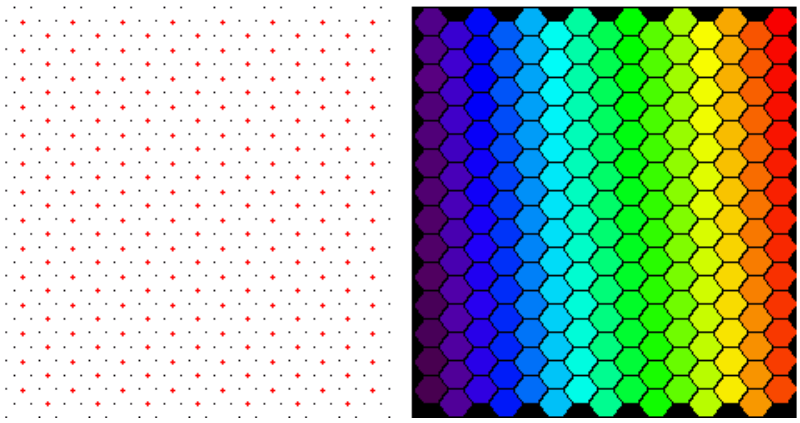

Figure 4.28: 232×247 two-level image obtained by displacing particles, of linear dimension m=1 px, on a hexagonal lattice with a lattice constant m_l=10 px. The center of each void is identified by a red cross

.

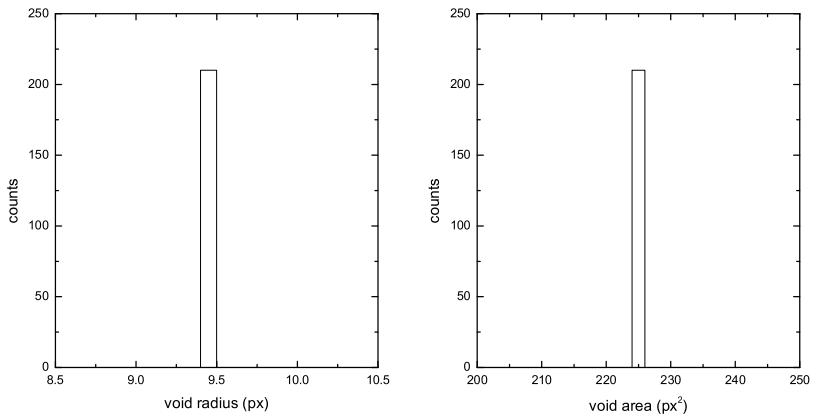

Figure 4.29: Distribution of the void radii and areas for the pattern shown in Fig. 4.28

.

displacing N_{st}=100, 500, 1000 non-overlapping structures on a 250×250 matrix. The corresponding void size distributions, obtained by summing the histograms of 100 samples, are reported in Fig. 4.31. In any case the histogram shows a maximum corresponding to the mean correlation distance among structures, $r_c = \left(D^2/N_{st}\right)^{1/2}$, where D is the image dimension (D=250). The test problems reveal the ability of the void searching algorithm to determine the spatial scale of a distribution of discrete structures; nevertheless, we note that the method alone cannot discriminate between different physical mechanisms generating the

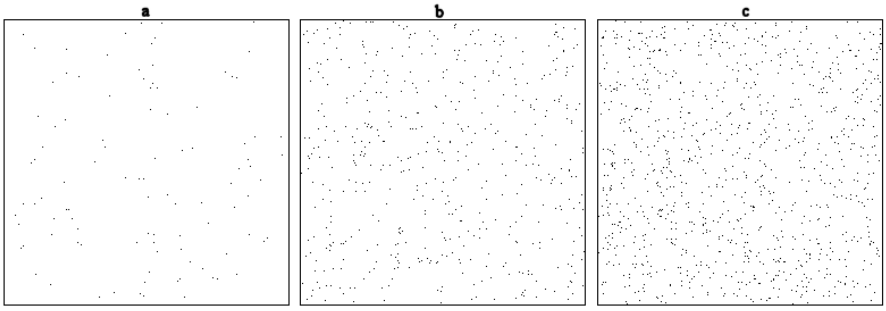

Figure 4.30: Three samples of pseudorandom patterns of 100 (a), 500 (b) and 1000 (c) nonoverlapping structures.

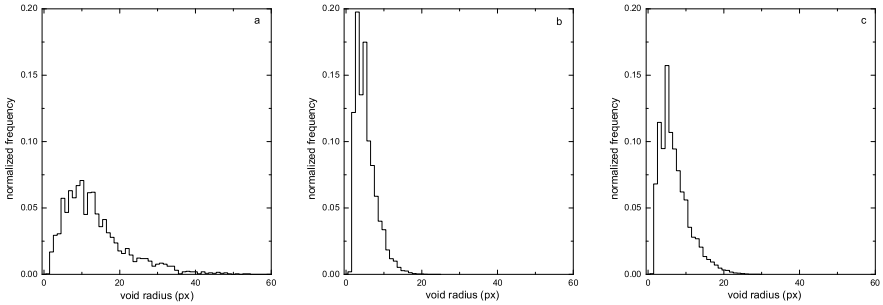

Figure 4.31: Distribution of the void radii for the three pseudo-random reported in Fig. 4.30. Each histogram is obtained by summing the histograms of 100 samples.

same topological features.

4.6 Applying the algorithm to MDI magnetograms

We present here some results obtained by applying the void searching algorithm to a series of MDI magnetograms. The Solar Oscillations Investigation / Michelson Doppler Imager (SOI/MDI) instrument is a state-of-the-art helioseismology experiment and magnetograph on board the SOHO spacecraft, devoted to studying the interior structure and dynamics as well as the surface magnetic field of the Sun. This instrument gives an image of the Sun, which is recorded by a 1024×1024 CCD camera, and can observe in two spatial resolution modes, full disk and high-resolution of the central part of the disk (HR). Two tunable Michelson interferometers allow MDI to record filtergrams centered at five wavelengths across the Ni I 676.8 nm absorption line. From the filtergrams, MDI computes the following six observables: Doppler velocity, continuum intensity, line depth, longitudinal magnetic field, horizontal velocity and limb position.

The SOI/MDI instrument is described in detail by Scherrer et al. (1995).

Here we focus our analysis on high resolution magnetograms at the 1.8 level, i.e. the last level provided by the MDI/SOHO team. The images have a field of view of 620"×620" and a pixel size of 0.605"×0.605". MDI magnetograms are usually obtained every 96 minutes, with the exception of periodic campaigns in which 1-minute cadence measurements are available. Magnetograms only measure net magnetic flux per resolution element, therefore the signal is not the true magnetic field strength B, inside a flux tube, but its longitudinal component, $\langle \mid B \mid cos\gamma \rangle$, averaged over the pixel, where γ is the angle between the magnetic vector and the line of sight. For simplicity, we hereafter refer to $\mid B \mid < cos\gamma >$ as B.

Our dataset consists of 160 high resolution magnetograms acquired in different days in the period from April, 1996 to December, 1997, near the solar activity minimum. We selected only magnetograms with a low activity so that only quiet network was present on the solar surface. All images were rebinned 512×512, leading to a pixel scale of 1.21"/pixel. The surface distribution of solar magnetic features is identified by setting a threshold equal to $3\sigma_{mag}$, which corresponds on average to 15 G. In this way we obtain a two-level representation of the magnetic field: when the absolute value of a pixel of the magnetogram will be greater or equal to the threshold value, the corresponding pixel of the two-level representing map will be set equal to 1; otherwise, it will be set equal to 0. To reduce false detections, even at the risk of missing active pixels, we reject all isolated pixels above the given thresholds assuming that they are noise.

Once we have obtained these two level maps, we search for "voids" between magnetic structures, by applying our procedure, and study the distribution of their dimensions. In Fig. 4.33 (*left panel*) we report the distribution of void diameters. It is obtained by summing the histograms of the dimensions of the voids identified in the 160 analyzed two level-maps. The histogram is normalized to area unity.

As a first result we note that the histogram is characterized by a pronounced peak for small dimensions (1.76 Mm). Two effects contribute to produce this small scale peak. First, it is possible that the algorithm is identifying voids on a smaller (granular) scale, revealing that some magnetic structures organize themselves on such a scale. The second explanation derives from the fact that the solar network (see Fig. 4.32) is not a continuous structure, but it is made up of single and not connected magnetic structures. While our eye is capable of "joining the dots" and identifying a number of structures as lying on the same "contour" that identifies a void, the algorithm cannot. As it is based on a computation of distances, it might identify a void between two close but not connected structures, belonging to the network. This could lead to an apparently high count of small voids.

Apart from the first peak, the histogram shows a large spread in the individual cell sizes, up to $\sim$ 60 Mm.

A more sensitive measure is the normalized MDI void distribution N'=N/N_r, where the distribution of void sizes (N), as identified from MDI magnetograms, is divided by the void sizes distribution for a completely random system (N_r) obtained by randomly disposing a number of points, equal to the mean number of magnetic structures identified in MDI magnetograms (around 2500 structures), on a matrix of the same dimension as the analyzed MDI images (512 ×

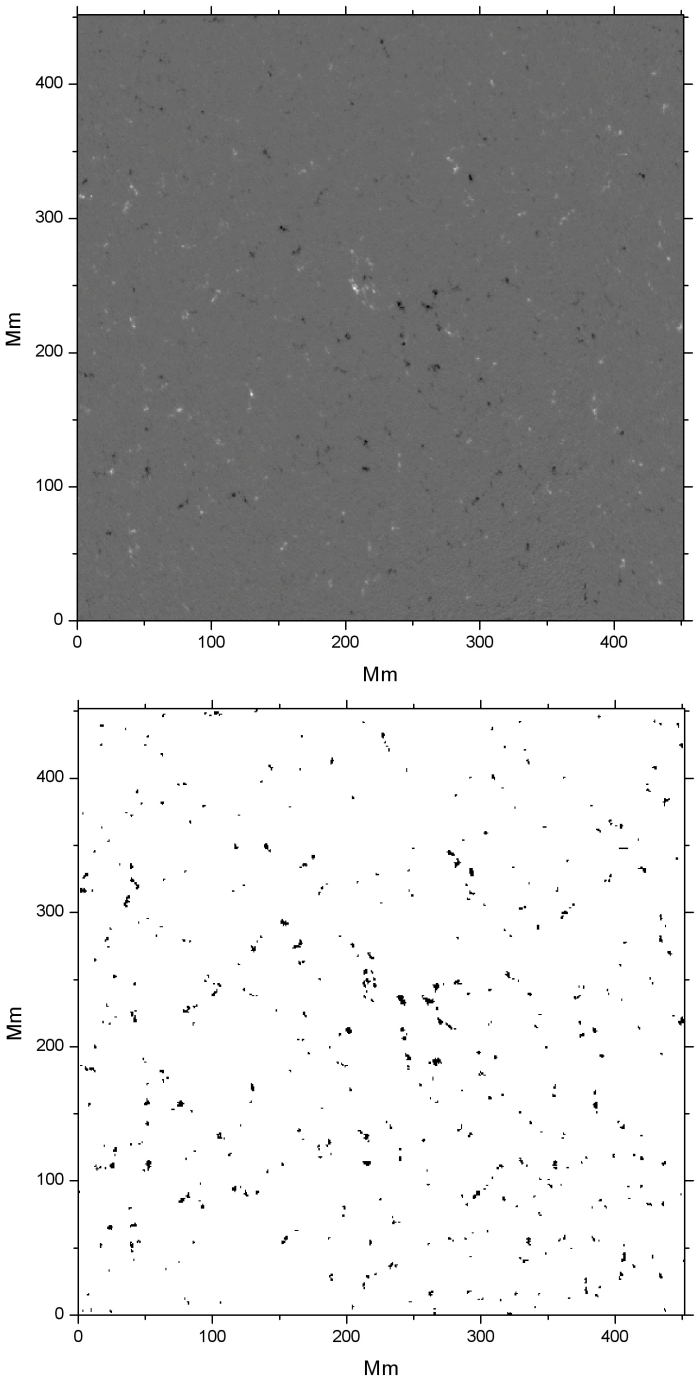

Figure 4.32: Example of a high resolution MDI magnetogram (*top*) and the corresponding binary image, representative of the magnetic network (*bottom*), on May 2, 1996.

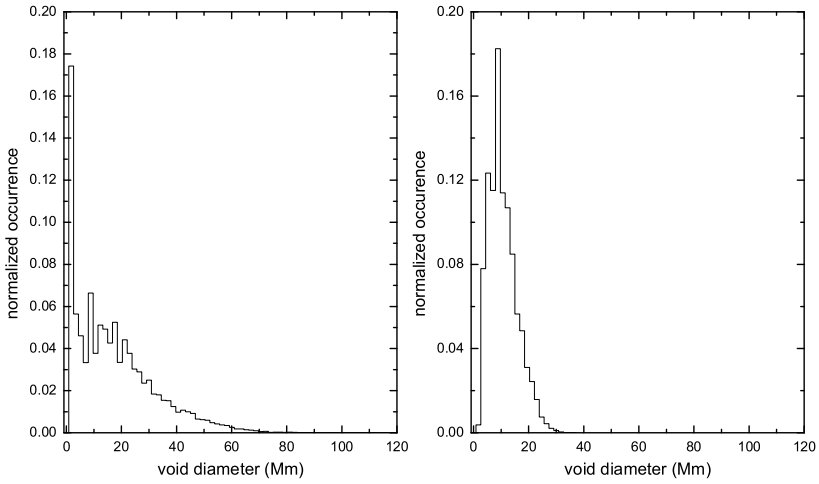

Figure 4.33: Distribution of void diameters (in Mm) for the 160 MDI binarized magnetograms (*left panel*) and for a pseudo-random distribution (*right panel*) having a particle density comparable to that of MDI binarized data.

512 pixels). The distribution of void diameters obtained for a random system is reported in Fig. 4.33, (*right panel*). As previously discussed, the histogram, normalized to unity area, shows the emergence of a typical void size, corresponding to the mean correlation distance among structures.

By comparing the two histograms we conclude that the distribution of the magnetic elements on the solar surface is not random.

In fig. 4.34 we plot, in a semi-logarithmic scale, the normalized MDI void distribution N'=N/N_r. Three regions can be identified in the histogram.

- A region, under 5 Mm, probably corresponding to the immission scale of the magnetic field.
- An intermediate region, between 5 Mm and 60 Mm which results exponentially distributed. In order to define a characteristic length scale, we fit the histograms with an exponential law (Fig. 4.34):

$$N'(D) = N'(0) \times e^{D/d} \tag{4.11}$$

We derived $d = 7Mm$ as the characteristic void scale. This length can be interpreted as the spatial organization scale of magnetic clustering regions.

This is the result of a preliminary analysis; further work is needed to better interpret the Void Distribution Functions describing the magnetic field distribution on the solar surface.

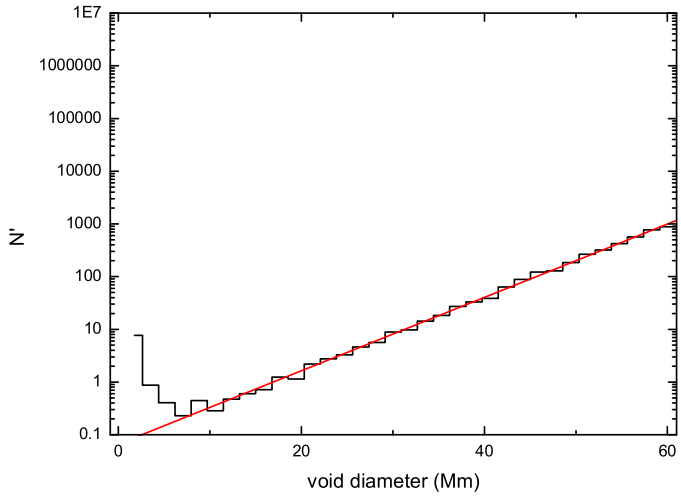

Figure 4.34: Normalized MDI void sizes distribution N'=N/N_r, where N_r is the void sizes distribution for a completely random system and N is the distribution of void sizes as identified from MDI magnetograms. Red line is exponential fit to the data.

Chapter 5

Conclusions

In this thesis we have addressed the basic problem of the connection between solar magnetic fields and photospheric dynamics working on three topics: first, the study of next generation sensors for solar imaging spectroscopy; second, the development and implementation of a complete reduction pipeline for the data acquired with the IBIS spectrometer; third, the study of the emergence and organization of the magnetic field on the solar surface, both as isolated and as clusters, through the analysis and interpretation of IBIS (Interferometric BIdimensional Spectrometer) and MDI (Michelson Doppler Imager) data.

The results can be summarized as follows:

- Two sensors, the SI-1920 HD CMOS sensor and the Andor IXON DV885 EMCCD sensor, were studied and calibrated in the laboratory. Our interest in these sensors originates from the necessity to replace the CCD camera currently installed on the IBIS spectral channel, in order to increase the efficiency of IBIS data acquisition.

  Measurements and calibrations of both sensors are reported. From the linearity tests, repeated for three different readout rates (13, 27 and 35 MHz) it resulted that the EMCCD sensor responds in a linear manner over a wide dynamic range. The same bahaviour was obtained also for the SI-1920 HD CMOS sensor.

  By applying the Photon Transfer Technique, we derived a conversion factor of $\simeq 1.06\ e^-$/ADU and a readout noise of $\simeq 13\ e^-$ for the camera working at 13 MHz. On the other hand, the photon transfer curves obtained for higher readout rates (27 and 35 MHz) and for higher signals deviate from a linear behaviour. This behaviour can be interpreted as due to an inefficiency in the readout process. During this phase, a part of the collected charge is not transferred from one pixel to another, causing a smoothing in the signal fluctuations.

  For the SI-1920 HD CMOS sensor we obtained a conversion factor of $\simeq 13.2\ e^-$/ADU and a readout noise of $\simeq 3.6\ e^-$.

- A pipeline for the IBIS data calibration has been developed, in IDL environment, in collaboration with the IBIS team.

  The first step in IBIS data reduction is to correct both the data and the flatfield images for dark current and CCD non-linearity effects. As

concerns the flatfield correction, we have to consider the classical mounting of the two FPIs, which causes a systematic blueshift of the instrumental profile when moving from the optical axis towards the edge of the FoV, therefore reaching its maximum in the outermost pixels. This blueshift effect has to be taken into account in the construction of the gain table.

- A pore with a light bridge (AR10812) was studied using high spatial and spectral resolution images acquired with IBIS.

  From MDI/SOHO magnetograms and continuum images the pore, initially composed of two structures with the same polarity, disappeared three days after our observation. Such a topology allowed us to relate the observed light bridge properties to the contiguity of two flux tubes.

  We analyzed the intensity images provided by the broad-band channel of IBIS, by the red wing of Ca II 854.2 nm line and by the G-band channel, both used as magnetic proxy, and simultaneous and cospatial Fe I 709.0 nm line LoS velocity maps.

  - We studied global properties of the pore by performing radial profiles, of intensity and velocity mean maps, starting from the pore geometrical barycenter and averaging them over the azimuth. From these profiles three different regions were identified. The first one, corresponding to the pore umbra, is a quasi-plateau of about $200 m \cdot s^{-1}$, compared to the quiet mean granular velocity set to zero. The second region, that we defined as the rim, extends from the pore boundary, as defined by the maximum of intensity derivative, up to 4.6" from the pore center. This region is characterized by strong downflows of about $350 m \cdot s^{-1}$ and rms fluctuations of $\simeq 100 m \cdot s^{-1}$. The third region, that we take as reference, corresponds to a normal granulation region extending away from the pore center, from 6.1" to 8.2".
  - We investigated the LoS velocity behaviour in the rim region via a time-slice approach. This analysis revealed that the negative average value of the LoS velocity in this region is due to a downflow strucuture that is present for the whole dataset duration, but it is irregular in space and intermittent in time. Moreover, a strong downflow plume (up to $1 km \cdot s^{-1}$) is recurrent in the upper-left boundary of the pore.
  - We computed the probability distribution functions (PDFs) of the LoS velocity in the three regions: i.e., the umbra ($\sim 7 \times 10^4$ measures), the rim ($\sim 10^5$ measures), and a surrounding annular region of granulation ($\sim 1.3 \times 10^5$ measures). We found a quasi-gaussian behaviour inside the pore umbra and in the surrounding quiet granulation region. On the other hand, the rim is characterized by a non-gaussian distribution, with extended exponential tails. This shape can be read as an evidence of the presence of several populations associated with different convective features, separated by a structured magnetic field.
  - An analysis of the intensity maps revealed the presence, along the light bridge axis, of an elongated dark structure, matching a feeble upward plasma structure in the range 50–100 $m \cdot s^{-1}$, flanked by two

downflows, around -150 m·s^{-1}. An important outcome of our analysis is the reversing in the LB of the intensity and velocity. It recalls the *inverse granulation* phenomenon, which consists in the inversion of temperature fluctuations, with respect to the velocity field, in the upper photosphere. However, the inverse granulation phenomenon involves the upper quiet photosphere, whereas dark intensity features in broad-band channel images refer to a zero altitude photosphere.

We interpreted this sort of reversed convective feature as related to a geometric effect due to the superposition of the convective flow pattern with a field free region (i.e., with high opacity).

- We developed a simple light bridge thermal model in which we consider a quiet field free region below a magnetic region that has been partially emptied of plasma. This model is able to qualitatively reproduce the observed intensity behaviour inside the light bridge.

- We analyzed the oscillatory properties of different regions of the solar surface, by adopting the IBIS dataset: a pore with a light bridge, a network region and an internetwork region. In particular we studied the chromospheric oscillations, in relation to the underlying photosphere, with particular regard to the effects of magnetic topology.

  - All analysis we carried out showed a period of oscillation, inside the pore, of ∼3 minutes in the chromospheric layer and of ∼5 minutes in the photosphere.

    By analyzing the space-time diagrams of the chromospheric intensity signal, we observed a clear structure resembling a "chevron" in correspondence of the pore umbra. While three minute oscillations are a common phenomenon in the chromosphere umbra of most sunspots and pores, clearly distinct "chevron" structures do not appear so frequently. The presence of these chevron structures is a clear sign of propagating wave motions in the umbra chromosphere, with a phase velocity of ∼20 km $^{-1}$. The spatial scale of the "chevron" structure corresponds to the umbra size, countering the hypothesis of a possible connection between the three minute oscillations and running penumbral waves.

  - The same analysis carried out in chromospheric network and internetwork regions showed that while the internetwork is dominated by oscillations with a period of about 3 minutes, in the network the dominant wave period is around 5 minutes. Jefferies et al. (2006) showed that quiet magnetic network elements provide "portals" through which low-frequency magneto-acoustic waves can propagate into the solar chromosphere. Such waves contribute to heat the solar chromosphere more than high frequency acoustic waves. Such results have been recently confirmed by Vecchio et al. (2007) who show that a large fraction of the chromospheric acoustic power at frequencies below the acoustic cutoff, residing in the proximity of the magnetic network elements, directly propagates from the underlying photosphere.

  - Another interesting feature resulting from the analysis of the "maximum power frequency" map is the lack of 3-min power in regions,

called "magnetic shadows", surrounding the pore and the network. This property is a consequence of the interaction between the upward-traveling acoustic waves (the global p-modes) on one side, and the expanding magnetic fields of the pore and of the magnetic network elements on the other.

- We studied the spatial distribution of magnetic structures observed in MDI magnetograms through a statistical method. We developed a void searching algorithm, such as those largely used in cosmology to study spatial galaxy distributions. This method, applied to a temporal series of MDI magnetograms, allowed us to identify voids between magnetic structures and to study the scale distribution of magnetic intercluster voids. A sensitive measure of the spatial distribution of magnetic structures is the normalized MDI void distribution N/N_r, that is defined as the ratio between the distribution of magnetic cluster voids (N) and the void distribution for a random system (N_r). This random configuration is obtained by randomly scattering a number of points, equal to the mean number of magnetic structures identified in MDI magnetograms (around 2500 structures), on a matrix of the same dimensions as the analyzed MDI images (512×512 pixels). From the N/N_r histogram it results that the size of identified voids follows an exponential law, which allows us to define a characteristic length, equal to 7 Mm. This length can be interpreted as the spatial organization of magnetic clusters.

Appendix A

Theory basics

A.1 MHD equations

The large variety of physical processes related to the dynamic interaction between convectively driven motions and magnetic fields in an electrically well-conducting fluid is commonly indicated with the term 'magneto-convection'. Under the conditions of the convection zone and of lower solar atmosphere, the plasma and its interaction with electric and magnetic fields is well described by the standard *magnetohydrodynamics* (MHD) *approximation*. It consists in combining the Maxwell equations, which describe the electro-magnetic field, with the equations of hydrodynamics.

We begin with Maxwell's equations for the magnetic field $\mathbf{B}$, the electric field $\mathbf{E}$, and the electric current density $\mathbf{j}$:

$$\nabla \cdot \mathbf{B} = 0 \tag{A.1}$$

$$\nabla \cdot \mathbf{E} = 4\pi\rho \tag{A.2}$$

$$\nabla \times \mathbf{E} = \frac{1}{c}\frac{\delta \mathbf{B}}{\delta t} \tag{A.3}$$

$$\nabla \times \mathbf{B} = \frac{4\pi}{c}\mathbf{j} + \frac{1}{c}\frac{\delta \mathbf{E}}{\delta t} \tag{A.4}$$

The MHD equations are based on the following assumptions:

a) The plasma motions are non-relativistic, i.e.

$$\frac{v}{c} \ll 1 \tag{A.5}$$

and if we consider a change of reference frame, $\mathbf{E}$ and $\mathbf{B}$ transform according to:

$$\mathbf{E'} = \mathbf{E} + \frac{\mathbf{v}}{c} \times \mathbf{B} \tag{A.6}$$

$$\mathbf{B'} = \mathbf{B} \quad \frac{\mathbf{v}}{c} \times \mathbf{E} \tag{A.7}$$

where $\mathbf{v}$ is the relative velocity between the two reference frames.

b) Let L and τ be the characteristic length and time scales where $\mathbf{E}$ and $\mathbf{B}$ change. Then

$$\frac{L/\tau}{c} \ll 1 \tag{A.8}$$

This implies that all phase velocities are not relativistic and so no electromagnetic waves occur in this approximation.

c) The plasma is assumed to be highly conducting and charge-neutral. This last assumption is justified by the fact that in photospheric plasma the spatial and temporal scales exceed the Debye length and the inverse plasma frequency by many orders of magnitude.
Owing to the high electrical conductivity electric fields are negligible. Formally, this follows from an order-of-magnitude estimate of Eq. A.3, which governs the electric field in the absence of free charges. We may compare the two terms in Eq. A.3 if we replace the different vectors with their absolute magnitudes and the curl operator with 1/L, where L is the scale of field variation. In this way we obtain:

$$\frac{E}{L} \simeq \frac{B}{c\tau} \Rightarrow \frac{E}{B} \simeq \frac{L}{c\tau} \ll 1 \tag{A.9}$$

With these assumptions it follows that the displacement current can be neglected. In fact

$$\frac{\mid \dot{E}/c \mid}{\mid \nabla \times B \mid} \simeq \frac{E/\tau}{cB/L} \approx \left(\frac{E}{B}\right)^2 \tag{A.10}$$

With the MHD approximations above, Eq. A.4 becomes

$$\nabla \times \mathbf{B} = \frac{4\pi}{c}\mathbf{j} \tag{A.11}$$

and the transformation of $\mathbf{B}$ (Eq. A.7)

$$\mathbf{B'} = \mathbf{B} \tag{A.12}$$

The transformation of $\mathbf{E}$ does not change. According to Eq. A.11 and Eq. A.12 the transformation of the current density is

$$\mathbf{j'} = \mathbf{j} \tag{A.13}$$

By taking into account these transformations, Ohm's law

$$\mathbf{j} = \sigma\mathbf{E} \tag{A.14}$$

becomes

$$\mathbf{j} = \sigma\left(\mathbf{E} + \mathbf{v} \times \mathbf{B}\right) \tag{A.15}$$

Taking the curl of Eq. A.15, substituting $\mathbf{j}$ and $\nabla\times\mathbf{E}$ from Eq. A.11 and Eq. A.3, respectively, and defining the magnetic diffusivity $\eta = c^2/4\pi\sigma$, one obtains the *induction equation*:

$$\frac{\delta\mathbf{B}}{\delta t} = \nabla \times (\mathbf{v} \times \mathbf{B}) \quad \nabla \times (\eta\nabla \times \mathbf{B}) \tag{A.16}$$

This equation describes the evolution of the magnetic field for a given velocity field, $\mathbf{v}$. The first term on the right of Eq. A.16 describes the inducing effect of the material motions upon the magnetic field, while the second one is the diffusion term, which describes the ohmic decay due to the finite conductivity in the plasma. We may compare these two terms by order of magnitude. The ratio of the induction term to the diffusion term is expressed by the dimensionless magnetic Reynolds number:

$$R_m = \frac{vL}{\eta} \tag{A.17}$$

R_m can also be interpreted as a ratio of two time scales, namely the time scale of ohmic decay

$$\tau_D = \frac{L^2}{\eta} \tag{A.18}$$

and the 'advection time scale', l/v.

In stellar atmospheres and convective envelopes the magnetic Reynolds number is large ($R_m \sim 10^3 \quad 10^6$), so that the temporal evolution is dominated by the induction term. A direct consequence of the high magnetic Reynolds number is the concept of "frozen" fields: magnetic field lines are transported by the fluid as if frozen in and fluid motions relative to the magnetic field are possible only along the direction of field lines. Formally, this means that the flux passing through a surface moving with a velocity $\mathbf{v}$ is constant.

The complete set of MHD equations results from combining the hydrodynamic continuity equation, the Navier-Stokes equation, the induction equation for the magnetic field and the thermodynamic energy equation. The continuity equation expresses the mass conservation:

$$\frac{\delta\rho}{\delta t} + \nabla \cdot (\rho \mathbf{v}) = 0 \tag{A.19}$$

The equation of motion is given by the Navier-Stokes equation extended by the Lorentz force

$$\rho \frac{\delta \mathbf{v}}{\delta t} + \rho \left(\mathbf{v} \cdot \nabla\right) \mathbf{v} = \nabla P + \frac{1}{c}\mathbf{j} \times \mathbf{B} + \rho \mathbf{g} + \rho \nu \delta \mathbf{v} \tag{A.20}$$

where ν is the kinematic viscosity and g is the gravitational acceleration.

The energy conservation equation is

$$\frac{\delta e}{\delta t} = \quad \mathbf{v} \cdot \nabla e \quad \frac{P}{\rho} \nabla \cdot \mathbf{v} + Q_{rad} + Q_{visc} \tag{A.21}$$

where e is the internal energy per unit mass, Q_{rad} is the radiative heating and Q_{visc} is the viscous dissipation.

In the equation of motion (Eq. A.20) the Lorentz force ($\mathbf{j} \times \mathbf{B}$) provides a link between the fluid equations and the electromagnetic equations. Given a prescribed flow, $\mathbf{v}$, the induction equation tells us how the magnetic field will evolve in time. As $\mathbf{B}$ changes, the Lorentz force will provide a back reaction on the plasma producing a force that will modify the velocity through the equation of motion. Here we analyze the properties of the Lorentz force and give it some physical meaning. Firstly, by the simple use of Eq. A.11 and a vector identity, the Lorentz force in Eq. A.20 reduces to:

$$\mathbf{j} \times \mathbf{B} = \frac{1}{\mu}(\nabla \times \mathbf{B}) \times \mathbf{B} = \frac{(\mathbf{B}\nabla\cdot)\mathbf{B}}{\mu} \quad \nabla \frac{\mathbf{B}^2}{2\mu} \tag{A.22}$$

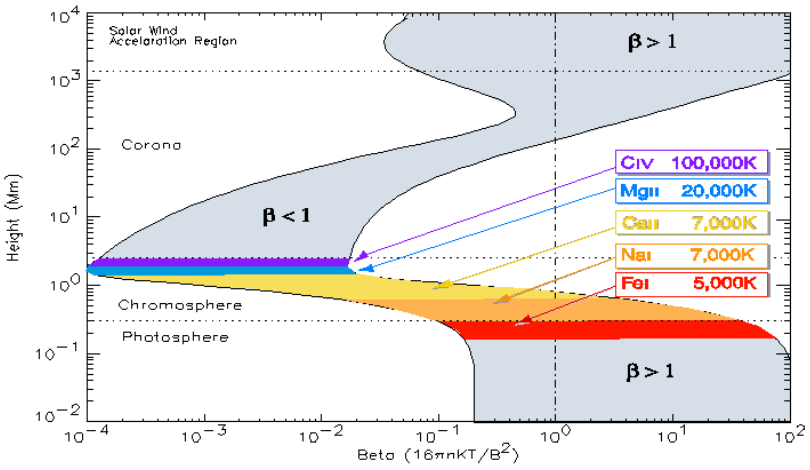

Figure A.1: Variation of the plasma-β as a function of height in the atmosphere.

The first term in the right hand side of the equation represents the effect of a *tension* of magnitude B^2/μ directed parallel to $\mathbf{B}$. This force appears whenever the magnetic field lines are curved. The second term represents the effect of a magnetic pressure of magnitude $B^2/2\mu$ per unit area that is isotropic. This force occurs when the field strength varies from position to position.

In the magnetostatic case, when all quantities are time independent and no flows are present, Eq. A.20 simplifies to:

$$\nabla P = \frac{1}{4\pi}(\nabla \times \mathbf{B}) \times \mathbf{B} + \rho g \tag{A.23}$$

From this equation it is possible to determine an important parameter, called *plasma* β, which is the ratio of gas pressure to magnetic pressure:

$$\beta = \frac{2\mu p}{B^2} \tag{A.24}$$

As we have just said, in the high R_m regime the *flux freezing theorem* applies, according to which magnetic field is transported by plasma motions and vice versa plasma moves along magnetic field lines. The *plasma beta* is important as it establishes which is the prime cause: the magnetic pressure or the gas pressure. In Fig. A.1 we report the behaviour of β as a function of the height in atmosphere.

Below the solar surface the *plasma beta* increases rapidly with depth, reaching values in the order of 10^5 near the bottom of the convection zone. In the photosphere most of the magnetic energy resides in magnetic flux tubes, bundles of nearly parallel field lines representing a high concentration of magnetic field, that cover less than 5% of the solar surface. Thus, locally, in correspondence of these flux tubes, the magnetic energy density can exceed the thermal energy density, giving values of $\beta < 1$, although globally most of the energy is in the form of thermal energy of the gas, so $\beta > 1$.

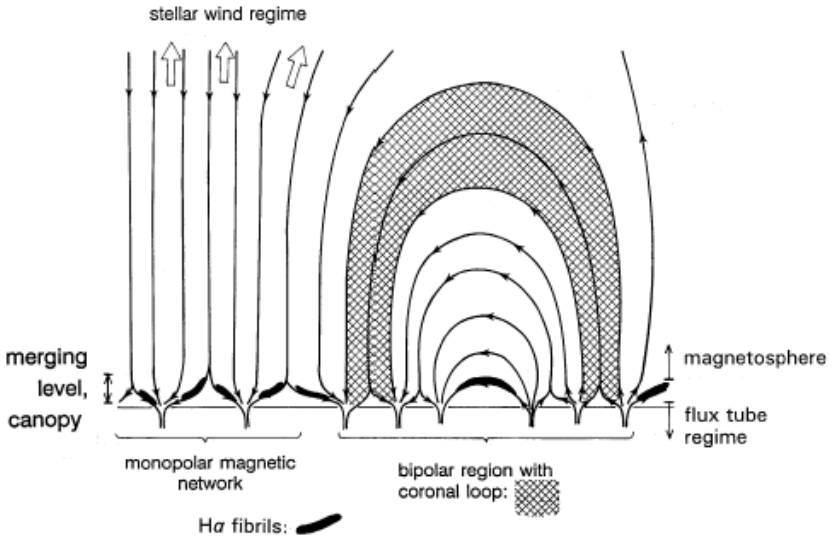

Figure A.2: Magnetic structure in the solar atmosphere. Discrete concentrations of magnetic field, separated by nearly field-free plasma, extend upward through the photosphere and into the low chromosphere. In the upper chromosphere the flux tubes merge, creating the magnetic canopy. The magnetosphere, defined as the domain above the merging level, is pervaded by the magnetic field. The solar wind flows along the magnetic field (wherever it is open) to interstellar space (from Schrijver & Zwaan et al., 2000).

The situation changes rapidly when we move higher in the atmosphere. Initially, both the gas and the magnetic pressure decrease exponentially with height, so that β remains approximately constant. At a certain height, corresponding to the chromospheric layer, the magnetic flux tubes expand filling the whole volume. Beyond this height, the gas pressure drops off nearly exponentially with height, with a scale height of only 150 km, which is much faster than the decline with height of the magnetic pressure. This leads to a situation in which the magnetic field completely dominates the structure and dynamics. Consequently, in the chromosphere and in the corona we have $\beta \ll 1$. The situation changes again in the higher layers of the corona and in the solar wind where particle energy is so high that it dominates the magnetic energy ($\beta > 1$).

This variation in the β regimes corresponds to different "hierachies" between plasma and magnetic field, affecting the magnetic structure in the solar atmosphere (shown in Fig. A.2). The intermittent magnetic flux concentrations in the photosphere expand upwards and merge in the chromosphere. In the corona the magnetic topology is either open and closed. The part of the corona open to interstellar space and heliosphere is called *wind domain* and is characterized by a low mass density and a dark appearance (*coronal holes*), due to a weak emission of radiation. In these regions much of the mechanical energy delivered from the lower atmosphere goes into the acceleration of a fast *solar wind*. On the other side, in the magnetically closed regions field lines bend back to the photospere, forming loop-like structures, containing dense, hot and bright

plasma.

A.2 Oscillation properties of the Sun

A.2.1 Basic properties of adiabatic oscillations

A star like the Sun is a gaseous sphere in hydrostatic equilibrium. Perturbations of this equilibrium give rise to a restoring volume force and can therefore lead to oscillations. Such oscillatory motions on the solar surface are measured by observing the oscillation of the Doppler shift of a spectral line as the plasma producing the spectral line oscillates back and forth along the line of sight, or by observing the oscillation in intensity produced by the waves. These oscillations are known to have a discrete spectrum (Gough and Toomre, 1991) and can be described by eigenfunctions of the wave equation of a spherical system, and can therefore be characterized by the spherical harmonic radial order n, the harmonic degree l and the azimuthal order m of the oscillation mode. In this section we will describe these oscillations under simplifying assumptions.

In most stars, the dynamical timescale is very much shorter than the thermal timescale, and hence everywhere in the star the adiabatic approximation

$$\frac{\delta P}{P_0} = \Gamma_1 \frac{\delta \rho}{\rho_0} \tag{A.25}$$

is satisfied. P_0 and ρ_0 are the undisturbed pressure and density, both dependent on radius r, and δP and $\delta \rho$ are the perturbations suffered by an element of gas as it moves back and forth. The adiabatic exponent,

$$\Gamma_1 = \left(\frac{d\ lnP}{d\ ln\rho} \right)_S \tag{A.26}$$

is related to the adiabatic sound velocity c by

$$c = \Gamma_1 P_0 / \rho_0 \tag{A.27}$$

and it too depends only on depth.

As a further simplification we can neglect the rotation, which is a small effect, of order of Ω/ω, where Ω and ω are the frequencies of rotation and oscillation, respectively. For the Sun $\Omega/\omega = 10^{\ -4}$.

Finally, we adopt the approximation of *linear* oscillations. Non-linear terms in the hydrodynamic equations are of order v/c compared to linear terms. The ratio v/c is very small almost everywhere in the Sun.

Under these assumptions, small-amplitude oscillations of such a star can be separated into normal modes, each of which has a harmonic dependence on time, and depends on the spherical coordinates θ and φ (co-latitude and longitude) as a spherical harmonic.

Therefore, the displacement eigenvector for a single mode can be written in the spherical coordinates (r, θ, ϕ) as

$$\xi = \Re \left\{ \left[\xi_{r,nl}(r), \xi_{h,nl}(r) \frac{\partial}{\partial \theta}, \xi_{h,nl}(r) \frac{\partial}{sin\theta \partial \phi} \right] Y_\ell^m(\theta, \phi) exp(i\omega_{nl} t) \right\} \tag{A.28}$$

where $Y_\ell^m = c_{\ell m} P_\ell^m(cos\theta) e^{im\varphi}$ is a spherical harmonic, P_ℓ^m is a Legendre function and $c_{\ell m}$ is a normalization constant such that the integral of $|Y_\ell^m|^2$ over

the sphere is unity. The dependence of the displacement on the distance r from the stellar center is described by the eigenfunctions $\xi_r(r)$ and $\xi_h(r)$, which are functions only of r, and $\Re$ means the real part.

A given mode is thus defined in terms of three indices. The spherical degree $l = 0, 1, 2, ..., (n \quad 1)$ corresponds to the number of total nodal lines on the surface, and we have

$$\lambda_h l \sim 2\pi R_\odot, \tag{A.29}$$

so that modes of high degree correspond to short horizontal wavelengths at the photosphere. The azimuthal order m ($|m| \leq l$) corresponds to the number of nodal lines in the longitudinal direction on the surface, and the radial order n roughly gives the number of nodal surfaces intersecting the radial direction. The degree of the mode is related to its horizontal wave-number k_h and wavelength λ at radius r by

$$k_h = \frac{2\pi}{\lambda} = \frac{L}{r} \tag{A.30}$$

where $L = \sqrt{\ell(\ell+1)}$.

Small-amplitude oscillations of the solar body about its equilibrium state can be classified into three types according to the restoring force: pressure modes (p-modes), where the pressure is the dominant restoring force; gravity-modes (g-modes), where gravity or buoyancy is the dominant restoring force; and a class of surface or interface modes (f-modes), which are nearly compressionless surface waves.

The equations of motion for adiabatic oscillations, under previous approximations, can be reduced to simpler forms. If we follow Gough's approximation (Deubner & Gough, 1984) we obtain:

$$\frac{d^2\psi}{dr^2} + k_r^2(\omega^2, r)\psi = 0 \tag{A.31}$$

where $\psi = \rho^{1/2} c^2 \nabla \cdot \xi$, ρ and c are the density and sound speed of the equilibrium state. The vertical component of the local wave number k_r is given by

$$k_r^2(\omega^2, r) = \frac{\omega^2 \quad \omega_{ac}^2}{c^2} \quad \frac{l(l+1)}{r^2}\left(1 \quad \frac{N_{BV}^2}{\omega^2}\right) \tag{A.32}$$

Here, ρ and c are the density and the sound velocity, respectively, and ω_{ac} and N_{BV} are the acoustic cutoff frequency and the Brunt-Väisälä frequency defined as

$$\omega_{ac}^2(r) = \frac{c^2}{4H_p^2}\left(1 \quad 2\frac{dH_\rho}{dr}\right) \tag{A.33}$$

and

$$N_{BV}^2(r) = g\left(\frac{1}{H} \quad \frac{g}{c^2}\right) \tag{A.34}$$

This last term defines the natural oscillation frequency of a gas element in a stable atmosphere slowly displaced from equilibrium in a gravitational field.

For the solutions to Eq. A.31 to be wavelike, it is necessary that $k_r^2 > 0$. It can be seen that for spherically symmetrical modes (l=0), this occurs only when ω exceeds the critical frequency ω_{ac}, which is a generalization of the Lamb's

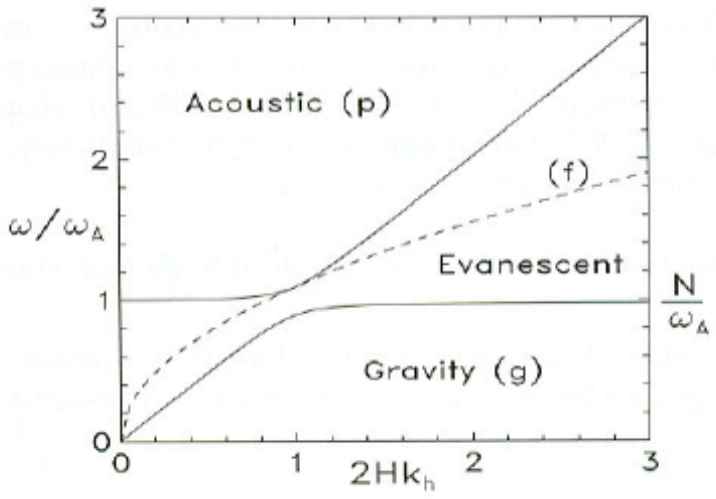

Figure A.3: k_r=0 curves in the k_h ω plane.

acoustical cutoff frequency (Lamb, 1908). For non-radial modes it is convenient to rewrite Eq. A.32 in the form

$$ck_r^2(\omega^2, r) = \omega^2 \left(1 \quad \frac{\omega_+^2}{\omega^2}\right)\left(1 \quad \frac{\omega^2}{\omega^2}\right) \tag{A.35}$$

where

$$\omega_\pm^2 = \frac{1}{2} \; S_l^2 + \omega_c^2) \pm \left[\frac{1}{4} \; S_l^2 + \omega_c^2)^2 \quad N_{BV}^2 S_l^2\right]^{1/2} \tag{A.36}$$

are the solutions of $k_r^2(\omega, r) = 0$ ($\omega_+ \geq \omega$). Here

$$S_l = [l(l+1)]^{1/2} \, \frac{c}{r} \tag{A.37}$$

which is sometimes called the Lamb frequency. It follows that there are two propagation zones in which k_r^2 is positive.These are a region in which

$$\omega^2 > \omega_+^2(r) \tag{A.38}$$

and a region in which

$$\omega^2 < \omega^2 \, (r) \tag{A.39}$$

In regions satisfying the condition A.38 (p-zone), waves propagate as acoustic waves, and in regions satisfying the condition A.39 (G-zone), waves propagate as gravity waves. Otherwise, waves are evanescent. In Fig. A.3 we report the curves k_r^2=0 in the k_h ω plane, or "diagnostic diagram". We distinguish three regions in this plane. First, for large ω Eq. A.32 simplifies to $\omega^2 = c^2 \; k_r^2 + k_h^2)$, which is the dispersion relation of ordinary *acoustic waves*. Its lower boundary lies at ω_A for l=0, and for large l asimptotically approaches the line $\omega = S_l \simeq ck_h$. In the low-frequency region of the k_h ω plane the dispersion relation simplifies to

$$k_r^2 = \frac{S_l^2}{c^2}\left(\frac{N_{BV}^2}{\omega^2} \quad 1\right) \tag{A.40}$$

which is the dispersion relation of *internal gravity waves*. Their region in the $k_h \quad \omega$ plane is bounded by $\omega = N$ for large l and by the line $\omega = S_l N_{BV}/\omega_A$ for small l. The intermediate frequency region of the $k_h \quad \omega$ plane is characterized by $k_r^2 < 0$ and for this reason is called *evanescent-wave region*.

From Eq. A.33 the acoustic cutoff frequency can be seen to increase outward with r. It ranges from $\omega_{ac} \simeq 4 \times 10^{\ 3}\ s^{\ 1}$ (corresponding to a period of ~ 25 min) in the solar interior to $\omega_{ac} \simeq 3.5 \times 10^{\ 2}\ s^{\ 1}$ (corresponding to a period of ~ 3 min) $\simeq 500$ above the photosphere. Waves of frequencies less than the photospheric ω_{ac} bounce back into the solar interior. The outward increase of ω_{ac} thus provides the upper boundary of the cavity required to trap acoustic waves in the Sun. The bottom boundary corresponds to a point of total internal reflection. It is located at $r = r_t$ determined by:

$$\frac{c_s(r_t)}{r_t} = \frac{\omega}{L} \tag{A.41}$$

A mode of oscillation, which is a standing wave, is formed as an interference pattern between such bouncing waves. At low degree, r_t is small, the modes penetrate effectively into the solar core and hence carry information about the entire Sun. However, the amplitudes are largest near the solar surface and much attention is required to extract that part of information which derives only from the deep solar interior.

Similar cavities exist also for gravity waves. These are determined by the behaviour of the Brunt- Väisälä frequency since a gravity wave's frequency must lie below the value of N_{BV}. A gravity wave is prevented by reflection from propagating into a region where $\omega > N_{BV}$. These modes are trapped beneath the solar convection zone, and have large amplitudes in the core, making them potentially very valuable as probes of conditions in the deep solar interior. Unfortunately, their periods are much longer than p- mode periods ($\simeq 50$ min), requiring much longer observational runs, moreover, they have still not been detected without doubt.

A.2.2 The influence of magnetic field on oscillations

The solar atmosphere is stratified due to gravity, so that the density continuously decreases with height. As a result, the atmosphere operates like a high pass in electronics: high frequency sound waves, with wavelengths small compared to the height over which the density drops significantly, travel through a nearly homogeneous, slowly varying gas and can thus propagate virtually without restrictions. Low frequency waves, on the other hand, behave differently. If their frequency falls below the so-called cutoff frequency (or their period exceeds a certain value, which for the Sun is about 3 min), the wavelength becomes so large that these waves see essentially a density jump, which reflects them. Therefore the amplitude of these low frequency oscillations drops rapidly with height, and they cannot transport energy. In the real solar atmosphere another complication arises, namely the presence of magnetic fields.

The effect of strong magnetic field on the two dimensional propagation of waves in a plane-stratified atmosphere has been discussed by Schunker & Cally (2006) and Cally (2006). The governing linearized wave equations may be written in terms of the x and z displacements ξ and ζ:

$$\begin{aligned} a^2 cos^2\theta \left(\frac{d^2}{dz^2} \quad k_x^2\right)\xi + \ \omega^2 \quad c^2 k_x^2)\,\xi \\ = a^2 cos\theta sin\theta \left(\frac{d^2}{dz^2} \quad k_x^2\right)\zeta \quad ik_x \left(c^2 \frac{d}{dz} \quad g\right)\zeta \end{aligned} \tag{A.42}$$

$$\begin{aligned} a^2 cos\theta sin\theta \left(\frac{d^2}{dz^2} \quad k_x^2\right)\xi \quad ik_x \left(c^2 \frac{d}{dz} + \frac{dc^2}{dz} \quad \frac{c^2}{H} + g\right)\xi \\ = \left[c^2 \frac{d^2}{dz^2} + \left(\frac{dc^2}{dz} \quad \frac{c^2}{H}\right)\frac{d}{dz} + \omega^2\right]\zeta + \\ a^2 sin^2\theta \left(\frac{d^2}{dz^2} \quad k_x^2\right)\zeta \end{aligned} \tag{A.43}$$

Here, $a = \left(\frac{B^2}{\mu_0 \rho}\right)^{1/2}$ is the Alfvén speed.

By numerically solving these equations it results that in presence of a magnetic field the acoustic energy and acoustic flux in the low solar atmosphere is very dependent on magnetic field inclination. To be more precise, the surface magnetic field acts as a filter on the ensemble of helioseismic waves below the surface, preferentially allowing through certain waves.

When the magnetic field is vertical, sound waves propagate along field lines unaware of the presence of magnetic field. In presence of an inclined field, the reduced gravity ($\approx cos\theta$) reduces the acoustic cutoff frequency by a factor $cos\theta$ so that the acoustic waves can tunnel through a significantly smaller evanescence region before propagating once again in the upper layers.

Appendix B

Solid state image sensors

This chapter provides an overview of both CCD (Charge Coupled Device) and CMOS (Complementray Metal Oxide Semiconductor) imaging array technologies. The CCD, which has been developed for almost 40 years, is a well-known, mature technology preferred for high quality still photography. Nevertheless, the CCD suffers from a number of drawbacks, including cost, complex power supplies and support electronics. On the other hand, CMOS imaging arrays, which have not yet reached the level of CCDs, are nonetheless set to develop rapidly and offer a number of potential benefits over CCDs.

B.1 Historical background

MOS image sensors were developed before CCD and CMOS. The first solid-state imagers, presented in the 60's and early 70's, used MOS diodes as light sensitive elements. During the 60's numerous groups worked on solid-state image sensors using NMOS, PMOS and bipolar processes. For instance, photodiode image sensors with MOS scanning circuits were known from the mid 60s. In 1963, Morrison reported a structure which used the photoconductive effect to determine a light spot's position. In 1964 IBM reported a *scansistor*, consisting in an array of n-p-n junctions able to produce an output pulse proportional to the local incident light intensity. In 1966, Westinghouse reported an element monolithic array of phototransistors. All of these sensors produced an output signal proportional to the local incident light intensity and did not perform any integration of the optical signal. Consequently, due to the low sensitivity of these devices a gain within the pixel was required to enhance their performance.

The use of p-n junctions in a photon flux integrating mode was suggested in 1967 by Weckler at Fairchild. The incident photons are collected in a reverse-biased p-n junction capacitance and then read by means of a PMOS switch. The signal charge, appearing as a current pulse, is converted to a voltage pulse using a series resistor. In 1968 a 100×100 element array of photodiodes, which Weckler later called *reticon*, was reported.

MOS sensors were not embraced commercially because of large pixel size (for that time) and poor performance. One of the primary problem with MOS and CMOS sensors, until recently, is the FPN (Fixed Pattern Noise). In 1970, when the CCD was first reported, its relative freedom from FPN was one of the

major reasons for its adoption over the many other forms of solid-state image sensors. The smaller pixel size afforded by the simplicity of the CCD pixel also contributed to its embrace by industry.

In the early 1990s, CMOS image sensors re-emerged as an alternative to CCDs thanks to the advantages we will discuss in the last section of this chapter. The first generation of CMOS sensors is represented by passive pixel sensors (PPS) which contained in each individual pixel only a photosensing element and a switching MOSFET. Major improvements in signal-to-noise ratio for photodiodes could be made by adding an amplifier per column or per row. Active-pixel sensors (APS) represent the second generation of CMOS imagers. In such sensors a buffer, which acts as simple source follower, has been implemented in each pixel. CMOS APS (Active Pixel Sensors) promised to provide lower noise readout, improved scalability to large array formats and higher speed readout compared to PPS.

Recently, the research has been focusing, mainly, on the improvement of the APS, which has resulted in a pixel circuit with better performance and flexibility. In order to strongly compete with CCD technology, the aim of researchers has been to obtain higher performance imaging systems based on CMOS technology. Therefore, there have been several reports on improving the fill-factor (FF) with low power consumption, low voltage operation, low noise, high speed imaging and high dynamic range.

Moreover, new applications have emerged due to the CMOS imager development. Automotive applications, imaging for cellular or static phones, computer video, space, medical, digital photography and 3D applications have been improved.

B.2 CCD sensors

The Charged Couple Device (CCD) was invented in 1970 by researchers at Bell Labs and was initially conceived as a new type of computer memory circuit. CCD soon showed to have many other potential applications, including signal processing and imaging, the latter because of silicon's light sensitivity that responds to wavelengths less than 1.1m. The CCD's early promise as a memory element has disappeared, but its superb ability to detect light has turned the CCD into the premier image sensor technology. CCDs have found their way into a huge range of products including fax machines, photocopiers, cameras, scanners and even children's toys.

CCDs consist of thousands (or millions) of light sensitive cells or pixels each capable of responding to the amount of light they receive. Typically, pixels can be arranged in either a single line (linear array CCDs) or in a two-dimensional grid (area array CCDs).

CCDs are in essence integrated circuits (ICs), rather like computer chips. Like integrated circuits, CCDs begin on thin wafers of silicon which are processed with a series of elaborate steps which define the various functions within the circuit. In order to allow light to fall on the silicon chip (or die) a small glass window is inserted in front of the chip. Conventional ICs are usually encapsulated in a black plastic body to primarily provide mechanical strength, but this also shields them from light, which can affect their normal operation. CCDs are manufactured using metal-oxide-semiconductor (MOS) fabrication techniques,

and each pixel can be thought of as a MOS capacitor that converts photons (light) into electrical charge, and stores the charge prior to readout.

B.2.1 CCD fundamentals

Basically, a CCD is an array of numerous individual photo-sensitive elements (pixels) that deliver an electrical signal related to the amount of photons that fall on the pixel surface during the integration time. The basic working principle is related to the photoelectric effect. When a photon is absorbed in the crystalline structure of silicon, its energy is transferred to a negatively charged electron which is then displaced from its normal location in the valence band of the atom into the conduction band. The vacated site is therefore positively charged and is referred to as a hole. In practice, the absorbtion of a photon generates the production of a pair electron-hole. In order to collect the photogenerated charge an electric force field has to be applied to the silicon crystal. This can be achieved by means of a p-n junction (photodiode) or a junction induced by the field formed by a MOS gate (photoMOS).

The CCD is based on MOS (Metal Oxide Semiconductor) technology: it typically consists of a vertically stacked conductive material (doped polysilicon) overlying a generally p-type silicon substrate (approx 300 mm thick) separated by a highly insulating material (silicon dioxide, approx 0.1 mm thick). The resulting structure behaves like a simple parallel plate capacitor which can store electrical charge and is called MOS structure.

By applying a voltage potential to the polysilicon or "gate" electrode, the electrostatic potentials within the silicon can be changed. In particular, the application of a positive voltage to the electrode will repel the holes which are in the majority and sweep out a region depleted of charge just as in the p-n junction. In this way an electrostatic "potential well" forms in the depletion region, whose capacity to store charge can be controlled by the voltage applied on the gate. As the voltage on the electrode increases, the "depth" of the well increases. In order to confine electrons under the gate it is necessary to form zones of higher potentials, called barriers, surrounding the well. Depending on the voltage, each gate can be biased to form a potential well or a barrier to the integrated charge. When the detector is exposed to a luminous radiation electron-hole pairs form, whose holes are driven out of the depletion region and electrons are attracted towards the positively charged electrode. The build up of negative charge is thus directly proportional to the level of incident light.

Once charge has been integrated and held locally by the bounds of the pixel architecture, one must now have a means of getting that charge to the amplifier which is physically separated from the pixels. The charge readout process takes place in two stages. The first involves moving the pixel charges across the surface of the array. The second involves reading out the pixel charges into a register prior to being converted to an equivalent digital value. Regarding the first stage, accumulated charge is first vertically transferred row by row to a special row of CCD pixels called serial register and then horizontally transferred to an output capacitor which makes the charge to voltage conversion. Each column is a shift register and all registers, separated by channel stops, form the parallel register. Each pixel in the serial register corresponds to a column of the parallel register. The way in which the photogenerated charge, and hence the image of the scene, is extracted from the storage/detection site, is called "charge coupling".

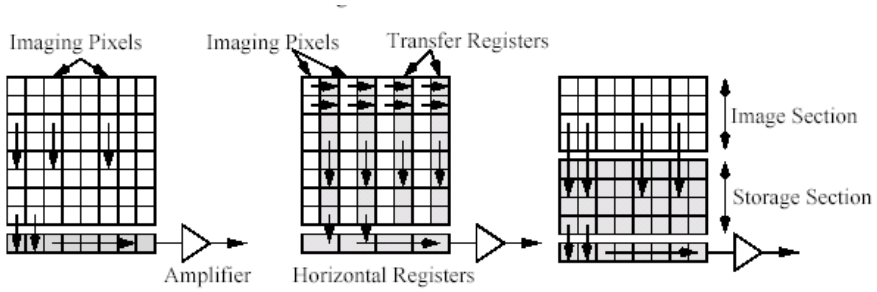

Figure B.1: Area CCD imager readout mechanisms. From left to right: FFT, ILT, and FT.

The three typical transfer mechanisms for an area image sensor are full frame transfer (FFT), interline transfer (ILT), and frame transfer (FT) (Beynon & Lamb, 1980; Buil, 1991), as shown in Fig. B.1. After integration, the image pixels in FFT array are transferred line-by-line to a horizontal serial register, where the charges are clocked out before the next line can be transferred. FFT usually causes smear, since during the readout process, the capacitors are allowed to continue accumulating the light. One improvement is to use ILT, where the readout regions are interspaced between the imaging regions, and are shielded from the light. At the end of the integration period, the charges are transferred horizontally to the vertical readout registers in parallel, and then read out line-by-line in a manner similar to FFT. ILT avoids smear but has the significant drawback that a large portion (typically 40%) of the imaging section is not sensitive to light. Another transfer option is FT, where the array is grouped into two sections: the image section and the storage section. These two sections are identical, except that the storage section is shielded from the light. During readout, charges are transferred line-by-line into the storage section by applying same clocking to both sections. A similar horizontal serial register is used to read out each line from the storage section. During the readout of the first frame, a second one can be collected in the image section.

In any case, charge transfer is achieved by modulating the potential of the bulk silicon using MOS gate electrodes. In particular, each pixel can be made up of one or more electrodes.

A simple CCD structure is shown in Fig.B.2, called three-phase structure, in which three gates are used to define a single pixel. The charge transfer process (Fig. B.3), which in this case occurs in three phases, can be explained as follows. During the integration time, we hold the voltage on the ϕ_1 and ϕ_2 gates high while keeping the voltage low on the ϕ_3 gate. In this way photo-induced charge is collected in the well under the ϕ_1 and ϕ_2 gates. We will say that ϕ_1 and ϕ_2 are in charge holding mode and ϕ_3 is in charge blocking mode. At the end of the integration period, as the timing diagram (see Fig.B.3) shows, ϕ_1 is placed in charge blocking mode, with the effect of transferring the total charge of ϕ_1 and ϕ_2 into only ϕ_2. ϕ_3 is then placed in charge holding mode, which allows the charge in ϕ_2 to distribute itself evenly between ϕ_2 and ϕ_3 (c). Next, ϕ_2 is placed in charge blocking mode, forcing the charge into ϕ_3. The process of raising and lowering the voltage can be repeated over and over and is known as clocking.

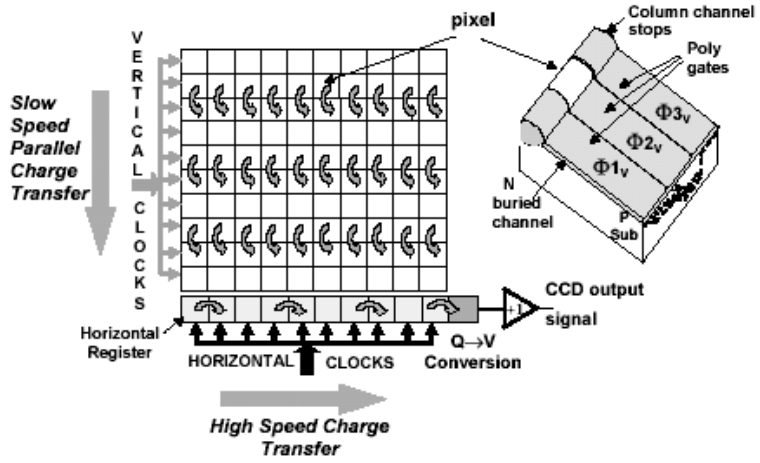

Figure B.2: Three-phase CCD structure: each pixel consists of three gates.

A complete clocking sequence consists of the following steps:

1. a vertical shift of the entire image by one pixel. This delivers a row of charge to the output register;
2. a horizontal shift through all the pixels in the output register. This delivers each charge in that row to the output amplifier, one pixel at a time;
3. another vertical transfer. This delivers the next row in the image;
4. another horizontal transfer.

The above process is repeated until all the rows in the CCD have been delivered to the output register and then to the output sense node where packets of charge are stored and converted to a voltage. Conventional techniques usually employ a "floating diffusion" sense node (essentially a reverse-biased noise) followed by a charge to voltage amplifier such as a source follower. It is called a "floating diffusion" because of the fact that its potential level will vary depending on the amount of charge present on the node. Source followers are used to preserve the linear relationship between light, generated electrons and output voltage. The process begins by resetting the floating diffusion through a reset gate which dictates the reset potential. This reset or zero signal level is converted to a voltage so that the output voltage $V_{out} = V_R$. The charges are then shifted from the last phase within the CCD through the floating diffusion onto an effective storage capacitance C. This causes an instantaneous change V=Q/C in the voltage of the input line of the on-chip transistor which in turn yields a voltage change at the output line by a quantity dependent on the charge content, i.e. on the signal. The resulting change in potential is converted into a voltage and sensed off chip. The difference between the reference or reset level and the potential shift of the floating diffusion level determines the signal. This operation is affected by noise. It is possible to show that the variance of this

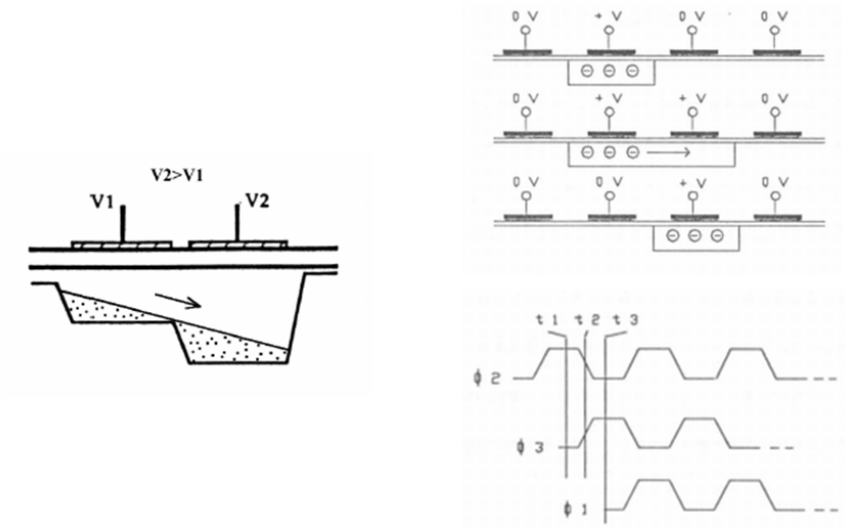

Figure B.3: Charge coupling in a three-phase CCD and timing waveforms for a three-phase CCD. In practice the degree of overlap between one electrode and the next depends on the CCD.

noise is $\sigma^2 = (CV)^2 = kTC$, where k is the Boltzmann constant. It depends on the stray capacity to ground and on temperature. This is called *reset noise* or also *read-out noise*, and it can have rather large values. For this reason some techniques are used to get rid of it, which we will discuss in the following.

B.3 Electron Multiplying Charge Coupled Devices

The sensitivity of a conventional CCD is limited by the noise introduced by the charge to voltage conversion process and by the video chain electronics. The EMCCD (Electron Multiplying Charge Coupled Device) technology removes such limitations by way of a low noise gain process applied in the charge domain, which allows weak signals to be multiplied before any readout noise is added by the output amplifier, hence rendering the read noise negligible. Unlike a conventional CCD, an EMCCD is not limited by the readout noise of the output amplifier, even when operated at high readout speeds. In fact, they enable imaging with a low input noise at pixel rates up to video frame rates and beyond. Since 2001, when they became commercially available, they have had a profound influence on photon starved imaging applications, thanks to their ultra-low noise, high resolution, high quantum efficiency and robustness to over exposure.

The architecture of a frame transfer device designed using the EMCCD technology is shown in B.4. The image, store and read-out register are of conventional design, but there is an extended section "gain" register, known as the multiplication register, between the normal serial register and the final detection node. The multiplication register has several hundred stages, each one

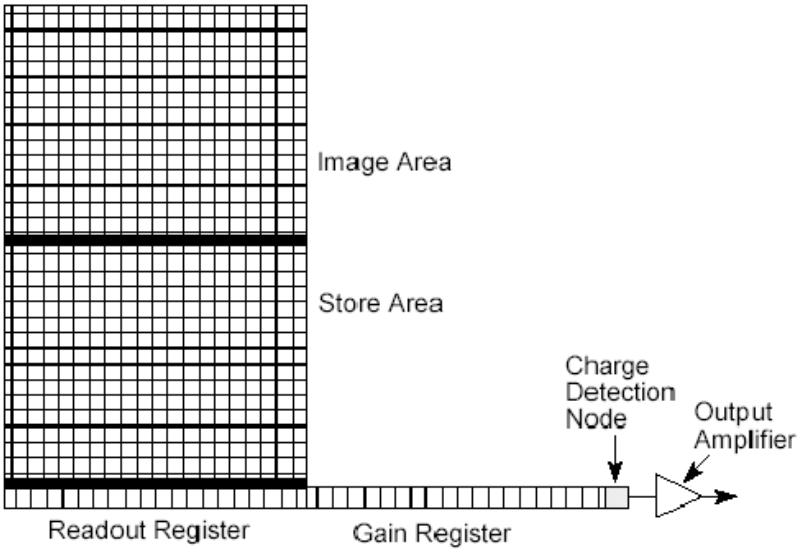

Figure B.4: Schematic of a Frame Transfer EMCCD

comprising 4 gates three of which are clocked. The design of the gain register is shown schematically in B.5. Two of the phases (ϕ_1 and ϕ_3) are clocked with normal amplitude drive pulses (typically 10 volts), whereas the drive pulses of the third phase (ϕ_2) are of a much higher amplitude (typically 40-50 volts). Before each ϕ_2 electrode is another electrode (ϕ_{dc}) held at a low d.c. voltage (typically 2 volts). The potential difference between ϕ_{dc} and ϕ_2 is kept sufficiently high so that electrons transferred from ϕ_1 to ϕ_2 during the normal clocking sequence can experience avalanche multiplication, which thereby increases the number of electrons in the charge packet. The EMCCDs use impact ionisation to provide high gain in the charge domain. The basic principle of charge multiplication in such devices is similar to that of the avalanche photodiode in which in each stage the electrons are multiplied by impact ionisation. The probability of impact ionisation and thus the mean gain at every stage of the register is small (P $< 2\%$) but as the number of elements is large (N > 500), the overall gain can be very high (g $= (1 + \mathrm{P})^N$), with single input electrons giving many thousands of output electrons.

In Fig. B.6 the EMCCD operation is shown. When the photons arrive at the sensor, some will be absorbed and converted into photoelectrons. This process is described by a scaling factor QE_λ:

$$QE_\lambda = \frac{pe_{pre}}{ph} \tag{B.1}$$

When the generated photoelectrons pass through the EM gain stage they are multiplied by a gain factor M:

$$M = \frac{pe_{post}}{pe_{pre}} \tag{B.2}$$

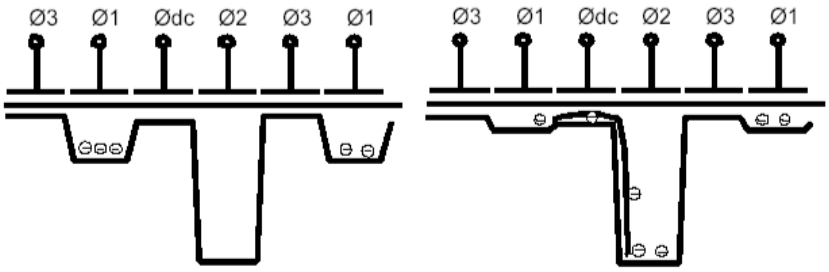

Figure B.5: The transfer of charge through a multiplication element

Finally, the photoelectrons leaving the EM gain stage are converted into a digital number at the ADC. This final gain stage, known as video gain, has a conversion factor A:

$$A = \frac{S_{ADU}}{pe_{post}} \tag{B.3}$$

An important performance parameter for EMCCDs is the noise introduced by the gain process. A noise factor, F, can be defined by the following expression:

$$F^2 = \frac{\sigma^2}{M^2\sigma_{in}^2} \tag{B.4}$$

where M is the mean gain, σ_{in}^2 and σ_{out}^2 are the variances of the input and output signals respectively.

The total variance on the camera output signal is given by

$$\sigma_{tot}^2 = A^2M^2F^2(\sigma_{signal}^2 + \sigma_{dark}^2) + A^2\sigma_{readout}^2 \tag{B.5}$$

where $\sigma_{readout}$ is the readout noise, A is the video chain gain, σ_{signal} is the noise on the optically generated signal S (σ_{signal}^2=S), σ_{dark} is the noise on the dark signal (σ_{dark}^2=S_{dark}). The noise referenced to the image area, σ_{eff} is given by

$$\sigma_{eff} = \sqrt{(F^2(S + S_{dark}) + \frac{\sigma_{readout}^2}{M^2})} \tag{B.6}$$

If the multiplication gain is sufficiently high the effect of the readout noise can be neglected.

B.4 CMOS sensors

For many years, solid-state imaging market has been dominated by CCD sensors. Over the last two decades, there has been considerable research interest in CMOS (Complementary Metal Oxide Semiconductor) image sensors. The idea of MOS imagers was first proposed in late 60s, about the same time as CCD imagers. Because MOS imagers required the incorporation of transistors into pixels, which was not feasible at that time due to large transistor size, CCD imagers have become the dominant solid-state imaging technology ever since.

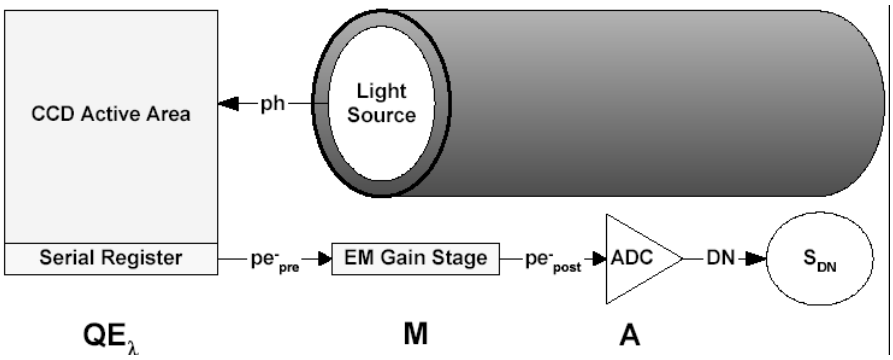

Figure B.6: EMCCD function. The difference between a traditional CCD and an EMCCD is the gain register added between the serial register and the analog to digital converter.

Only recently commercial sensor chips have become available, thanks to the research carried out at the Jet Propulsion Laboratory (JPL). In 1993 they produced a CMOS sensor with a performance comparable to scientific-grade CCDs. The renaissance of MOS imagers is mainly attributed to the down-scaling of the transistor size so that a pixel can achieve a reasonable fill factor.

The CMOS imager is fabricated using a standard digital CMOS process, which is by far the most common and highest yielding chip-making process in the world. Such process is, in fact, used to make millions of chips for computer processors and memory modules. Moreover, CMOS costs are lowered also because they can have processing circuits created on the same chip. With CCDs, these processing circuits must be on separate chips. In the next section, we will highlight some of the advantages and disadvantages CMOS image sensors offer over CCDs.

CMOS sensors, like CCDs, are formed from a grid of radiation sensitive elements, each capable of producing, by photoelectric effect, an electrical signal/charge proportional to the incident light. In general the photo-sensing principle is the same for both devices: they utilize silicon as the sensing material and the photo-charges collected by the image sensors represent the intensity of optical signal. These two types of sensors differentiate, principally, in the photo-charges reading mechanism. Fig. B.7 shows the architecture of a CMOS image sensor, which is similar to a memory array. To read a pixel a row scan circuit and a column scan circuit decode a supplied address and enable the row and column lines of the pixel. As with cells in a memory array, all pixels in a column drive a common buffer via a shared column bus. When a particular row is selected, all pixels in that row drive their respective column buffers. All column buffers drive a common amplifier via a single output bus. Only one buffer, selected by the column scan circuit, operates at a time. Thus, by scanning the address space, each pixel may drive its photogenerated signal to the output amplifier. Thanks to this organization, CMOS sensors, unlike CCDs, provide random access to pixel and direct windowing capability at very high frame rates and avoid the multiple charge transfers over long distances of the CCD architecture that are very sensitive to radiation degradation.

Apart from the readout process, another difference between CCD and CMOS

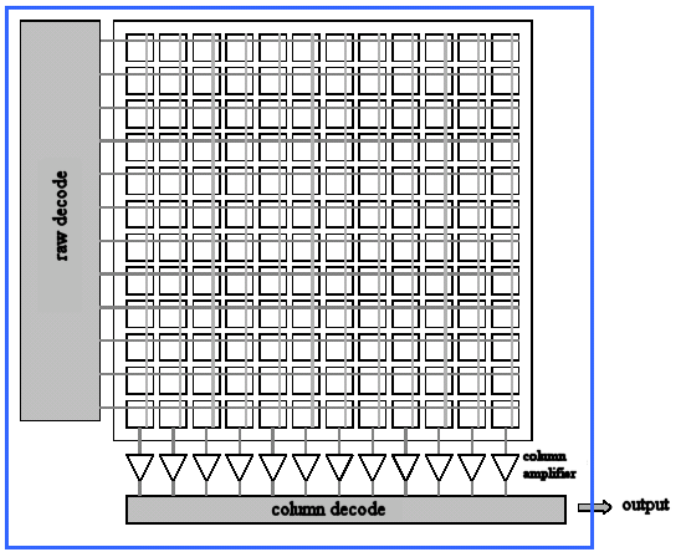

Figure B.7: CMOS image sensor architecture

sensors is the pixel structure. The main contribution of CMOS sensors is the combination inside the pixel of the photodetector, the charge-to-voltage conversion and transistors providing buffering and addressing capability. This unique feature allows for a memory-like organization, where most of the operations are performed in the voltage domain. Like in CCDs, light striking the photodetector creates charge carriers that are used to produce a signal, which may be a voltage or current. The way in which the signal is produced and the type of signal depends on the pixel design.

CMOS image sensors typically come in two forms: *passive pixel* and *active pixel*. Passive pixel devices have charge amplifiers at the bottom of each column of pixels, with each pixel having just a single transistor (in addition to the photodiode and capacitor). This transistor is used as a charge gate and switches the contents of each pixels capacitor to the charge amplifier. Active pixel arrays implement an amplifier in every pixel, as we will discuss in the following. The two different detector types are illustrated in Fig. B.8.

Unlike CCD sensors, in a CMOS pixel different types of photodetectors can be employed, according to the specific requirement (feeble flux, spectral response, etc.). The most common photodetector is the photodiode, which is a *p-n* junction diode operating under reverse bias. Incident light generates a photocurrent, proportional to the incident light flux, which adds to the reverse saturation current of the diode. There are two pixel circuit arrangements to detect incident photons: *current configuration* and *integration* (or *precharge) configuration* (see Fig. B.9).

Current-mode operation - This is the simplest configuration: information about the quantity of incident light is obtained by measuring the current pro-

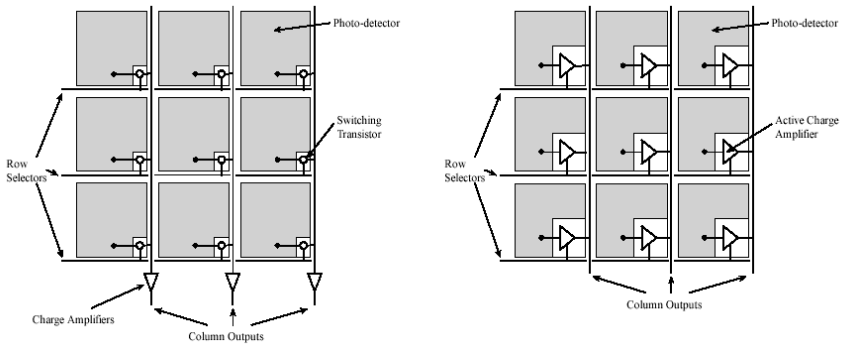

Figure B.8: Passive (*left panel*) and Active (*right panel*) Pixel CMOS Arrays

duced by the photo-generated electrons. This current, on first order, is given by the following expression:

$$I = I_0 AH \tag{B.7}$$

where:
I is the basic photosensitivity for the *p-n* structure ($A^{-1} \cdot m^{-2} \cdot lux^{-1}$);
H is the illumination level (lux^{-1});
A is the photosensitive area (m^{-2})
A great advantage of the current-mode of operation is the increased dynamic range for a limited supply voltage. Because the polarization voltage does not change, the response function is linear for a large range of light intensities. The pixel structure in current-mode operation is shown in Fig. B.9. It consists of three transistors:
M3 is the transistor transferring the pixel signal to the analogic bus;
M2 is the transistor amplifying the diode voltage (in the case of an active pixel sensor);
M1 is the transistor providing the charge-to-voltage conversion.

Integration-mode operation - The integration mode of operation is the most common method used to increase the pixel output signal. In this configuration the pixel employs a photodiode, a capacitor and up to three transistors. Prior to the start of the integration period, the *p-n* junction, and so its capacitor, is charged to a reverse voltage V_0 (less than its breakdown voltage) and then open-circuited. The voltage across the junction, with zero incident illumination, will decay to a value V_1 at a rate that is independent on junction area. When the integration period begins, the rate of decay of charge depends linearly on the intensity of the incident illumination, so that the total charge removed is proportional to the time integral of illumination. The voltage across the junction will decay to a value V_2. At the end of the integration period, the charge remaining in the capacitor is read out and digitised. The output signal will be the difference: $V_1 \quad V_2$. Formally, the voltage across the junction can be expressed in the following way:

$$V_d(t) = V_r e f \quad \frac{1}{C_d} \cdot \int_0^t I_{phot}(u) du \tag{B.8}$$

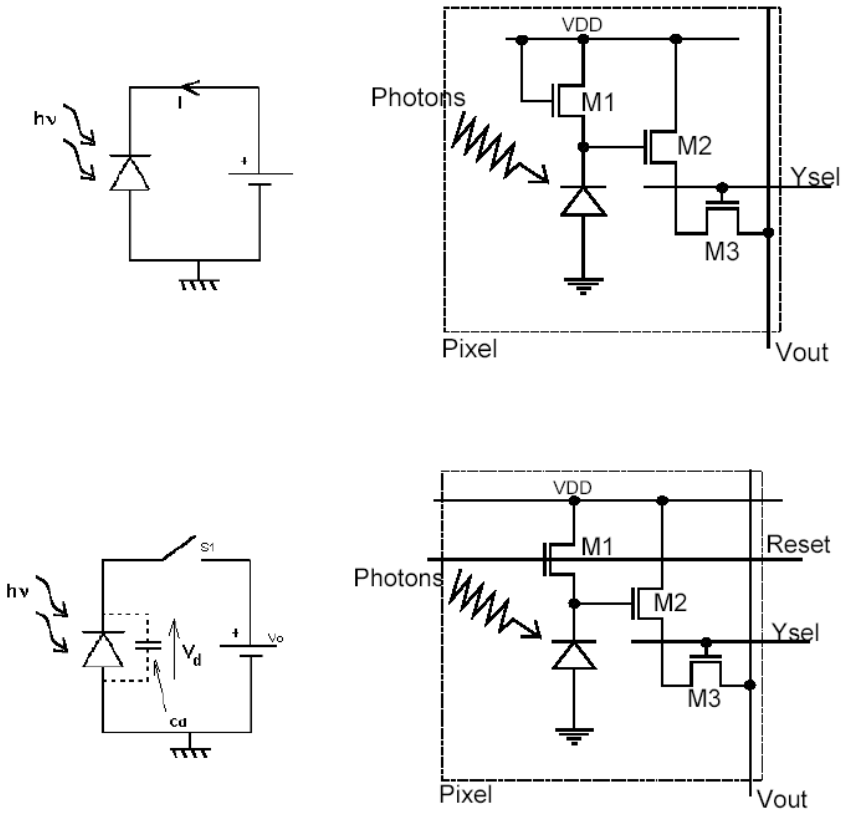

Figure B.9: *Left panels:* idealized circuits for analyzing integration-mode operation (*top*) and current-mode operation (*bottom*) of a p-n junction diode; *right panels:* single pixel structure in both operation modes.

where:
V_d is the voltage across the junction during the integration period;
V_{ref} is the reference voltage, after the photodiode reset;
C_d is the pixel capacitance.
The pixel consists of three transistors as well as a photodetector:
M1 is the transistor acting as a switch to reset the device. When this transistor is turned on, the photodiode is effectively connected to the power supply, V_{dd}, clearing all integrated charge;
M2 is the transistor acting as a buffer (specifically, a source follower), an amplifier which allows the pixel voltage to be observed without removing the accumulated charge. Its power supply is typically tied to the power supply of the reset transistor;
M3 is the row-select transistor. It is a switch that allows a single row of the pixel array to be read by the read-out electronics.

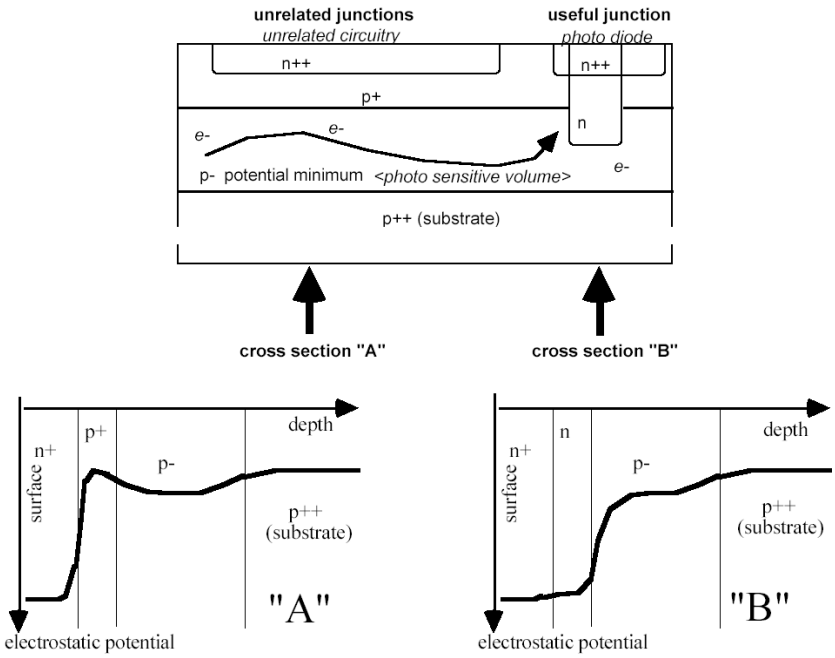

Figure B.10: *Top:* schematic cross section of pixel structure; *Bottom:* electrostatic potential versus depth for cross section "A" (*left panel*) and "B" (*right panel*).

A further advantage of using the integration mode of operation is that, by varying the integration time, the pixel output signal can be maximized for the incident light intensity. This is typically done by limiting the number of completely discharged pixels across the array to lie within a given range. The required frame rate limits the maximum integration time and the minimum is determined by the system clock.

Though the most employed photodetector in a CMOS pixel is the photodiode, photogate detectors are used in some devices as they can offer lower noise through the use of a correlated double sampling. The photogate APS was introduced by JPL in 1993 for high performance scientific imaging and low light applications. A photogate pixel, such as that shown in Fig. B.11, is essentially a single-pixel surface channel CCD imager, which combines CCD benefits and X-Y readout. Its imaging structure consists of a photogate (PG) with a floating diffusion output (FD) separated by a transfer gate (TX). The pixel unit cell also contains a reset transistor (M1), the input transistor of the in-pixel source-follower (M2), and a row selection transistor (M3). During the signal integration period, photo-generated charge is collected under the photogate, which is biased at a higher potential (5V). TG is generally biased at 2V to isolate the collected charge under the photogate from the floating diffusion node. For readout, the floating-diffusion node is reset by using transistor M1 and its resultant voltage is measured by the source follower and stored. Electrons collected under the photogate are then transferred to the FD node via

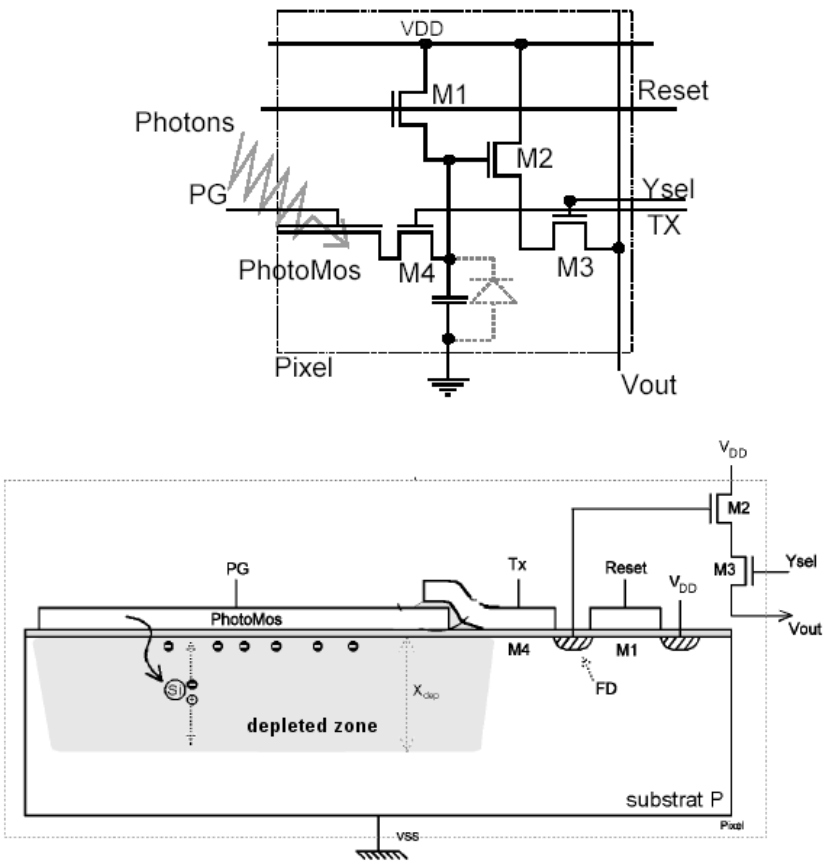

Figure B.11: *Top:* schematic of a CMOS photogate pixel; *Bottom:* cross-section of a CMOS photogate pixel during integration time

device TG by holding PG at ground (0V). The new voltage is then sensed. The difference between the reset level and the signal level is the output of the sensor. A fundamental problem with the photogate pixel is the absorption of incident light, through the polysilicon electrode, before reaching the substrate, reducing the short-wavelength responsivity. Such a problem can be circumvented by backside illumination. A further disadvantage of the photogate pixel is that, in a CMOS process, the transfer of charge between the pixel and floating-diffusion node is not optimized, leading to the introduction of image lag. An important advantage of the photogate pixel is the suppression of the reset noise (KT/C) by the Correlated-Double Sampling.

Appendix C

Selected sensors for the IBIS instrument

C.1 Silicon Imaging SI-1920HD MegaCamera

The SI-1920HD MegaCamera consists of 6 major component sections built on two PC boards (33 x 40mm):
- 2.1 Megapixel CMOS Image Sensor
- Digital Clock Synthesizer
- Digital Control Logic
- Microprocessor
- Dual 12-Bit CameraLink Interface (Base Configuration)
- Camera Control Signals & +5VDC Power

The SI-1920HD MegaCamera utilizes a 2.1 Million pixel high-speed CMOS image sensor. Each pixel is 5 μm square, ideal for image processing, and the array has 1920 pixels on a line and 1080 rows, which result in a 16:9 aspect ratio. Thanks to the CMOS technology, the sensor offers a more responsive pixel design with added circuitry for increased dynamic range, greater sensitivity, decreased fixed pattern noise and low dark current for long exposure applications. Unlike CCDs, which leak charge to adjacent pixels when the registers overflow (bloom), the SI-1920HD provides inherent antiblooming protection in each pixel, so that there is no blooming. The sensor array design is based on a field integration read-out system with line-by-line transfer and an electronic shutter with a synchronous pixel read-out scheme. Other features include subsampling and binning for reduced resolution with a full field of view, RoI (region of interest) for reduced field of view and full resolution and individual gain controls for each pixel to maximize dynamic range.

The analog gain amplifier consists of two stages: one stage that controls the gain of each pixel and one stage for overall analog gain.

Each pixel value is sampled by a Dual 12-Bit Analog-to-digital (A/D) converter and quantized into 4096 levels inside the sensor. The use of a 12-bit converter versus traditional 8-bit system further enhances the image dynamic range.

The Digital Clock Synthesizer allows us to generate a wide range of master

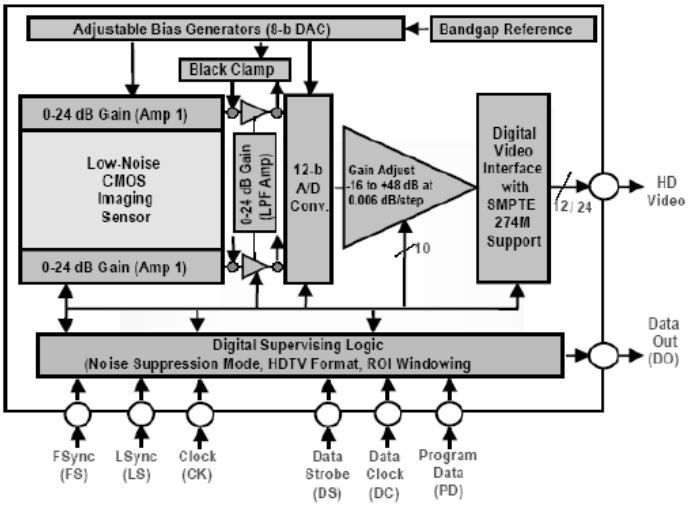

Figure C.1: Block diagram of the SI-1920HD MegaCamera

clock frequencies (e.g. 20 to 75 MHz).

The camera is equipped with a microprocessor which provides the control interface between the PC and the functional block in the camera (Sensor, Clock Synthesizer, Register Memory, Channel Link Interface & Serial port (CameraLink).

Camera Link is a new digital transmission method. It is an easy and standard way to connect digital cameras to frame grabbers providing a data transmission greater than 1.2Gb/sec.

In Table C.1 SI-1920HD MegaCamera characteristics are reported. This camera has been selected mainly for its high frame rate, of order of of 30-300 fps, depending on the selected ROI and on the exposure times. Moreover, its rectangular format (1920 x 1080 pixels) does not provide a gain on the number of pixels, but allows us to record two images (both for Phase Diversity or polarimetric use) on the same sensor. In Fig. C.3 the SI-1920HD MegaCamera Quantum Efficiency is shown. If we compare this curve with that relative to the current IBIS CCD, it is evident that the CMOS sensor shows a better spectral response than the CCD in all IBIS spectral lines apart from the 854.2 nm line (30% for both sensors in this case).

C.2 Andor IXON DV885 EMCCD

Andor IXON DV885 camera uses the electron multiplying CCD (EMCCD) technology. These sensors are manufactured using standard CCD fabrication methods but the unique feature is an electron multiplying structure that is inserted between the end of the shift register and the output amplifier. It enables charges to be multiplied on the sensor before it is read out, while utilizing the full QE performance of the CCD sensor. The EMCCD gain of the camera can be varied from unity up to thousand times directly through the software. An important feature of this camera is the high pixel readout rate, that can be set

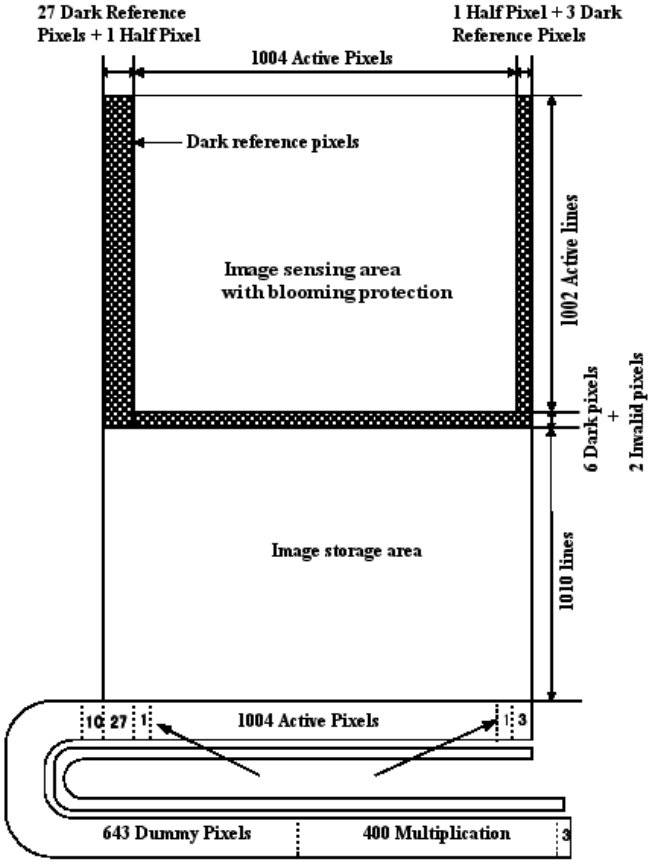

Figure C.2: 1004 × 1002 pixel Impactron CCD image sensor

up to 35MHz. All main characteristics of the camera are shown in Table C.1. In Fig. C.3 the Quantum Efficiency curve is reported. This camera, like the previous one, shows a better spectral response (35%-65%) in the IBIS spectral range than the current CCD. It contains an Impactron Frame Transfer CCD from Texas Instruments. The sensor consists of five basic functional blocks: the image-sensing area, the image-storage area, the serial register, the charge multiplier and the charge detection node with buffer amplifier. The location of each of these blocks is identified in the functional block diagram (Fig. C.2). The image-sensing area of the sensor is made up of 1002 lines with 1004 pixels in each line. 28 columns at the left edge and 4 columns at the right edge of the image-sensing area are shielded from the incident light and reserved for dark reference. Other 6 dark lines, located between the image sensing area and the image-storage area, were added to the array for isolation. The blooming protection is based on an advanced lateral overflow drain concept that drains away from the pixels all electrons that exceed a specific level. The sensor can be operated in the progressive scan mode. The frame transfer from the image sensing area to the memory area is accomplished at a high rate that minimizes image smear. By applying a short positive pulse to the anti-blooming drain all charges

are removed from the image area. In this way it is possible to precisely control the beginning of the integration time. Moreover, the single-pulse clearing capability also reduces smear by eliminating accumulated charge in pixels before the start of the integration period. After charge is integrated and stored in the memory it is available for readout in the next cycle. This is accomplished by using a unique serial register design that includes special charge multiplication pixels.

The serial register, used for transporting charge stored in the pixels of the memory lines to the output amplifier, has twice the standard length. The first half has the conventional design of a CCD sensor. The second half, however, includes 400 charge multiplication stages with a number of dummy pixels used to transport charge between the active register blocks and the output amplifier. Charge is multiplied as it progresses from stage to stage in the multiplier toward the charge detection node.

The last element of the charge detection and readout chain is the charge detection node with the buffer amplifier. The charge detection node uses a standard Floating Diffusion (FD) concept followed by an on-chip dual-stage source-follower buffer.

The camera, based on the EMCCD technology, enables charges to be multiplied on the sensor before it is read out, while utilizing the full QE performance of the CCD sensor.

	PentaMax	**SI1920-HD**	**Andor DV885**
Sensor	CCD	CMOS	EMCCD
Active Pixels	1317 ×1035	1920×1280	1004×1002
Image Area (mm^2)	8.98×7.04	9.68×5.45	8×8
Pixel Size (μm^2)	6.8×6.8	5×5	8×8
Full Well Capacity (e)	45,000	60,000	40,000
Read Noise (e)	∼10e @1MHz	∼15e	<25e @35MHz
Frame Rate	5 fps	30-300 fps	31.5 fps

Table C.1: Comparison between PentaMax, SI-1920HD and Andor DV885

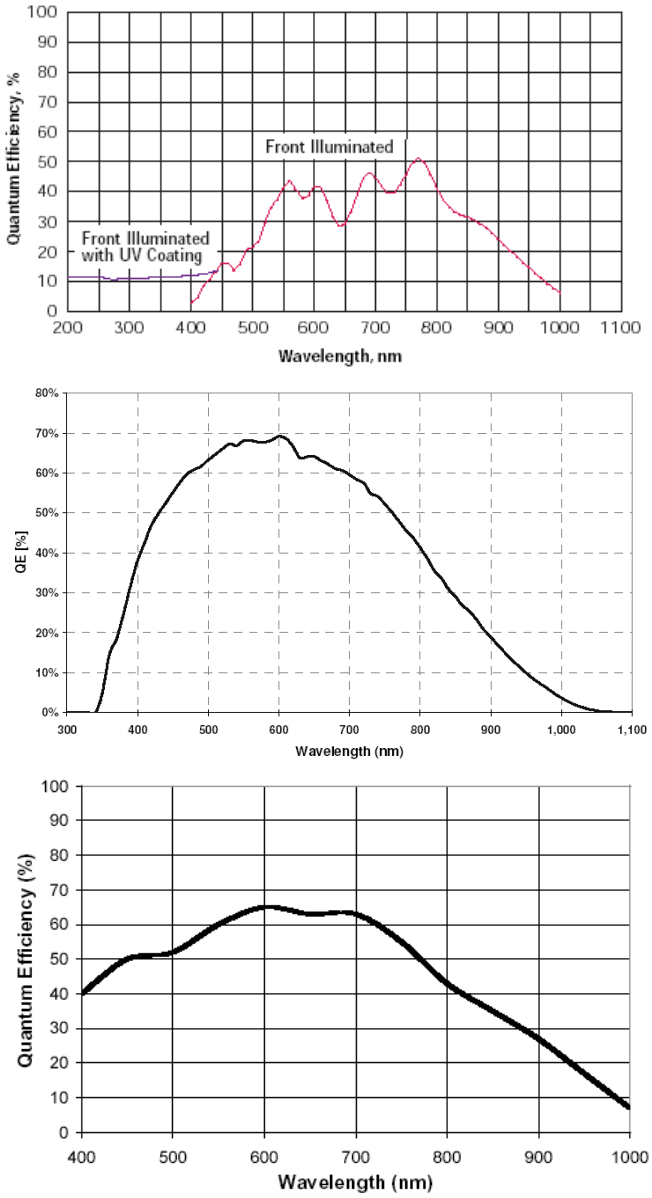

Figure C.3: Quantum Efficiency curves of the KAF-1400 sensor (*top panel*), SI-1920HD MegaCamera (*central panel*) and Andor IXON DV885 EMCCD sensor (*bottom panel*)

Appendix D

IBIS data reduction code

In this appendix we report the main routines of the IBIS data reduction pipeline written in IDL 6.2 in collaboration with Dr. Katja Jannsen. These routines include the correction for CCD non-linearity effects, dark current, gain table and blue shift.

PRO Ibis, new_flat=new_flat, new_gain=new_gain, flat_field

```
common file_path, flat_dir, data_dir, result_dir, dark_dir, blueshift_map, &
vel_dir, data_corrected_dir

common variabili, sequences, flat_sequences, seq_length, flat_seq_length, scan_start,&
scan_end, line_start, line_end, cont_pos, flat_scan_start, flat_scan_end, &
start_seq, flat_line_start, flat_line_end

common variabili1, filter_wavelength, wavelength_step, new_stepwidth, ccd_full_size,&
binning

device, decomposed=0
loadct, 0, /SILENT

;;; ---------- Define COMMON variables----------

  flat_seq_length     = 36      ; Flat Sequence Length
  seq_length          = 36      ; Sequence Length
  flat_scan_start     = 0       ; First spectral point of the scan
  flat_scan_end       = 15      ; Last spectral point of the scan
  flat_line_start     = 3       ; First spectral point of the flat
  flat_line_end       = 12      ; Last spectral point of the flat
  scan_start          = 0       ; the same as flat
  scan_end            = 15      ; the same as flat
  line_start          = 3       ; the same as flat
  line_end            = 12      ; the same as flat
  filter_wavelength   = 7090    ; Integer, in Å
  wavelength_step     = 0.030   ; Original mean stepwidth in Å
  new_stepwidth       = 0.001   ; New interpolation stepwidth in Å
```

```
 ccd_full_size      = 1024    ; Pixels
 binning            = 2
 blueshift_map      = 2
 start_seq          = 0       ; sequence start
;************* WORK DIRECTORY************

 flat_dir               =   'C\'+strtrim(filter_wavelength, 2)+'\flat'\'
 dark_dir               =   'C\'+strtrim(filter_wavelength, 2)+'\dark'\'
 data_dir               =   'C\'+strtrim(filter_wavelength, 2)+'\data'\'
 result_dir             =   'C\'+strtrim(filter_wavelength, 2)+'\result'\'
 data_corrected_dir     =   'C\'+strtrim(filter_wavelength, 2)+'\result+'\scan_correct'\'
 dark_dir               =   'C\'+strtrim(filter_wavelength, 2)+'\dark'\'
 scan_file   =   'scan_'

;;————————— Set Keywords ————————————

 new_flat    =   ;produce averaged flat
 new_gain    =   ;calculate gain, dark and blueshift
 flat_field  =   ;gain, dark and blueshift correction
;;————————————————————————————————-

; — PRODUCE AVERAGED FLAT —

IF KEYWORD_SET(new_flat) THEN ibis_average_flat

;;;*********************************************************

; — CALCULATE GAIN, BLUESHIFT AND DARK CURRENT

IF KEYWORD_SET (new_gain) THEN ibis_make_gain

;;;*********************************************************

; — PREFILTER

IF keyword_set(new_prefilter) THEN ibis_make_prefilter

;*********************************************************

IF KEYWORD_SET (flat_field) THEN BEGIN

    FOR seq_number=start_seq,sequences-1 DO BEGIN

        file = string(scan_file, filter_wavelength, seq_number,&
        format='(a5, i4, "_", i3.3, ".sav")')

;; ————————— Read Data Scan ————————————

        scan_orig = read_ibis_file(seq_number,/linearity)
```

```
;; ———————— Apply Gain and Dark ——————————

        scan1 = ibis_apply_gain(scan_orig)

;; ———————— Prefilter Correction ————————-

scan2 = ibis_apply_prefilter(scan1, blueshifted=0)

;; ————————————Apply Blueshift ———————————

        scan = ibis_apply_blueshift(scan2)

;; ————————————Save Results ———————————

        save, scan, filename=result_dir+file

    ENDFOR
ENDIF

PRINT, '****** END OF PROGRAM **********************'

END


FUNCTION read_ibis_file, seq_num,linearity=linearity

common file_path, flat_dir, data_dir, result_dir, dark_dir, blueshift_map, &
vel_dir, data_corrected_dir

common variabili, sequences, flat_sequences, seq_length, flat_seq_length, scan_start,&
scan_end, line_start, line_end, cont_pos, flat_scan_start, flat_scan_end, &
start_seq, flat_line_start, flat_line_end

common variabili1, filter_wavelength, wavelength_step, new_stepwidth, ccd_full_size,&
binning

xsize=ccd_full_size/binning
ysize=ccd_full_size/binning

first_column=fltarr(10000)
second_column=fltarr(10000)
full_well=4096.0
perc_full_well=fltarr(xsize,ysize)
index=intarr(xsize,ysize)

image_corrected=fltarr(xsize,ysize,seq_length)

images=5000 ;number of images in each subfolder
```

```
all_files=strarr(images)

image=intarr(xsize,ysize,scan_end-scan_start+1)

; ——————- Open images ——————
restore,result_dir+'radial_mask_'+strtrim(filter_wavelength,2)+'.sav'

KK=0
FOR j=scan_start, scan_END DO BEGIN

indice=seq_num*seq_length+j

    file=all_files(indice)

    openr,1,file
    a=assoc(1,intarr(xsize,ysize),2880)
    read_image = a(0)
    image(*,*,KK)=read_image(*,*)
    close,1
    KK=KK+1

ENDFOR

;;;———— Non Linearity Correction ————

FOR k=0,kk-1 DO BEGIN

    IF KEYWORD_SET(linearity) THEN BEGIN

        openr,1,data_dir+\'linearity.correction.curve.txt'

        i=0
        WHILE NOT EOF (1) do begin
            readf,1,aa,bb
            first_column(i)=aa
            second_column(i)=bb
            i=i+1
        ENDWHILE

        close,1


        FOR i=0,xsize-1 DO BEGIN

            FOR j=0,ysize-1 DO BEGIN

                perc_full_well(i,j)=image(i,j,k)/4096.0
                index(i,j)=round(perc_full_well(i,j)/0.001)
                indice=index(i,j)
                image(i,j,k)=image(i,j,k)/second_column(indice)
```

```
        ENDFOR

    ENDFOR

  ENDIF

ENDFOR

return,image

END
```

PRO Ibis_average_flat

```
common file_path, flat_dir, data_dir, result_dir, dark_dir, blueshift_map, &
vel_dir, data_corrected_dir

common variabili, sequences, flat_sequences, seq_length, flat_seq_length, scan_start,&
scan_end, line_start, line_end, cont_pos, flat_scan_start, flat_scan_end, &
start_seq, flat_line_start, flat_line_end

common variabili1, filter_wavelength, wavelength_step, new_stepwidth, ccd_full_size,&
binning

; — Sum up Flatsequences Imagewise —

averaged_flat=fltarr(ccd_full_size/binning, ccd_full_size/binning, &
flat_scan_end-flat_scan_start+1)

file=FINDFILE(flat_dir+'/*.fits')
file=file(sort(file))
count=n_elements(file)

xsize=ccd_full_size/binning
ysize=ccd_full_size/binning

For k=flat_scan_start, flat_scan_end Do Begin
  For i=0, flat_sequences-1 Do Begin

    print, file(k+i*flat_seq_length)

    read_image=read_ibis_flat_file(file(k+i*flat_seq_length),/linearity)

    openw,1,result_dir+'medie_av_flat_'+strtrim(f_w, 2)+'.dat',/append
    media=mean(read_image(xsize/2-50:xsize/2+49, ysize/2-50:ysize/2+49))
    devst=stddev(read_image(xsize/2-50:xsize/2+49, ysize/250:ysize/2+49))
    printf,1,format='(2(i,2x),2(f0,2x))',i,k,media,devst
    close, 1
```

```
        averaged_flat = averaged_flat /(flat_sequences)

    endfor
endfor

save,averaged_flat,filename=result_dir+'averaged_flat_'+wavelength+'.sav'

END



PRO ibis_make_gain

; ********************************************************
; ***** Construct IBIS Gain Table Calibration Matrix *****
; ********************************************************


common file_path, flat_dir, data_dir, result_dir, dark_dir, blueshift_map, &
vel_dir, data_corrected_dir

common variabili, sequences, flat_sequences, seq_length, flat_seq_length, scan_start,&
scan_end, line_start, line_end, cont_pos, flat_scan_start, flat_scan_end, &
start_seq, flat_line_start, flat_line_end

common variabili1, filter_wavelength, wavelength_step, new_stepwidth, ccd_full_size,&
binning

;**********************KEYWORD***************************
  use_radial_mask    =    1
  blueshift          =    1
; ********************************************************
; ***** Perform Initial Flat Sequence Calibrations *****
; ********************************************************

xsize=ccd_full_size/binning
;dimensione originale dell'immagine ysize=ccd_full_size/binning

  all_dark_files     =    findfile (dark_dir+'*.fits')
  n_all_dark_files   =    n_elements (all_dark_files)
  media_dark         =    intarr (n_all_dark_files)
for i=0,n_all_dark_files-1 do begin
    openr,1,all_dark_files(i)
    a=assoc(1,intarr(xsize,ysize),2880)
    dark_image=a(0)
    close,1
    media_dark(i)=mean(dark_image)
endfor
```

```
dark_current=mean(media_dark)

; —— Load (previously) Averaged Flat Field Sequence ——
; (i.e. imagewise sum of all flat fielding sequences)
; no matter the source, corrections for non-linearity and byte order
; should already have been applied to the flat sequence at this point

; —— Determine size of average flat field sequence ——

restore, result_dir+'\averaged_flat_'+strtrim(filter_wavelength,2)+'.sav'

xsize_ave_flats = (size(averaged_flat))(1)
ysize_ave_flats = (size(averaged_flat))(2)
zsize_ave_flats = (size(averaged_flat))(3)

; ********************************************************
; ****************** Create radial mask *****************
; ********************************************************

; (*) This takes the center of the data array as the center of the image.
; We should fit a circle to the circular mask to determine true image
; center and image radius

IF use_radial_mask EQ 1 THEN BEGIN

    image_center = (xsize_ave_flats, ysize_ave_flats)/2.
    image_radius = fix( ((ccd_full_size/2)-ccd_full_size*0.03)/binning)
    radial_dist = radial_distances((1, xsize_ave_flats,ysize_ave_flats), image_center)
    radial_mask = radial_dist LE image_radius

ENDIF

; —— Remove Dark/Bias from Flat Sequence ——
index=where(radial_mask eq 1)
for i=0, zsize_ave_flats-1 DO BEGIN
    averaged_flat(index,i) = averaged_flat(index,i)-dark_current
endfor

save,averaged_flat,filename=result_dir+'no_dark_averaged_flat_'+&
strtrim(filter_wavelength,2)+'.sav'

for i=0,flat_scan_start-flat_scan_end do begin
    averaged_flat(*,*,i) =averaged_flat(*,*,i) * radial_mask(*,*)
endfor

; ——Read original wavelengths ————-

ii=0
openr,1,result_dir+'wavelength_'+strtrim(filter_wavelength,2)+'.txt'
```

```
wavelengths_orig=fltarr(scan_end-scan_start+1)

while not eof(1) do begin
    readf,1,wave
    wavelengths_orig(ii)=wave
    ii=ii+1
endwhile

close,1

; ******************************************************
; ***** Find Blueshift Map for Flat Field Sequence *****
; ******************************************************

;CONSIDERO SOLO LE LUNGHIZZE D'ONDA LUNGO LA RIGA, NO CON-
TINUO

wave_range=wavelengths_orig(line_end-scan_start)-wavelengths_orig(line_start-scan_start)
stepnumber=round(wave_range/new_stepwidth)
wavelengths_new=findgen(stepnumber)*new_stepwidth+wavelengths_orig(line_start-
scan_start)

save,wavelengths_orig, filename = result_dir+ 'wavelengths_orig_' +&
strtrim(filter_wavelength,2)+'.sav'
save, wavelengths_new, filename = result_dir+ 'wavelengths_new_'&
+strtrim(filter_wavelength,2)+'.sav'

IF KEYWORD_SET (blueshift) THEN BEGIN

; — Create a Reference Profile —

    extract_ref = ref(line_start-scan_start:line_end-scan_start)

; — Calculate Line Center Shifts –
    observed_blueshift = FLTARR(xsize_ave_flats, ysize_ave_flats)

    FOR i=0, xsize_ave_flats-1 DO BEGIN
        FOR j=0, ysize_ave_flats-1 DO BEGIN

            IF (radial_mask(i, j) EQ 1) THEN BEGIN

                extract_line =REFORM(averaged_flat(i, j,&
                line_start-scan_start:line_end-scan_start))

                observed_blueshift(i, j)=shc(extract_ref, extract_line,/int)

            ENDIF

        ENDFOR
    ENDFOR
```

```
; — Calculate Angstrom and Find Center of Blueshift —

    observed_blueshift=observed_blueshift*(wave_range/(line_end-line_start))
    observed_blueshift = observed_blueshift - max(observed_blueshift)

;CALCOLO IL CENTRO OTTICO DEL BLUESHIFT E IL BLUESHIFT FIT-
TATO

    optical_center = ibis_optical_center(observed_blueshift,
    mask=radial_mask,blueshift_fitted=blueshift_fitted,blueshift4=blueshift4)


    CASE blueshift_map OF
        '0': blueshift_used = observed_blueshift
        '1': blueshift_used = analytical_ blueshift
        '2': blueshift_used = blueshift_blueshift
    ENDCASE

    analytical_blueshift =ibis_blueshift(filter_wavelength,(xsize_ave_flats, ysize_ave_flats),
    optical_center=optical_center,binning=binning)/ 1000.
    analytical_blueshift=-(analytical_blueshift*radial_mask)

; ****************************************************************
; ***** Construct Unbroadened Mean Flat Field Profile *****
; ***** This contains the global prefilter profile & the lines *****
; ****************************************************************

      flat_start      =   0
      flat_end        =   zsize_ave_flats-1
      wave_range      =   wavelengths_orig(flat_end)-wavelengths_orig(flat_start)
      stepnumber      =   (wave_range / new_stepwidth)
    wavelengths_new = FINDGEN(stepnumber)*new_stepwidth + wavelengths_orig(flat_start)

; — Apply Blueshift to Flatfieldprofiles and Average —

      alignedprofile_flats      =   DBLARR(stepnumber)
      alignedprofile_flats_var  =   DBLARR(stepnumber)
      counter                   =   0L
    FOR i=0, xsize_ave_flats-1 DO BEGIN
        FOR j=0,ysize_ave_flats-1 DO BEGIN

            IF (radial_mask(i,j) EQ 1) THEN BEGIN

                flat_single_spectrum=reform(averaged_flat(i, j, flat_start:flat_end))

                wavelengths_new_blue=wavelengths_new-blueshift_used(i,j)

                flat_spectrum_shifted1=SPL_INIT(wavelengths_orig,flat_single_spectrum)
                flat_spectrum_shifted= SPL_INTERP(wavelengths_orig, flat_single_spectrum,&
```

```
                flat_spectrum_shifted1,& wavelengths_new_blue)

                alignedprofile_flats =alignedprofile_flats + flat_spectrum_shifted

                alignedprofile_flats_var = alignedprofile_flats_var+&
                (flat_spectrum_shifted^2)
                counter = counter + 1
            ENDIF
        ENDFOR
    ENDFOR

; ***************************************************************
; ***** Apply Blueshift to Unbroadened Mean Spectral Profile ***
; ***** =¿ 3D-Array that contains Blueshift, Unbroadened Lines ***
; ***** Global Prefilter Profile, no Gaintable ***
; ***************************************************************

; the flat field mean spectral profile found above will be remapped at
; each point to construct the blueshifted average profile that would be
; expected at each point in a "perfect' system (i.e. no flat field variations)

; — Apply Blueshift to Unbroadened Mean Profile —

shiftedprofile_flats_interp = DBLARR(zsize_ave_flats)

shiftedprofile_flats=DBLARR(xsize_ave_flats, ysize_ave_flats,zsize_ave_flats)

    FOR i=0,xsize_ave_flats-1 DO BEGIN
        FOR j=0,ysize_ave_flats-1 DO BEGIN

            IF (radial_mask(i,j) EQ 1) THEN BEGIN
                wavelengths_orig_with_blue=wavelengths_orig+blueshift_used(i,j)

                shiftedprofile_flats_interp1=SPL_INIT(wavelengths_new,&
                alignedprofile_flats)
                shiftedprofile_flats_interp = SPL_INTERP(wavelengths_new,&
                alignedprofile_flats,shiftedprofile_flats_interp1, wavelengths_orig_with_blue)
                shiftedprofile_flats(i,j,*) = shiftedprofile_flats_interp

            ENDIF

        ENDFOR
    ENDFOR

    save, analytical_blueshift,filename = result_dir+'analytical_blueshift_'+strtrim
    (filter_wavelength,2)+'.sav'

    save, observed_blueshift, filename =result_dir+'observed_blueshift_'+&
    strtrim(filter_wavelength,2)+'.sav'
```

```
ENDIF ELSE BEGIN

 flat_start      =   0
 flat_end        =   zsize_ave_flats-1
 wave_range      =   wavelengths_orig(flat_end)-wavelengths_orig(flat_start)
 stepnumber      =   (wave_range / new_stepwidth)
   wavelengths_new = FINDGEN(stepnumber)*new_stepwidth + wavelengths_orig(flat_start)


; — Apply Blueshift to Flatfieldprofiles and Average —

 alignedprofile_flats       =   DBLARR(stepnumber)
 alignedprofile_flats_var   =   DBLARR(stepnumber)   = 0L
 counter                    =   0L
   FOR i=0, xsize_ave_flats-1 DO BEGIN
      FOR j=0,ysize_ave_flats-1 DO BEGIN

         IF (radial_mask(i,j) EQ 1) THEN BEGIN

            flat_single_spectrum = REFORM(averaged_flat(i,j, flat_line_start&
            -flat_scan_start:flat_line_end-flat_scan_start))

            flat_spectrum_shifted=SPLINE(wavelengths_orig(flat_line_start&
            -flat_scan_start:flat_line_end-flat_scan_start),flat_single_spectrum,&
            wavelengths_new_blue )
            alignedprofile_flats=alignedprofile_flats+ flat_spectrum_shifted
            alignedprofile_flats_var=alignedprofile_flats_var+ (flat_spectrum_shifted^2)
            counter = counter + 1

         ENDIF

      ENDFOR
   ENDFOR

   alignedprofile_flats =alignedprofile_flats/counter
   alignedprofile_flats_var=SQRT(((counter * alignedprofile_flats)-&
   alignedprofile_flats_var)/FLOAT(counter* (counter - 1)))

; ************************************************************
; ***** Apply Blueshift to Unbroadened Mean Spectral Profile ***
; ***** =¿ 3D-Array that contains Blueshift, Unbroadened Lines ***
; ***** Global Prefilter Profile, no Gaintable ***
; ************************************************************
;
; the flat field mean spectral profile found above will be remapped at
; each point to construct the blueshifted average profile that would be
; expected at each point in a "perfect' system (i.e. no flat field variations)

   shiftedprofile_flats_interp = FLTARR(zsize_ave_flats)
   shiftedprofile_flats =FLTARR(xsize_ave_flats, ysize_ave_flats, zsize_ave_flats)
```

```
; — Apply Blueshift to Unbroadened Mean Profile —

    FOR i=0,xsize_ave_flats-1 DO BEGIN
        FOR j=0,ysize_ave_flats-1 DO BEGIN

            IF (radial_mask(i,j) EQ 1) THEN BEGIN

                shiftedprofile_flats_interp=SPLINE( wavelengths_new,&
                alignedprofile_flats, wavelengths_orig)
                shiftedprofile_flats(i,j,*)=shiftedprofile_flats_interp

            ENDIF
        ENDFOR
    ENDFOR

ENDELSE

; — Construct Gain Table —
; by dividing the average flat field sequence by the array of shifted
; mean profiles.

gain_table = averaged_flat / (shiftedprofile_flats ¿1)

;; Save results

save,gain_table,filename=result_dir+'gain_table_'+strtrim(filter_wavelength,2)+'.sav'

save, radial_mask, filename=result_dir+ 'radial_mask_'+ strtrim(filter_wavelength,2)+'.sav'

save,dark_current, filename=result_dir+'dark_current_' +strtrim(filter_wavelength,2)+'.sav'

END


FUNCTION Ibis_apply_gain, image

common file_path, flat_dir, data_dir, result_dir, dark_dir, blueshift_map, &
vel_dir, data_corrected_dir

common variabili, sequences, flat_sequences, seq_length, flat_seq_length, scan_start,&
scan_end, line_start, line_end, cont_pos, flat_scan_start, flat_scan_end, &
start_seq, flat_line_start, flat_line_end

common variabili1, filter_wavelength, wavelength_step, new_stepwidth, ccd_full_size,&
binning

common variabili1, filter_wavelength, wavelength_step, new_stepwidth, ccd_full_size,binning

restore, result_dir+'dark_current_'+ strtrim(filter_wavelength,2)+ '.sav'
```

```
restore, result_dir+'gain_table_'+strtrim(filter_wavelength,2)+ '.sav'
restore, result_dir+'radial_mask_'+strtrim(filter_wavelength,2)+ '.sav'

xsize = (size(image))(1)
ysize = (size(image))(2)
zsize = (size(image))(3)

;; — Apply Gain and Dark —

image1=fltarr(xsize,ysize,zsize)

FOR i=0, zsize-1 DO BEGIN

;; Define temporary 2d-images, in order to use where

    data_image = image(*, *, i);+line_start-scan_start)
    gain_image = gain_table(*, *, i)

;; Subtract Dark, Avoid negative Datavalues

    data_image = data_image - dark_current
    data_image = data_image ¿ 0

;; Use Gaintable for pixels, that it exists for, Cut the rest

    index = where(radial_mask EQ 1)

    data_image(index) = data_image(index) / gain_image(index)
    data_image = data_image * radial_mask

    image1(*, *, i) = data_image

ENDFOR

return, image1
```

END

PRO ibis_make_prefilter

```
common prefilter_path,data,result_dir
common prefilter_var,seq_length,scan_start,scan_end,x_start,x_end,y_start,y_end,&
line1_start,line1_end,line2_start,line2_end,line3_start,line3_end,line4_start,line4_end,&
line5_start,line5_end ,profile_start,profile_end,wavelength_pref

common prefilter_path,data,result_dir

common variabili1,filter_wavelength,wavelength_step,new_stepwidth,&
ccd_full_size,binning,xnew_size,ynew_size
```

```
;********************************** SET PARAMETERS ***************************
IF filter_wavelength EQ 7090 THEN BEGIN
  seq_length     =   97
  scan_start     =   0
  scan_end       =   96
  x_start        =   0
  x_end          =   511
  y_start        =   0
  y_end          =   511
  line1_start    =   20
  line1_end      =   27
  line2_start    =   35
  line2_end      =   39
  line3_start    =   40
  line3_end      =   66
  line4_start    =   77
  line4_end      =   84
  line5_start    =   87
  line5_end      =   92
  profile_start  =   0
  profile_end    =   96
  binning        =   2
  verbose        =   1
ENDIF ELSE IF filter_wavelength EQ 7224 THEN BEGIN


  seq_length     =   95
  scan_start     =   0
  scan_end       =   94
  x_start        =   0
  x_end          =   511
  y_start        =   0
  y_end          =   511
  line1_start    =   7
  line1_end      =   30
  line2_start    =   32
  line2_end      =   38
  line3_start    =   40
  line3_end      =   50
  line4_start    =   53
  line4_end      =   58
  line5_start    =   60
  line5_end      =   68
  profile_start  =   2
  profile_end    =   94
  binning        =   2
  verbose        =   1
ENDIF ELSE BEGIN
```

```
  seq_length     =   107
  scan_start     =   0
  scan_end       =   106
  x_start        =   0
  x_end          =   = 511
  y_start        =   0
  y_end          =   511
  line1_start    =   17
  line1_end      =   96
  line2_start    =   97
  line2_end      =   98
  line3_start    =   100
  line3_end      =   101
  line4_start    =   102
  line4_end      =   103
  line5_start    =   104
  line5_end      =   105
  profile_start  =   0
  profile_end    =   106
  binning        =   2
  verbose        =   1
ENDELSE
;*****************************************************************************

x_start = x_start/binning ;as both are integer, results directly an integer (no
half values)
x_end = x_end/binning
y_start = y_start/binning
y_end = y_end/binning

xsize = x_end - x_start+1
ysize = y_end - y_start+1

;;Read wavelengths

ii=0
openr,1,result_dir+'\'wavelength_pref_'+strtrim(filter_wavelength,2)+'.dat'

wavelengths_pref=fltarr(scan_end-scan_start+1)

while not eof(1) do begin
    readf,1,wave
    wavelengths_pref(ii)=wave
    ii=ii+1
endwhile

close,1

;; Open Prefilter Scan and Wavelengths
```

```
prefilter_scan = ibis_open_pref(0)


;; Get Radial Mask

restore, result_dir+'radial_mask_'+strtrim(filter_wavelength,2)+'.sav'
restore, result_dir+'fitted_blueshift_'+strtrim(filter_wavelength,2)+'.sav'


;; Create Unbroadened Prefilter Profile from 3D Prefilter Scan
; Apply Blueshift to All profiles and Average Them

profile_pref = dblarr(seq_length)
counter = 0L

FOR i=0, xsize-1 DO BEGIN
    FOR j=0, ysize-1 DO BEGIN

        IF (radial_mask(i,j) EQ 1) THEN BEGIN

            profile = reform(prefilter_scan(i, j, *))

            wavelengths_old = wavelengths_pref +blueshift_fitted(i, j)
            wavelengths_new = wavelengths_pref

            interpol_profile=spline(wavelengths_old,profile,wavelengths_new)
            profile_pref = profile_pref + interpol_profile

            counter = counter + 1

        ENDIF

    ENDFOR
    ENDFOR

profile_pref = profile_pref/ counter


    ;; Cut spectral lines out of prefilter profile

cutprofile=(profile_pref(profile_start:line1_start),profile_pref(line1_end:line2_start),&
            profile_pref(line2_end:line3_start),profile_pref(line3_end:line4_start),&
            profile_pref(line4_end:line5_start),profile_pref(line5_end:profile_end))

cutwavelengths = (wavelengths_pref(profile_start:line1_start),&
            wavelengths_pref(line1_end:line2_start), &
            wavelengths_pref(line2_end:line3_start), &
            wavelengths_pref(line3_end:line4_start), &
            wavelengths_pref(line4_end:line5_start), &
            wavelengths_pref(line5_end:profile_end))
```

```
;; Interpolate Polynominal of 4th Degree to Prefilter

coeff = poly_fit(cutwavelengths, cutprofile, 4, /double)


;; Calculate Fit just to show it, not used elsewhere

prefilter_fit=coeff(0)+coeff(1)*wavelengths_pref+coeff(2)*wavelengths_pref^2+&
coeff(3)*wavelengths_pref^3+ coeff(4)*wavelengths_pref^4

;; Interpolate Prefilter for the Data Wavelengths

restore, result_dir+'wavelengths_orig_'+strtrim(filter_wavelength,2)+'.sav'

xsize = (size(blueshift_fitted))(1)
ysize = (size(blueshift_fitted))(2)
zsize = n_elements(wavelengths_orig)

prefilter_cube = fltarr(xsize, ysize, zsize)
FOR x=0, xsize-1 DO BEGIN
    FOR y=0, ysize-1 DO BEGIN
        wavelengths_xy = wavelengths_orig + blueshift_fitted(x, y)

        prefilter_cube(x, y, *) = coeff(0) + coeff(1)*wavelengths_xy+&
        coeff(2)*wavelengths_xy^2+coeff(3)*wavelengths_xy^3+ coeff(4)*wavelengths_xy^4

    ENDFOR
ENDFOR


;; Normalize Prefilter

prefilter_cube = prefilter_cube / max(prefilter_cube)


;; Save Prefilter

save, prefilter_cube, file=result_dir+'prefilter_cube.sav'
print, 'Wrote '+result_dir+'prefilter_cube.sav'
```

END

FUNCTION ibis_apply_prefilter, scan, blueshifted=blueshifted

```
common prefilter_path,data,result_dir
common prefilter_var,seq_length,scan_start,scan_end,x_start,x_end,y_start,y_end,&
line1_start,line1_end,line2_start,line2_end,line3_start,line3_end,line4_start,line4_end,&
```

```
line5_start,line5_end ,profile_start,profile_end,wavelength_pref

common prefilter_path,data,result_dir

common variabili1,filter_wavelength,wavelength_step,new_stepwidth, &
ccd_full_size,binning,xnew_size,ynew_size

IF n_params( ) LT 1 THEN BEGIN
    print, 'Usage: scan=ibis_apply_prefilter(scan,blueshifted=0/1)'
    return, -1
ENDIF

restore, result_dir + 'prefilter_cube.sav'
restore, result_dir + 'fitted_blueshift_'+strtrim(filter_wavelength,2)+'.sav'

xsize = (size(scan))(1)
ysize = (size(scan))(2)
zsize = (size(scan))(3)

IF keyword_set(blueshifted) THEN &
    print, 'Applying prefilter to already blueshifted scan' &
ELSE &
    print, 'Applying prefilter to not blueshifted scan'

unshifted_prefilter_profile = prefilter_cube(xsize/2, ysize/2, *)

FOR x=0, xsize-1 DO BEGIN
    FOR y=0, ysize-1 DO BEGIN

        IF keyword_set(blueshifted) THEN &
            scan(x, y, *) = scan(x, y, *) / unshifted_prefilter_profile &
        ELSE &
            scan(x, y, *) = scan(x, y, *) / prefilter_cube(x, y, *)

    ENDFOR
ENDFOR


return, scan
```

END

FUNCTION Ibis_apply_blueshift, image

```
common file_path, flat_dir, data_dir, result_dir, dark_dir, blueshift_map, &
vel_dir, data_corrected_dir

common variabili, sequences, flat_sequences, seq_length, flat_seq_length, scan_start,&
scan_end, line_start, line_end, cont_pos, flat_scan_start, flat_scan_end, &
```

```
start_seq, flat_line_start, flat_line_end

common variabili1, filter_wavelength, wavelength_step, new_stepwidth, ccd_full_size,
&
binning

restore,result_dir+'radial_mask_'+strtrim(filter_wavelength,2)+ '.sav'
restore,result_dir+'wavelengths_orig_'+strtrim(filter_wavelength,2)+ '.sav'
restore, result_dir+'wavelengths_new_'+strtrim(filter_wavelength,2)+ '.sav'

restore, result_dir+'fitted_blueshift_'+ strtrim(filter_wavelength,2)+'.sav'

xsize = (size(image))(1)
ysize = (size(image))(2)
zsize = (size(image))(3)

;; — Apply Blueshift —

image1=fltarr(xsize,ysize,line_end-line_start+1)
image1(*,*,0:line_end-line_start)=image(*,*,line_start-scan_start: line_end-scan_start)

;; — Blueshift correction with mean original stepwidth —

shiftmap =(blueshift_used/wavelength_step)

FOR x=0, xsize-1 DO BEGIN ; use the full line
    FOR y=0, ysize-1 DO BEGIN

        IF radial_mask(x, y) EQ 1 THEN BEGIN
            image1(x, y, *)=frac_shift(reform(image1(x, y, *)),shiftmap(x, y))

        ENDIF
    ENDFOR

ENDFOR

scan_wavelengths = wavelengths_orig

;; — Save Wavelengths Vector and Return Shifted Scan —

save, scan_wavelengths, filename=resul_dir+'scan_wavelength_'+strtrim(filter_wavelength,2)+'.sav'

image(*,*,line_start-scan_start:line_end-scan_start)=image1(*,*,*)

return, image

END
```

Bibliography

Aikio, J. and Mähönen, P. (1998). A Simple Void-searching Algorithm. *Astrophysical Journal*, 497:534.

Aiouaz, T., Peter, H., Keppens, R. (2005). Forward modeling of coronal funnels. *Astronomy and Astrophysics*, 442:L35–L38.

Beckers, J. M. and Tallant, P. E. (1969). Chromospheric Inhomogeneities in Sunspot Umbrae. *Solar Physics*, 7:351–365.

Beckers, J. M. and Schröter, E. H. (1969). The Intensity, Velocity and Magnetic Structure of a Sunspot Region. IV: Properties of a Unipolar Sunspot. *Solar Physics*, 2:384–403.

Beckers, J. M. and Schultz, R. B. (1972). Oscillatory Motions in Sunspots. *Solar Physics*, 27:61–70.

Beckers, J. M. and Milkey, R. W. (1975). The line response function of stellar atmospheres and the effective depth of line formation. *Solar Physics*, 43:289292.

Beckers, J. M. (1998). On the effect of narrow-band filters on the diffraction limited resolution of astronomical telescopes. *Astronomy and Astrophysics Supplement*, 129:191–194.

Bel, N. and Leroy, B. (1977). Analytical Study of Magnetoacoustic Gravity Waves. *Astronomy and Astrophysics*, 55:239.

Bellot Rubio, L. R., Balthasar, H., Collados, M. (2004). Two magnetic components in sunspot penumbrae. *Astronomy and Astrophysics*, 427:319–334.

Bendlin, C., Volkmer, R., Kneer, F. (1992). A new instrument for high resolution, two-dimensional solar spectroscopy. *Astronomy and Astrophysics*, 257:817–823.

Bendlin, C. and Volkmer, R., (1995). The two-dimensional spectrometer in the German Vacuum Tower Telescope/Tenerife. From observations to results. *Astronomy and Astrophysics Supplement*, 112:371.

Bercik, D. J., Basu, S., Georgobiani, D., Nordlund, Å, Stein, R. F. (1998). Solar Magneto-Convection. *in ASP Conf. Ser. 154, The Tenth CambridgeWorkshop on Cool Stars, Stellar Systems and the Sun, ed. R. A. Donahue & J. A. Bookbinder, (San Francisco: ASP), CD-568.*

Berger, T. E., and Berdyugyna, S.V., (2003). The Observation of Sunspot Light-Bridge Structure and Dynamics. *Astrophysical Journal*, 589:L117-L121.

Berger, T. E., Schrijver, C. J., Shine, R. A., Tarbell, T. D., Title, A. M. and Scharmer, G. (1995). New Observations of Subarcsecond Photospheric Bright Points. *Astrophysical Journal*, 454:531.

Berger, T. E. (1996). Observation and Analysis of Small-scale Solar Magnetic Structure. *Bulletin of the American Astronomical Society*, 28:869.

Berger, T. E., Löfdahl, M. G., Shine, R. S. and Title, A. M. (1998). Measurements of Solar Magnetic Element Dispersal. *Astrophysical Journal*, 495:973.

Berger, T. E. and Title, A. M. (2001). On the Relation of G-Band Bright Points to the Photospheric Magnetic Field. *Astrophysical Journal*, 553:449469.

Berrilli, F, Florio, A., Ermolli, I. (1997). On the geometrical properties of the chromospheric network. *Solar Physics*, 180:29.

Berrilli, F., Consolini, G., Florio, A., Pietropaolo G. (2001). Solar granulation: properties of velocity fields from THEMIS-IPM observations. *Memorie della Societa Astronomica Italiana*, 72:669-672.

Berrilli, F., Consolini, G., Pietropaolo, E., Caccin, B., Penza, V. and Lepreti, F. (2002). 2-D multiline spectroscopy of the solar photosphere. *Astronomy and Astrophysics*, 381:253–264.

Berrilli, F., Del Moro, D., Russo, S., Consolini, G., Straus, T. (2005). Spatial Clustering of Photospheric Structures. *Astrophysical Journal*, 632:677–683.

Beynon, J. D. E. and Lamb, D. R. (1980). Charge-coupled devices and their applications. *McGraw-Hill Book Company (UK) Limited, Maidenhead, Berkshire, England*.

Bharti, L., Rimmele, T., Jain, R., Jaaffrey, S. N. A., Smartt, R. N. (2007). Detection of opposite polarities in a sunspot light bridge: evidence of low-altitude magnetic reconnection. *Monthly Notices of the Royal Astronomical Society*, 376:1291–1295.

Bharti, L. Joshi, C., Jaaffrey, S. N. A. (2007). Observations of Dark Lanes in Umbral Fine Structure from the Hinode Solar Optical Telescope: Evidence for Magnetoconvection. *Astrophysical Journal*, 669:L57–L60.

Bharti, L., Jain, R., Jaaffrey, S. N. A. (2007). Evidence for Magnetoconvection in Sunspot Umbral Dots. *Astrophysical Journal*, 665:L79–L82.

Bhatnagar, A. and Tanaka, K. (1972). Intensity Oscillation in Ha-Fine Structure. *Solar Physics*, 24:87–97.

Bhatnagar, A., Livingston, W. C., Harvey, J. W. (1972). Observations of Sunspot Umbral Velocity Oscillations. *Solar Physics*, 27:80–88.

Bianda, M., Stenflo, J. O., Solanki, S. K. (1999). Hanle effect observations with the CA BT I 4227 line. *Astronomy and Astrophysics*, 350:1060–1070.

Bogdan, T. J. (2000). Sunspot Oscillations: A Review. *Solar Physics*, 192:373–394.

Bogdan, T. J., Carlsson, M., Hansteen, V. H., McMurry, A., Rosenthal, C. S., Johnson, M., Petty-Powell, S., Zita, E. J., Stein, R. F., McIntosh, S. W., Nordlund, Å. (2003). Waves in the Magnetized Solar Atmosphere. II. Waves from Localized Sources in Magnetic Flux Concentrations. *The Astrophysical Journal*, 599:626–660.

Bogdan, T. J., Judge, P. G. (2006). Observational aspects of sunspot oscillations. *Philosophical Transactions of the Royal Society Series A*, 364:313–331.

Bonet, J. A., Sobotka, M., Vazquez, M. (1995). Photometry of sunspot pores from partial eclipse observations. *Astronomy and Astrophysics*, 296:241.

Borrero, J. M., Lagg, A., Solanki, S. K., Collados, M. (2005). On the fine structure of sunspot penumbrae. II. The nature of the Evershed flow. *Astronomy and Astrophysics*, 436:333–345.

Brants, J. J., and Zwaan, C. (1982). The structure of sunspots. IV - Magnetic field strengths in small sunspots and pores. *Solar Physics*, 80:251–258.

Bray, R. J. ,& Loughhead, R. E. (1964). Sunspots. *The International Astrophysics Series, London: Chapman & Hall, 1964.*

Buil, C. (1991). CCD Astronomy: Construction and Use of an Astronomical CCD Camera. *Willmann-Bell.*

Caccin, B., Gomez, M. T., Marmolino, C., and Severino, G. (1977). Response functions and contribution functions of photospheric lines. *Astronomy and Astrophysics*, 54:227–231.

Cally, P. S. (2006). Dispersion relations, rays and ray splitting in magnetohelioseismology. *Royal Society of London Transactions Series A*, 364:333–349.

Cameron, R., Schüssler, M., Vögler, A. and Zakharov, V. (2007). Radiative magnetohydrodynamic simulations of solar pores. *Astronomy and Astrophysics*, 474:261–272.

Canfield, R. C. and Mehltretter, J. P. (1973). Fluctuations of Brightness and Vertical Velocity at Various Heights in the Photosphere. *Solar Physics*, 33:33.

Canfield, R. C. and Stencel, R. E. (1976). Emission lines in the wings of CA II H and K. I - Initial solar observations and implications. *Astrophysical Journal*, 209:618620.

Canfield, R. C. (1976). The height variation of granular and oscillatory velocities. *Solar Physics*, 50:239-254.

Carlsson, M.; Stein, R. F. (1997). Chromospheric Dynamics - What Can Be Learnt from Numerical Simulations. *Proceedings of the 8th European Meeting on Solar Physics Held at Halkidiki*, 489:159.

Cattaneo, F. (1999). On the Origin of Magnetic Fields in the Quiet Photosphere. *Astrophysical Journal*, 515:L39–L42.

Cattaneo, F., Lenz, D., and Weiss, N. (2001). On the Origin of the Solar Mesogranulation. *IEEE Trandactions on Electron Devices ED-30*, No.6, 694-699.

Cavallini, F. (1998). The Italian Panoramic Monochromator. *Astronomy and Astrophysics Supplement*, 128:589–598.

Cavallini, F. (2006). IBIS: a new post-focus instrument for solar imaging spectroscopy. *Solar Physics*, 236:415 .

Chandrasekhar, S. (1961). *Hydrodynamic and hydromagnetic stability*. International Series of Monographs on Physics, Oxford: Clarendon.

Choudhuri, A. R. (1986). The dynamics of magnetically trapped fluids. I. Implications for umbral dots and penumbral grains. *Astrophysical Journal*, 302:809–825.

Choudhuri, A. R. (1992). The cluster model of sunspots. *In: Sunspots: Theory and observations; Proceedings of the NATO Advanced Research Workshop on the Theory of Sunspots, Cambridge, United Kingdomp*, 243–257.

Cowling, T. G. (1957). Magnetohydrodynamics. *New York: Interscience*.

Cubasch, U. and Voss, R. (2000). The Influence of Total Solar Irradiance on Climate. *Space Science Reviews*, 94:185–198.

de Boer, C. R., Kneer, F., Nesis, A. (1992). Speckle observations of solar granulation. *Astronomy and Astrophysics*, 257:L4–L6.

Degenhardt, D. and Lites, B. W. (1993). The Magnetohydrodynamics of Umbral Flux Tubes. II. Spectroscopic Properties. *Astrophysical Journal*, 416:875.

Deinzer, W., Hensler, G., Schüssler, M., Weisshaar, E. (1984). Model Calculations of Magnetic Flux Tubes - Part Two - Stationary Results for Solar Magnetic Elements. *Astronomy and Astrophysics*, 139:435.

De Pontieu, B.; Erdĺyi, R., James, S. P. (2004). Solar chromospheric spicules from the leakage of photospheric oscillations and flows. *Nature*, 430:536–539.

De Rosa, M., Duvall, T. L., and Toomre, J. (2000). Near-Surface Flow Fields Deduced Using Correlation Tracking and Time-Distance Analyses. *Solar Physics*, 192:351–361.

Deubner, F. L. (1971). Some Properties of Velocity Fields in the Solar Photosphere. III: Oscillatory and Supergranular Motions as a Function of Height. *Solar Physics*, 17:6.

Deubner, F. L. (1975). Observations of low wavenumber nonradial eigenmodes of the sun. *Astronomy and Astrophysics*, 44:371–375.

Deubner, F. L. and Gough, D. (1984). Helioseismology: Oscillations as a Daignostic of the Solar Interior. *Annual review of astronomy and astrophysics*, 22:593–619.

Domínguez Cerdeña, I., Kneer, F., Sánchez Almeida, J. (2003). Quiet-Sun Magnetic Fields at High Spatial Resolution. *Astrophysical Journal*, 582:L55–L58.

Duvall, T. L. J., D'Silva, S., Jefferies, S. M., Harvey, J. W., Schou, J. (1996). Downflows Under Sunspots Detected by Helioseismic Tomography. *Nature*, 379:235.

Einasto, J., Einasto, M., Gramann, M. (1989). Structure and formation of superclusters. IX - Self-similarity of voids. *Monthly Notices of the Royal Astronomical Society*, 238,:155–177.

El-Ad, H., Piran, T., da Costa, L. N. (1996). Automated Detection of Voids in Redshift Surveys. *Astrophysical Journal Letters*, 462:L13.

El-Ad, H. and Piran, T. (1997). Voids in the Large-Scale Structure. *Astrophysical Journal*, 491:421.

Emonet, T. and Cattaneo, F. (2001). Small-Scale Photospheric Fields: Observational Evidence and Numerical Simulations. *Astrophysical Journal*, 560:L197-L200.

Furusawa, K. and Sakai, J. I. (2000). Simulation of the Collision of Magnetic Flux Tubes in the Quiet Solar Photosphere. *Astrophysical Journal*, 540:1156–1171.

Gabriel, A. H. (1976). A magnetic model of the solar transition region. *Philosophical Transactions*, 281:339–352.

Galloway, D. J., Proctor, M. R. E., and Weiss, N. O. (1977). Formation of intense magnetic fields near the surface of the sun. *Nature*, 266:686–689.

Garcia de La Rosa, J. I. (1987). Umbral dots - A case of penetrative convection between sunspot fragments. *Solar Physics*, 112:49–58.

Giovanelli, R. G. (1972). Oscillations and Waves in a Sunspot. *Solar Physics*, 27:71–79.

Giovanelli, R. G. (1974). Waves and Oscillations in the Chromosphere in Active and Quiet Regions. *Chromospheric Fine Structure: Proceedings from IAU Symposium*, 137.

Giovanelli, R. G. (1980). The supergranule velocity field. *Solar Physics*, 67:211–228.

Gough, D. and Toomre, J. (1991). Seismic observations of the solar interior. *Annual Review of Astronomy and Astrophysics*, 29:627–685.

Graham, E. (1977). Compressible convection. *Problems of Stellar Convection (Berlin: Springer)*, 71:151–155.

Grossmann-Doerth, U., Keller, C. U., Schüssler, M. (1996). Observations of the quiet Sun's magnetic field. *Astronomy and Astrophysics*, 315:610–617.

Gurman, J. B. and Leibacher, J. W. (1984). Linear models of acoustic waves in sunspot umbrae. *In ESA The Hydromagnetics of the Sun*, 205–206.

Hagenaar, H. J., Schrijver, C. J., and Title, A. M. (1997). The Distribution of Cell Sizes of the Solar Chromospheric Network. *Astrophysical Journal*, 481:988.

Hansteen, V. H., De Pontieu, B., Rouppe van der Voort, L., van Noort, M., Carlsson, M. (2006). Dynamic Fibrils Are Driven by Magnetoacoustic Shocks. *Astrophysical Journal*, 647:L73–L76.

Hart, A. B. (1954). Motions in the Sun at the photospheric level. IV. The equatorial rotation and possible velocity fields in the photosphere. *Monthly Notices of the Royal Astronomical Society*, 114:17.

Hart, A. B. (1956). Motions in the Sun at the photospheric level. VI. Large-scale motions in the equatorial region. *Monthly Notices of the Royal Astronomical Society*, 116:38.

Hathaway, D. H., Beck, J. G., Han, S., and Raymond, J. (2002). Radial Flows in Supergranules. *Solar Physics*, 205:25–38.

Heinemann, T., Nordlund, Å., Scharmer, G. B., Spruit, H. C. (2007). MHD Simulations of Penumbra Fine Structure. *Astrophysical Journal*, 669:1390–1394.

Herschel, W. (1801). Observations Tending to Investigate the Nature of the Sun, in Order to Find the Causes or Symptoms of Its Variable Emission of Light and Heat; With Remarks on the Use That May Possibly Be Drawn from Solar Observations. *Philosophical Transaction Royal Society of London*, 91:265.

Hirzberger, J., Vazquez, M., Bonet, J. A., Hanslmeier, A. and Sobotka, M. (1997). Time Series of Solar Granulation Images. I. Differences between Small and Large Granules in Quiet Regions. *Astrophysical Journal*, 480:406.

Hirzberger, J., Bonet, J. A., Sobotka, M., Vaẋquez, M., Hanslmeier, A. (2002). Fine structure and dynamics in a light bridge inside a solar pore. *Astronomy and Astrophysics*, 383:275–282.

Hirzberger, J. (2003). Imaging spectroscopy of solar pores. *Astronomy and Astrophysics*, 405:331-340.

Hurlburt, N. E., Toomre, J., Massaguer, J. M. (1984). Two-dimensional compressible convection extending over multiple scale heights. *Astrophysical Journal*, 282:557-573.

Hurlburt, N. E. and Toomre, J. (1988). Magnetic fields interacting with nonlinear compressible convection. *Astrophysical Journal*, 327:920–932.

Hulburt, N. E. and Rucklidge, A. M. (2000). Development of structure in pores and sunspots: flows around axisymmetric magnetic flux tubes. *Monthly Notices of the Royal Astronomical Society*, 314:793–806.

Janesick J. R. (2001). Scientific Charge-Coupled Devices. *SPIE press monograph, Bellingham Washington.*

Janssen, K. and Cauzzi, G., (2006). Dynamics of the solar photosphere with IBIS. I. Reversed intensity structure in the mid-photosphere. *Astronomy and Astrophysics*, 450:365–374.

Jefferies, S. M., Pomerantz, M. A., Duvall, T. L. J., Harvey, J. W., Jaksha, D. B. (1988). Helioseismology from the South Pole: Comparison of 1987 and 1981 results. *Seismology of the Sun and Sun-Like Stars*, 279–284.

Jefferies, S. M., McIntosh, S. W., Armstrong, J. D., Bogdan, T. J., Cacciani, A., Fleck, B. (2006). Magnetoacoustic Portals and the Basal Heating of the Solar Chromosphere. *Astrophysical Journal*, 648:L151–L155.

Jurĉák, J., Mártinez Pillet, V. and Sobotka, M. (2006). The magnetic canopy above light bridges. *Astronomy and Astrophysics*, 453:1079–1088.

Kauffmann, G. and Fairall, A. P. (1991). Voids in the distribution of galaxies - an assessment of their significance and derivation of a void spectrum. *Monthly Notices of the Royal Astronomical Society*, 248:313–324.

Keil, S. L., Balasubramanian, K. S., Smaldone, L. A., Reger, B. (1999). Velocities in Solar Pores. *Astrophysical Journal*, 510:422–443.

Keppens, R. and Mŕtinez Pillet, V. (1996). The magnetic structure of pores and sunspots derived from Advanced Stokes Polarimeter data. *Astronomy and Astrophysics*, 316:229–242.

Keppens, R. (2000). Sunspot Pores. *Encyclopedia of Astronomy and Astrophysics, Edited by Paul Murdin, article 2043. Bristol: Institute of Physics Publishing, 2001.*

Khomenko, E. V., Collados, M., Solanki, S. K., Lagg, A., Trujillo Bueno, J. (2003). Quiet-Sun inter-network magnetic fields observed in the infrared. *Astronomy and Astrophysics*, 408:1115–1135.

Knölker, M. and Schüssler, M. (1988). Model calculations of magnetic flux tubes. IV - Convective energy transport and the nature of intermediate size flux concentrations. *Astronomy and Astrophysics*, 202:275–283.

Kobanov, N. I., Makarchik, D. V. (2004). Propagating waves in the sunspot umbra chromosphere. *Astronomy and Astrophysics*, 424:671–675.

Kobanov, N. I., Kolobov, D. Y., Makarchik, D. V. (2006). Umbral Three-Minute Oscillations and Running Penumbral Waves. *Solar Physics*, 238:231–244.

Koschinsky, M., Kneer, F., Hirzberger, J. (2001). Speckle spectro-polarimetry of solar magnetic structures. *Astronomy and Astrophysics*, 365:588–597.

Krieg, J., Kneer, F., Koschinsky, M., and Ritter, C. (2000). Granular velocities of the Sun from speckle interferometry. *Astronomy and Astrophysics*, 360:1157–1162.

Kurucz, R. L., Furenlid, I., Branult, J. and Testerman, L. (1985). Book-Review - Solar Flux Atlas from 296 TO 1300-NM. *Sky and Telescope*, 70:38.

Kurucz, R. L. (1994). *CD-ROM*, No. 19.

Lamb, H. (1908). *Proc. London Math. Soc. Ser.*, 41, 7:122

Lawrence, J. K., Cadavid, A. C., Ruzmaikin, A. A. (1999). Characteristic Scales of Photospheric Flows and Their Magnetic and Temperature Markers. *Astrophysical Journal*, 513:506–515.

Leibacher, J. W. and Stein, R. F. (1971). A New Description of the Solar Five-Minute Oscillation. *Astrophysical Letters*, 7:191.

Leighton, R. B., Noyes, R. W., Simon, G. W. (1962). Velocity Fields in the Solar Atmosphere. I. Preliminary Report. *Astrophysical Journal*, 135:474.

Leighton, R. B. (1963). The Solar Granulation. *Annual Review of Astronomy and Astrophysics*, 1:19.

Leka, K. D., Skumanich, A. (1998). The Evolution of Pores and the Development of Penumbrae. *Astrophysical Journal*, 507:454–469.

Leka, K. D. (1997). The Vector Magnetic Fields and Thermodynamics of Sunspot Light Bridges: The Case for Field-free Disruptions in Sunspots. *Astrophysical Journal*, 484:900.

Lin, H. (1995). On the Distribution of the Solar Magnetic Fields. *Astrophysical Journal*,446:421.

Lin, H. and Rimmele, T. (1999). The Granular Magnetic Fields of the Quiet Sun. *Astrophysical Journal*, 514:448–455.

Lisle, J., De Rosa, M., and Toomre, J. (2000). New Approach to Study Extended Evolution of Supergranular Flows and Their Advection of Magnetic Elements. *Solar Physics*, 197:21–30.

Lites, B. W. (1992). Sunspot oscillations - Observations and implications. *In: Sunspots: Theory and observations; Proceedings of the NATO Advanced Research Workshop on the Theory of Sunspots, Cambridge, United Kingdom*, 261–302.

Lites, B.W., Scharmer, G. B., Berger, T. E, and Title, A. M., (2004). Three-Dimensional Structure of the Active Region Photosphere as Revealed by High Angular Resolution. *Solar Physics*, 221:65–84.

Livingston, W. C. and Harvey, J. (1975). A New Component of Solar Magnetism - The Inner Network Fields. *Bulletin of the American Astronomical Society*, 7:346.

Livingston, W. and Mahaffey, C. (1981). Umbral Oscillations at the Photospheric Level. *Physics of Sunspots*, 312.

Livingston, W. (2002). Sunspots Observed to Physically Weaken in 2000-2001. *Solar Physics*, 207:41–45.

Loughhead, R. E., Bray, R. J., Brown, N. (1978). Instrumental profile of a triple Fabry-Perot interferometer for use in solar spectroscopy. *Applied Optics*, 17:415–419.

Marsch, E., Tu, C.-Y. (1997). Solar Wind and Chromospheric Network. newblock*Solar Physics*, 176:87–106.

Mártinez Pillet, V., Collados, M., Sánchez Almeida, J. et al. (1999). LPSP & TIP: Full Stokes Polarimeters for the Canary Islands Observatories. *High Resolution Solar Physics: Theory, Observations, and Techniques, ASP Conference Series 183. Eds. T. R. Rimmele, K. S. Balasubramaniam, and R. R. Radick*, 264.

McIntosh, S. W. and Jefferies, S. M. (2006). Observing the Modification of the Acoustic Cutoff Frequency by Field Inclination Angle. *Astrophysical Journal*, 647:L77–L81.

Mein, P. (1971). Inhomogeneities in the Solar Atmosphere from the Ca II Infra-Red Lines. *Solar Physics*, 20:3.

Meyer, F., Schmidt, H. U., Wilson, P. R., Weiss, N. O. (1974). The growth and decay of sunspots. *Monthly Notices of the Royal Astronomical Society*, 169:35–57.

Meyer, F., Schmidt, H. U., Weiss, N. O. (1977). The stability of sunspots. *Monthly Notices of the Royal Astronomical Society*, 179:741–761.

Muller, R. and Roudier, T. (1984). The fine structure of the quiet sun. *Solar Physics*, 94:33.

Muller, R. (1985). The fine structure of the quiet sun. *Solar Physics*, 100:237–255.

Muller, R., Auffret, H., Roudier, T., Vigneau, J., Simon, G. W., Frank, Z., Shine, R. A. and Title, A. M. (1992). Evolution and advection of solar mesogranulation. *Nature*, 356:322–325.

Muller, R., Steiner, O., Schlichenmaier, R., Brandt, P. N. (2001). Time-slice diagrams of solar granulation. *Solar Physics*, 203:211–232.

Nesis, A., Hanslmeier, A., Hammer, R., Komm, R., Mattig, W. and Staiger, J. (1992). Dynamics of the solar granulation. I - A phenomenological approach. *Astronomy and Astrophysics*, 253:561–566.

Nesis, A., Hammer, R., Hanslmeier, A., Schleicher, H., Sigwarth, M. and Staiger, J. (1997). Dynamics of the solar granulation. IV. Granular shear flow. *Astronomy and Astrophysics*, 326:851–859.

Nesis, A., Hanslmeier, A., Hammer, R., Komm, R., Mattig, W. and Staiger, J. (1993). Dynamics of the solar granulation. 2: A quantitative approach. *Astronomy and Astrophysics*, 279:599–609.

Nordlund, Å. (1983). Numerical 3-D simulations of the collapse of photospheric flux tubes. *In IAU Symp. 102: Solar and Stellar Magnetic Fields: Origins and Coronal Effects*, 79–83.

Nordlund, Å. (1984). Magnetoconvection: The interaction of convection and small scale magnetic fields. *In ESA The Hydromagnetics of the Sun*, 37–46 .

Nordlund, Å. (1984). Modelling of Small-Scale Dynamical Processes: Convection and Wave Generation. *in Small-Scale Dynamical Processes in Quiet Stellar Atmospheres, ed. S. L. Keil (Sunspot, NM: Sacramento Peak Observatory)*, 181.

Nordlund, Å. (1985). Solar convection. *Solar Physics*, 100:209–235.

Nordlund, Å. and Stein, R. F. (1990). Solar Magnetoconvection. *in Solar Photosphere: Structure, Convection, Magnetic Fields, IAU Symp. 138, ed. J. O. Stenflo*, 191.

Nordlund, Å. and Stein, R. F. (1995). Convection; Significance for Stellar Structure and Evolution. *in Proc. 32d Liége Colloq., ed. A. Noels et al. (Liege: Univ. Liége, Inst. d'Astrophys.)*, 75.

Nordlund, Å. and Stein, R. F. (1997). Stellar Convection; general properties. *Solar Convection and Oscillations and their Relationship, Proceedings of a workshop. Eds.: F.P. Pijpers, J. Christensen-Dalsgaard, and C.S. Rosenthal*, 79–103.

November, L. J., Toomre, J., Gebbie, K. B., and Simon, G. W. (1981). The detection of mesogranulation on the sun. *Astrophysical Journal*, 245:L123–L126.

November, L. J. and Simon, G. W. (1988). Precise proper-motion measurement of solar granulation. *Astrophysical Journal*, 333:427–442.

November, L. J. (1994). Inferring the depth extent of the horizontal supergranular flow. *Solar Physics*, 154:1–17.

Oda, N. (1984). Morphological study of the solar granulation. III - The mesogranulation. *Solar Physics*, 93:243–255.

Ofman, L., Klimchuk, J. A., Davila, J. M. (1998). A Self-consistent Model for the Resonant Heating of Coronal Loops: The Effects of Coupling with the Chromosphere. *Astrophysical Journal*, 493:474.

Osaki, Y. and Shibahashi, H. (1990). Progress of Seismology of the Sun and Stars. *Proceedings of the Oji International Seminar Held at Hakone, Japan, 1114 December 1989. Editor: Y. Osaki, H. Shibahashi, Lecture Notes in Physics*, 367.

Parker, E. N. (1963). Kinematical Hydromagnetic Theory and its Application to the Low Solar Photosphere. *Astrophysical Journal*, 138:552.

Parker, E. N. (1979). Sunspots and the physics of magnetic flux tubes. I - The general nature of the sunspot. II - Aerodynamic drag. *Astrophysical Journal*, 230:905-.923.

Parker, E. N. (1979). Sunspots and the physics of magnetic flux tubes. IX Umbral dots and longitudinal overstability. *Astrophysical Journal*, 234:333-347.

Parker, E. N. (1988). Nanoflares and the solar X-ray corona. *Astrophysical Journal*, 330:474–479.

Paraulski, K. and Jamerson, P. (1996). Enabling Technologies for a family of digital cameras SPIE. *The International Society for Optical Engineering; Solid State Sensor Arrays and CCD Cameras*, 2654.

Penn, M. J. and Labonte, B. J. (1993). The source of 5 minute period photospheric umbral oscillations. *Astrophysical Journal*, 415:383–396.

Penza, V., Caccin, B. and Del Moro, D. (2004). The sensitivity of the C I 538.0 nm Fe I 537.9 nm and Ti II 538.1 nm lines to solar active regions. *Astronomy and Astrophysics*, 427:345–351.

Plaskett, H. H. (1954). Motions in the Sun at the photospheric level. V. Velocities of granules and of other localized regions. *Monthly Notices of the Royal Astronomical Society*, 114:251.

Ploner, S. R. O., Solanki, S. K., and Gadun, A. S. (2000). Is solar mesogranulation a surface phenomenon?. *Astronomy and Astrophysics*, 356:1050–1054.

Porter, D. H. and Woodward, P. R. (1994). High-resolution simulations of compressible convection using the piecewise-parabolic method. *Astrophysical Journal Supplement Series*, 93:309–349.

Puschmann, K., Vázquez, M., Bonet, J. A., Ruiz Cobo, B. and Hanslmeier, A. (2003). Time series of high resolution photospheric spectra in a quiet region of the sun. I. Analysis of global and spatial variations of line parameters. *Astronomy and Astrophysics*, 408:363–378.

Qu, Z.Q.,Xu, Z. (2002). Key Properties of Solar Chromospheric Line Formation Process. *Chinese Journal of Astronomy & Astrophysics*, 2:71–80.

Rabin, D. and Moore, R. (1984). Heating the sun's lower transition region with fine-scale electric currents. *Astrophysical Journal*,285:359–367.

Raju, K. P., Srikanth, R., and Singh, J. (1999). Lifetimes and sizes of supergranular cells. *Bulletin of the Astronomical Society of India*, 27:65.

Ramsay, J. V., Kobler, H., Mugridge, E. G. V. (1970). A New Tunable Filter with a Very Narrow Pass-Band. *Solar Physics*, 12:492–501.

Rast, M. P. (1995). On the nature of 'exploding' granules and granule fragmentation. *Astrophysical Journal*, 443:863–868.

Rast, M. P. (1999). Thermal starting plumes, solar granulation, and the excitation of solar acoustic oscillations. *In Rimmele, T. R., Balasubramaniam, K. S., and Radick, R. R., editors, High Resolution Solar Physics: Theory, Observations and Techniques, ASP Conference Series 183*, page 443.

Rast, M. P. (2003b). The Scales of Granulation, Mesogranulation, and Supergranulation. *Astrophysical Journal*, 597:1200–1210.

Rast, M. P., Lisle, J. P., and Toomre, J. (2004). The Spectrum of the Solar Supergranulation: Multiple Nonwave Components. *Astrophysical Journal*, 608:1156–1166.

Reeves, E. M. (1976). The EUV chromospheric network in the quiet sun. *Solar Physics*, 46, 53–72.

Rice, J. B. and Gaizauskas, V. (1973). The Oscillatory Velocity Field Observed in a Unipolar Sunspot Region. *Solar Physics*, 32:421–433.

Richardson, R. S. and Schwarzchild, M. (1950). On the Turbulent Velocities of Solar Granules. *Astrophysical Journal*, 111:351.

Rieutord, M., Roudier, T., Malherbe, J. M., and Rincon, F. (2000). On mesogranulation, network formation and supergranulation. *Astronomy and Astrophysics*, 357:1063–1072.

Rimmele, T. and Schroeter, E. H. (1989). The variation of the cell size and velocities of the supergranulation with heliographic latitude. *Astronomy and Astrophysics*, 221:137–145.

Rimmele, T., (1997). Evidence for Magnetoconvection in a Sunspot Light Bridge. *Astrophysical Journal*, 490:458.

Rimmele, T. (2004). Recent advances in solar adaptive optics. *Advancements in Adaptive Optics. Edited by Domenico B. Calia, Brent L. Ellerbroek, and Roberto Ragazzoni. Proceedings of the SPIE*, 5490:34–46

Roudier, T. and Muller, R. (1987). Structure of the solar granulation. *Solar Physics*, 107:11–26.

Roudier, T., Rieutord, M., Malherbe, J. M., and Vigneau, J. (1999). Determination of horizontal velocity fields at the sun's surface with high spatial and temporal resolution. *Astronomy and Astrophysics*, 349:301–311.

Roudier, T., Bonet, J. A. and Sobotka, M. (2002). Properties of horizontal flows inside and outside a solar pore. *Astronomy and Astrophysics*, 395:249–255

Roudier, T., Ligniéres, F., Rieutord, M., Brandt, P. N. and Malherbe, J. M. (2003). Families of fragmenting granules and their relation to meso-and supergranular flow fields. *Astronomy and Astrophysics*, 409:299–308.

Rucklidge, A. M., Schmidt, H. U., and Weiss, N. O. (1995). The abrupt development of penumbrae in sunspots. *Monthly Notices of the Royal Astronomical Society*, 273:491-498.

Ruëdi, I., Solanki, S. K., Livingston, W. (1995). Infrared lines as probes of solar magnetic features. XI. Structure of a sunspot umbra with a light bridge. *Astronomy and Astrophysics*, 302:543.

Ryden, B. S. (1995). Measuring q_0 from the Distortion of Voids in Redshift Space. *Astrophysical Journal*, 452:25.

Ryden, B. S. and Melott, A. L. (1996). Voids in Real Space and in Redshift Space. *Astrophysical Journal*, 470:160.

Sánchez Almeida, J. and Lites, B. W. (2000). Physical Properties of the Solar Magnetic Photosphere under the MISMA Hypothesis. II. Network and Internetwork Fields at the Disk Center. *Astrophysical Journal*, 532:1215-1229.

Sánchez Almeida, J. (2003). Inter-Network magnetic fields observed during the minimum of the solar cycle. *Astronomy and Astrophysics*, 411:615–621.

Sánchez Almeida, J., Márquez, I., Bonet, J. A., Domínguez Cerdeña, I., and Muller, R. (2004). Bright Points in the Internetwork Quiet Sun. *Astrophysical Journal Letters*, 609:L91–L94.

Sankarasubramanian, K. and Rimmele, Th. (2003). Properties of Magnetic and Velocity Fields in and around Solar Pores. *Astrophysical Journal* 598:689–699.

Scherrer, P. H., Bogart, R. S., Bush, R. I., Hoeksema, J. T., Kosovichev, A. G., Schou, J., Rosenberg, W., Springer, L., Tarbell, T. D., Title, A., Wolfson, C. J., Zayer, I., MDI Engineering Team (1995). The Solar Oscillations Investigation - Michelson Doppler Imager. *Solar Physics*, 162:129–188.

Scheuer, M. A. and Thomas, J. H. (1981). Umbral oscillations as resonant modes of magneto-atmospheric waves. *Solar Physics*, 71:21–38.

Schmidt, W. abd Balthasar, H. (1994). Polarimetry and spectroscopy of a simple sunspot. 3: Velocity and magnetic field of sunspot umbral dots. *Astronomy and Astrophysics*, 283:241–246.

Schrijver, C. J., Hagenaar, H. J., and Title, A. M. (1997). On the Patterns of the Solar Granulation and Supergranulation. *Astrophysical Journal*, 475:328.

Schrijver, C. J. and Zwaan, C. (2000). Solar and stellar magnetic activity. newblock *Cambridge University Press*.

Schunker, H. and Cally, P. S. (2006). Magnetic field inclination and atmospheric oscillations above solar active regions. *Monthly Notices of the Royal Astronomical Society*, 372:551–564.

Schüssler, M. and Vögler, A. (2006). Magnetoconvection in a Sunspot Umbra. *The Astrophysical Journal*, 641:L73–L76.

Schwartz, S. J., Cally, P. S., Bel, N. (1984). Chromospheric and coronal Alfvenic oscillations in non-vertical magnetic fields. *Solar Physics*, 92:81–98.

Schwartz, S. J. and Bel, N. (1984). Propagation of waves in an atmosphere in the presence of a magnetic field. VII - Magneto-acoustic-gravity modes in an oblique B. *Astronomy and Astrophysics*, 137:128–132.

Severnyi, A. B. (1965). The Nature of Solar Magnetic Fields (The Fine Structure of the Field). *Soviet Astronomy*, 9:171.

Shine, R. A., Simon, G. W., and Hurlburt, N. E. (2000). Supergranule and Mesogranule Evolution. *Solar Physics*, 193:313–331.

Sigwarth, M., Balasubramaniam, K. S., Knölker, M., Schmidt, W. (1999). Dynamics of solar magnetic elements. *Astronomy and Astrophysics*, 349.941–955 .

Simon, G. W. and Leighton, R. B. (1964). Velocity Fields in the Solar Atmosphere. III. Large-Scale Motions, the Chromospheric Network, and Magnetic Fields. *Astrophysical Journal*, 140:1120.

Simon, W. G. (1967). Observations of Horizontal Motions in Solar Granulation: Their Relation to Supergranulation. *Zeitschrift fur Astrophysics*, 65:345.

Simon, G. W., Title, A. M., Topka, K. P., Tarbell, T. D., Shine, R. A., Ferguson, S. H., Zirin, H., and SOUP Team (1988). On the relation between photospheric flow fields and the magnetic field distribution on the solar surface. *Astrophysical Journal*, 327:964–967.

Smithson, R. C. (1975). Observations of Weak Solar Magnetic Fields with the Lockheed Diode Array Magnetograph. *Bulletin of the American Astronomical Society*, 7:346.

Sobotka, M., Bonet, J. A, and Vázquez, M., (1994). A high-resolution study of the structure of sunspot light bridges and abnormal granulation. *Astrophysical Journal*, 426:404–413.

Sobotka, M., Brandt, Peter N., Simon, G. W. (1997). Fine structure in sunspots. I. Sizes and lifetimes of umbral dots. *Astronomy and Astrophysics*, 328:682–688.

Sobotka, M., Vázquez, M., Bonet, J. A., Hanslmeier, A., Hirzberger, J. (1999). Temporal Evolution of Fine Structures in and around Solar Pores. *Astrophysical Journal*, 511:436–450.

Sobotka, M. (2003). Solar activity II: Sunspots and pores. *Astron. Nachr*, 324:369–373

Socas-Navarro, H., Trujillo Bueno, J., Ruiz Cobo, B. (2000). Anomalous Polarization Profiles in Sunspots: Possible Origin of Umbral Flashes. *Science*, 288:1396–13

Socas-Navarro, H. and Sánchez Almeida, J. (2003). Magnetic Fields in the Quiet Sun: Observational Discrepancies and Unresolved Structure. newblock*Astrophysical Journal*, 593:581–586.

Soltau, D., Schröter, E. H., Wöhl, H. (1976). On velocity oscillations in sunspot umbrae. *Astronomy and Astrophysics*, 50:367–370.

Spruit, H. (1979). Convective collapse of flux tubes. *Solar Physics*, 61:363–378.

Spruit, H. C. and Roberts, B. (1983). Magnetic flux tubes on the sun. *Nature*, 304.401–406.

Spruit, H. C., Nordlund, A., Title, A. M. (1990). Solar convection. *Annual review of astronomy and astrophysics*, 28:263-301.

Spruit, H. (1997). Convection in stellar envelopes: a changing paradigm. *Memorie della Societa Astronomia Italiana*, 68:397.

Spruit, H. C. and Scharmer, G. B. (2006). Fine structure, magnetic field and heating of sunspot penumbrae. *Astronomy and Astrophysics*, 447:343–354

Srikanth, R., Singh, J., and Raju, K. P. (2000). Distribution of Supergranular Sizes. *Astrophysical Journal*, 534:1008–1019.

Staude, J. (1999). Sunspot Oscillations. *Third Advances in Solar Physics Euroconference: Magnetic Fields and Oscillations, ASP Conference Series*, 184:113–130.

Stein, R. F. and Nordlund, Å. (1989). Topology of convection beneath the solar surface. *Astrophysical Journal*, 342:L95-L98.

Stein, R. F., Bercik, D. and Nordlund, Å. (2002). Solar convection and magneto-convection simulations. *Il Nuovo Cimento C*, 25:513.

Stein, R. F., Brandenburg, A. and Nordlund, Å. (1992). Magnet0-Convection. *in ASP Conf. Ser. 26, The Seventh Cambridge Workshop on Cool Stars, Stellar Systems, and the Sun, ed. M. S. Giampapa & J. A. Bookbinder, (San Francisco: ASP)*, 148.

Stein, R. F. and Nordlund, Å. (1998). Simulations of Solar Granulation. I. General Properties. *Astrophysical Journal*, 499:914.

Steiner, O., Knölker, M., Schüssler, M. (1994). Dynamic interaction of convection with magnetic flux sheets: first results of a new MHD code. *in NATO ASI Ser. 433, Solar Surface Magnetism, ed. R. J. Rutten & C. J. Schrijver (Dordrecht:Kluwer)*, 441.

Steiner, O., Grossmann-Doerth, U., Schüssler, M. Knölker, M. (1996). Radiation Diagnostics of Magnetohydrodynamic Models of the Solar Atmosphere. *Solar Physics*, 164:223-242.

Steiner, O., Grossmann-Doerth, U., Knölker, M., Schüssler, M. (1998). Dynamical Interaction of Solar Magnetic Elements and Granular Convection: Results of a Numerical Simulation. *Astrophysical Journal*, 495:468.

Steiner, O., Bruls, J., and Hauschildt, P. H. (2001). Why are G-Band Bright Points Bright?. In *ASP Conf. Ser. 236: Advanced Solar Polarimetry – Theory, Observation, and Instrumentation*, 453.

Straus, T., Deubner, F.-L., and Fleck, B. (1992). Is mesogranulation a distinct regime of convection?. *Astronomy and Astrophysics*, 256:652–659.

Straus, T. and Bonaccini, D. (1997). Dynamics of the solar photosphere. I. Two-dimensional spectroscopy of mesoscale phenomena. *Astronomy and Astrophysics*, 324:704–712.

Stuart, F. E. and Rush, J. H. (1954). Correlation Analyses of Turbulent Velocities and Brightness of the Photospheric Granulation. *Astrophysical Journal*, 120:245.

Sutterlin, P., Schroeter, E. H., and Muglac, K. (1996). Polarimetry of Solar Pores. *Solar Physics*, 164:311–320.

Suetterlin, P. and Wiehr, E. (1998). Temperature mapping of sunspots and pores from speckle reconstructed three colour photometry. *Astronomy and Astrophysics*, 336:367–370.

Tao, L., Weiss, N. O., Brownjohn, D. P., Proctor, M. R. E. (1998). Flux Separation in Stellar Magnetoconvection. *Astrophysical Journal Letters*, 496:L39.

Thomas, J. H. (1981). Theories of dynamical phenomena in sunspots. *The physics of sunspots; Proceedings of the Conference*, 345–358.

Thomas, J. H. and Scheuer, M. A. (1982). Umbral oscillations in a detailed model umbra. *Solar Physics*, 79:19–29.

Thomas, J. H., Cram, L. E., Nye, A. H. (1982). Five-minute oscillations as a subsurface probe of sunspot structure. *Nature*, 297:485–487.

Thomas, J. H., Cram, L. E.; Nye, A. H. (1984). Dynamical phenomena in sunspots. I - Observing procedures and oscillatory phenomena. *Astrophysical Journal*, 285:368–385.

Thomas, J. H. (1985). Oscillations in sunspots. *Australian Journal of Physics*, 38:811–824.

Thomas, J. H., and Weiss, N. O. (2004). Fine Structure in Sunspots. *Annual Review of Astronomy & Astrophysics*, 42:517–548

Title, A. M., Tarbell, T. D., Topka, K. P., Ferguson, S. H., Shine, R. A., and SOUP Team (1989). Statistical properties of solar granulation derived from the SOUP instrument on Spacelab 2. *Astrophysical Journal*, 336:475–494.

Tritschler, A., Schmidt, W., Rimmele, T. (2003). Annular Downflow Around a Solar Pore. *Astronomische Nachrichten Sopplement*, 324:54.

Tritschler, A., Schmidt, W., Langhans, K., Kentischer, T. (2002). High-resolution solar spectroscopy with TESOS - Upgrade from a double to a triple system. *Solar Physics*, 211:17–29.

Trujillo Bueno, J. (2003). Astrophysical Spectropolarimetry and Magnetic Field Diagnostics. *Modelling of Stellar Atmospheres. Ed. by N. Piskunov, W.W. Weiss, and D. F. Gray. Published on behalf of the IAU by the Astronomical Society of the Pacific*, 243.

Uchida, Y. and Sakurai, T. (1975). Oscillations in sunspot umbras due to trapped Alfven waves excited by overstability. *Astronomical Society of Japan*, 27:259–274.

Uitenbroek, H., Balasubramanian, K. S. and Tritschler, A. (2006). Evidence for a Siphon Flow Ending near the Edge of a Pore. *ApJ*, 645:776–781.

Ulrich, R. K. (1970). The Five-Minute Oscillations on the Solar Surface. *Astrophysical Journal*, 162:993.

Unsöld, A. (1930). Konvektion in der Sonnenatmosphäre. *Zeitschrift für Astrophysik*, 1:138.

van Ballegooijen, A. A., Nisenson, P., Noyes, R. W., Löfdahl, M. G., Stein, R. F., Nordlund, Å., Krishnakumar, V. (1998). Dynamics of Magnetic Flux Elements in the Solar Photosphere. *Astrophysical Journal,* 509:435–447.

van Noort, M., Rouppe van der Voort, L., Löfdahl, M. G. (2005). Solar Image Restoration By Use Of Multi-frame Blind De-convolution With Multiple Objects And Phase Diversity. *Solar Physics*, 228:191–215.

Vázquez, M. (1973). A Morphological Study of the Light-Bridges in Sunspots. Solar Physics, 31:377–387.

Vecchio, A., Cauzzi, G., Reardon, K. P., Janssen, K., Rimmele, T. (2007). Solar atmospheric oscillations and the chromospheric magnetic topology. *Astronomy and Astrophysics*, 461:L1–L4.

Vettolani, G., de Souza, R. E., Marano, B., Chincarini, G. (1985). The distribution of voids. *Astronomy and Astrophysics*, 144:506–513.

Vocks, C. and Mann, G. (2003). Generation of Suprathermal Electrons by Resonant Wave-Particle Interaction in the Solar Corona and Wind. *The Astrophysical Journal*, 593:1134–1145.

Vgler, A., Shelyag, S., Schssler,M.,Cattaneo, F. Emonet, T. and Linde, T. (2005). Simulations of magneto-convection in the solar photosphere. Equations, methods, and results of the MURaM code. *Astronomy and Astrophysics*, 429:335-351.

von der Lühe, O. and Kentischer, Th. J. (2000). High spatial resolution performance of a triple Fabry-Pérot filtergraph. *Astronomy and Astrophysics Supplement*, 146:499–506.

Wang, H., Tang, F., Zirin, H., and Wang, J. (1996). The Velocities of Intranetwork and Network Magnetic Fields. *Solar Physics*, 165:223–235.

Wang, H. and Zirin, H. (1989). Study of supergranules. *Solar Physics*, 120:1–17.

Wang, H. and Zirin, H. (1992). Flows around sunspots and pores. *Solar Physics*, 140:41–54.

Weiss, N. O., Brownjohn, D. P., Matthews, P. C., Proctor, M. R. E. (1996). Photospheric Convection in Strong Magnetic Fields. *Monthly Notices of the Royal Astronomical Society*, 283:1153-1164.

Wiehr, E. and Degenhardt, D. (1993). Magnetic field strengths in umbral dots. *Astronomy and Astrophysics*, 278:584–588.

Wilken, V., de Boer, C. R., Denker, C., and Kneer, F. (1997). Speckle measurements of the centre-to-limb variation of the solar granulation. *Astronomy and Astrophysics*, 325:819–824.

Yorke, H. W. (1980). Numerical solution of the equation of radiation transfer in spherical geometry. *Astronomy and Astrophysics*, 86:286–294.

Zhang, T. Y. and Suen, C. Y. (1984). A fast parallel algorithm for thinning digital patterns. *Communications of the ACM*, 273:236–239.

Zhang, H., Scharmer, G., Lofdahl, M., and Yi, Z. (1998a). Fine Structures of Magnetic Field in Solar Quiet Region. *Solar Physics*, 183:283–290.

Zhang, J., Lin, G., Wang, J., Wang, H., and Zirin, H. (1998b). The evolution of intranetwork magnetic elements. *Astronomy and Astrophysics*, 338:322–328.

Zhugzhda, Iu. D., Locans, V., Staude, J. (1983). Seismology of sunspot atmospheres. *Solar Physics*, 82:369–378.

Zhugzhda, Iu. D., Staude, J., Locans, V. (1984). A model of the oscillations in the chromosphere and transition region above sunspot umbrae. *Solar Physics*, 91:219–234.

Zhugzhda, Iu. D. and Dzhalilov, N. S. (1984). Magneto-acoustic-gravity waves on the sun. I - Exact solution for an oblique magnetic field. II - Transformation and propagation. *Astronomy and Astrophysics*, 132:45–57.

Zhugzhda, Iu. D. and Dzhalilov, N. S. (1984). Magneto Acoustic Gravity Waves on the Sun - Part Two - Transformation and Propagation. *Astronomy and Astrophysics*, 132:52.

Zhugzhda, Iu. D. and Dzhalilov, N. S. (1984). Magneto-acoustic-gravity waves on the sun. III - The theory of running penumbral waves. *Astronomy and Astrophysics*, 133:333–340.

Zirin, H. and Stein, A. (1972). Observations of Running Penumbral Waves. *Astrophysical Journal*, 178:L85.